In-situ evaluation of the hcp to bcc phase transformation kinetics in commercially pure titanium and Ti-5Al-5Mo-5V-3Cr alloy using laser ultrasonics

by

Alyssa Shinbine

B.Sc, University Of Alberta, 2013

A THESIS SUBMITTED IN PARTIAL FULFILLMENT OF THE REQUIREMENTS
FOR THE DEGREE OF

Master of Applied Science

in

THE FACULTY OF GRADUATE AND POSTDOCTORAL STUDIES
(Materials Engineering)

The University of British Columbia
(Vancouver)

March 2016

Abstract

This thesis developed and validated laser ultrasonics as an *in-situ* monitor of phase transformations in commercially pure titanium and Ti - 5 wt.% Al - 5 wt.% Mo - 5 wt.% V - 3 wt.% Cr (Ti-5553). Three studies (Chapters 5, 6 and 7) were performed to achieve this goal. The first study involved using finite element modeling (FEM) to simulate wave propagation through a 2-phase aggregate to understand the effects of precipitate arrangement and phase fraction on the velocity signal. The predicted ultrasound velocity depended on the geometric configuration of the microstructure and the relative size of the pulse's wavelength compared to the microstructural feature size. However, for mixtures of phases with similar elastic properties and densities (such as in α and β titanium), the possible averaging schemes produce nearly identical velocities, and thus using a rule of mixtures involving the α and β velocities was confirmed to be sufficient. The second study showed that the ultrasonic velocity is sensitive to the $\alpha \rightarrow \beta$ and $\beta \rightarrow \alpha$ transformations in commercially pure titanium, even though the density and elastic modulus of these two phases are very similar. Extraction of the transformation kinetics from the ultrasonic velocity does require, however, the effects of the strong starting texture and texture evolution during grain growth to be accounted for. Finally, the third study presented in Chapter 7 took Ti-5553 specimens, solutionized them to the fully β condition, and then held them for varying times at a 700 °C isotherm to monitor precipitation kinetics with LUMet. The precipitation of α grains could be monitored by using the relative change in velocity and compared to the *ex-situ* obtained phase fraction.

While laser ultrasonics has been previously used to measure the elastic constants in Ti-H alloys [1] and to qualitatively observe the transformation kinetics in Ti-6V-4Al [2] the work presented here represents the first fully quantitative assessment of transformation kinetics in pure titanium via laser ultrasonics. This is a significant result since *ex-situ*, metallographic analysis of the transformation in commercially pure titanium is not possible as the high temperature β phase is not stable at room temperature, and it paves the way for this technique to be used for microstructure monitoring during more complex thermo-mechanical processing paths in the Gleeble thermo-mechanical simulator. Laser ultrasonics was also validated in Ti-5553, where it was used to monitor the precipitation of α precipitates during an isothermal treatment, and produced comparable kinetics to the kinetics derived from *ex-situ* metallography.

Preface

The experimental work presented in this thesis was conducted at the University of British Columbia within the department of Materials Engineering. This included all the experimental design, material heat treatments, *in-situ* observation, sample preparation, and metallography. The initial sample template file used in ABAQUS was created by Quentin Puydt at the University of British Columbia. This template file was modified by the author to contain various microstructural arrangements (via MATLAB) and material properties in correspondence with the study presented in Chapter 5. The equilibrium α phase fraction at 700 °C used in Chapter 7 was calculated in the TTTI3 database in Thermocalc software by Julien Teixeira, at Institut Jean Lamour - SI2M in Nancy France.

Results and discussions pertaining to the hcp to bcc transformation in commercially pure titanium have been submitted for publication and is currently under review (A. Shinbine, T. Garcin, C. Sinclair (2015) "In-situ laser ultrasonic measurement of the hcp to bcc transformation in commercially pure titanium." Submitted and Under Review).

Table of Contents

Abstract . . . . . **ii**

Preface . . . . . **iii**

Table of Contents . . . . . **iv**

List of Tables . . . . . **vi**

List of Figures . . . . . **vii**

List of Abbreviations . . . . . **xi**

Acknowledgments . . . . . **xiii**

1 Introduction **1**

2 Literature Review **3**

2.1 General characteristics of the α and β phases in titanium 3

2.1.1 Crystal structures of the allotropic α and β phases 3

2.1.2 Temperature dependence of density of α and β phases 4

2.1.3 The effect of alloying elements on α and β phase stability in titanium alloys 5

2.1.4 Microstructural design for mechanical properties in β alloys 8

2.2 Elastic properties of titanium 10

2.2.1 Temperature dependence of elastic constants 10

2.2.2 Elastic anisotropy in titanium hcp and bcc single crystals 12

2.3 Mechanisms involved in the $\alpha \leftrightarrow \beta$ phase transformation 16

2.3.1 The α to β phase transformation 16

2.3.2 Grain growth in β phase titanium 20

2.3.3 The β to α phase transformation 20

2.3.4 Observation of phase transformation kinetics in titanium and Ti-5553 27

2.4 Laser ultrasonics 28

2.4.1 Laser generation and detection of ultrasonic pulse 29

2.4.2 Interpretation of waveform signal 30

2.5 Ultrasonic wave propagation in metals 33

2.5.1 Calculation of velocity from the Christoffel equation 33

2.5.2 Ultrasound velocity in an isotropic medium 34

2.5.3 Rotation of elastic stiffness tensors 35

2.5.4 Elastic properties of polycrystalline aggregates in the isotropic assumption 37

2.5.5 Ultrasound velocity in a textured polycrystalline aggregate 40

2.5.6 Velocity in the two phase region . . . 41

3 Scope and Objectives . . . 43

4 Experimental Methodology . . . 45
4.1 As-received materials . . . 45
4.1.1 Commercially pure titanium . . . 45
4.1.2 As-received Ti-5Al-5Mo-5V-3Cr . . . 45
4.2 *Ex-situ* microstructural characterization . . . 46
4.2.1 Scanning electron microscopy . . . 46
4.2.2 Electron backscatter diffraction . . . 46
4.3 *In-situ* microstructural characterization . . . 47
4.3.1 Laser ultrasonics . . . 47
4.3.2 Thermal treatments . . . 49
4.3.3 Interpretation of waveform data in CTOME . . . 50
4.3.4 Interpretation of error in laser ultrasound measurements . . . 51

5 Finite Element Modeling of Ultrasonic Wave Propagation in Dual Phase Material . . . 54
5.1 Introduction . . . 54
5.2 Input parameters, construction and assumptions . . . 54
5.2.1 Wavelet generation . . . 57
5.3 Interpretation of FEM data . . . 58
5.4 Calculation of average velocities . . . 60
5.5 FEM results . . . 61
5.6 Sensitivity of averaging schemes . . . 66
5.7 Chapter summary . . . 67

6 *In-situ* Laser Ultrasonic Measurement of the HCP to BCC Transformation in Commercially Pure Titanium . . . 69
6.1 Introduction . . . 69
6.2 Characterization of the as-received material . . . 70
6.3 *Ex-situ* observation of microstructural changes upon thermal cycling . . . 70
6.4 Evaluation of the ultrasonic velocity . . . 75
6.5 Chapter summary . . . 82

7 *In-situ* Laser Ultrasonic Measurement During Aging of Ti-5553 . . . 83
7.1 Introduction . . . 83
7.2 Characterization of the as-received material . . . 83
7.3 *Ex-situ* metallography . . . 84
7.4 Evaluation of ultrasonic velocity . . . 89
7.5 Chapter summary . . . 95

8 Summary and Future Work . . . 97
8.1 Summary . . . 97
8.2 Future work . . . 98

Bibliography . . . 101

A EBSD IPF comboscan maps . . . 107

B Plotting 3-D Surface Young modulus as a Function of Orientation . . . 109
B.1 Young modulus as a function of orientation in the titanium hcp unit cell . . . 109
B.2 Young modulus as a function of orientation in the titanium bcc unit cell . . . 112

List of Tables

Table 2.1 Parameters used in the Calphad approach for calculation molar volume, density, and CLE . . . 5
Table 2.2 Legend of author based color codes and symbols used in Figures 2.7a and 2.7b to describe the elastic response in hcp and bcc titanium . . . 10
Table 2.3 Comparison of calculated anisotropies for hcp and bcc titanium . . . 13
Table 2.4 The effect of cooling rate on formed α microstructures when $\alpha + \beta$ alloy Ti -6Al-4V [13], commercially pure titanium (cp-Ti) [14, 15], and extremely pure (ep-Ti) [14] is cooled from above the transus . . . 22

Table 5.1 Input parameters defining two isotropic phases used in an explicit 2-D FEM simulation of an ultrasound pulse propagating in a dual phased polycrystalline aggregate structure . . . 55
Table 5.2 Summary of imposed microstructures seeded to the core interaction region of the meshed specimen . . . 57
Table 5.3 Density (ρ) and P-wave moduli (λ) of polycrystalline α and β titanium at 882 °C . . . 66

Table 6.1 Microstructural parameters of commercially pure titanium in the: as-received condition, after 1 treatment cycle, after 5 treatment cycles . . . 73
Table 6.2 Reduced axis/angle pairs for each type of α/α boundaries that can result from the same parent β grain [88] . . . 74
Table 6.3 Best fit values of the adjustable parameters (A_1 and A_2) in equation 6.2 obtained by comparing during fitting the heating and cooling portions of the experimental data in Figure 6.6 for the 1^{st}, 2^{nd}, and 5^{th} cycles . . . 79

Table 7.1 Phase fraction of α (f_α) precipitated during isothermal holding at 700 °C . . . 85

List of Figures

Figure 2.1 Unit cells of a) hexagonal closed packed (hcp) alpha phase titanium and b) body center cubic (bcc) β phase titanium 4
Figure 2.2 Density of titanium hcp and bcc phases obtained using the CALPHAD method [25] . . . 5
Figure 2.3 The effect of alloying elements on equilibrium titanium phase diagram for additions of a) α b) β-eutectoid and c) β-isomorphous stabilizers. The β-transus is highlighted in purple [30]. 6
Figure 2.4 Schematic mapping multicomponent alloy classifications on a β isomorphous pseudo-binary phase diagram. M_s and M_f refer to the martensite start and finish lines, respectively [10]. 8
Figure 2.5 Two needles of atom probe tomography (APT) reconstructions demonstrating the presence of homogeneously dispersed ω phases after quenching and ω aging at 300 ˚C for 8 hours. Reprinted and reproduced with permission from Elsevier Publishing Ltd. [35] . . 9
Figure 2.6 Results Coakley *et al.* showing evolution of Vickers micro-hardness of Ti-5553 as a function of ageing time. The data presented shows the hardness of the quenched material (A-0), 300 ˚C and 400 ˚C samples with ageing times between 1 and 8 h, labeled A-1 to A-8 and C-1 to C-8 respectively. The hardness of sample B-2 which received a 300 ˚C/8h + 500 ˚C/2h aging heat treatment is also presented. Reprinted and reproduced with permission from Elsevier Publishing Ltd. [35] 9
Figure 2.7 a) Polycrystalline bulk and shear moduli of the hcp and bcc phases in pure titanium [36–41] and a nearly pure Ti-0.05% H alloy [1]. The red line signifies the transformation temperature T_{eq} of 882 ˚C; and b) Compilation of single crystalline elastic moduli of hcp (data left of T_{eq} = 882 ˚C) and bcc (data right of T_{eq} = 882 ˚C) phases in pure titanium [36–39, 41]. The red line signifies the transformation temperature T_{eq} of 882 ˚C. The symbols used here indicate the type of modulus plotted while the color indicates the source of the data. See Table 2.2 for details of both. 11
Figure 2.8 Temperature dependence of the anisotropy ratio (A) in hcp titanium [36] 14
Figure 2.9 Young Modulus as a function of orientation where the radius extending from the origin provides E in GPa and axis units are GPa for a) hcp titanium unit cell at 25 ˚C, and b) bcc titanium unit cell at 1000 ˚C. Code for calculating the direction dependence of Young modulus is provided in Appendices B.1 and B.2 16
Figure 2.10 Atomic projections on {0001} hcp planes and {110} bcc showing the changes in packing planes which result from the Burger's Orientation Relationship (BOR) observed during the hcp to bcc transformation scheme. Reprinted and reproduced with permission from American Physical Society (APS) [36] 17
Figure 2.11 Schematic of the competitive growth between two types of β morphology, where the intragranular plates are indicated by P, the allotriomorphs are indicated by A, and the matrix is comprised of α grains. Reprinted and reproduced with permission from Elsevier Publishing Ltd. [11] 19

Figure 2.12 Backscatter electron contrast images depicting grain growth of β titanium after a) 30 minutes, b) 1 hr, and c) 4 hrs at temperatures of approximately 910 °C. After 30 minutes, (a) surface relief due to thermal etching of the prior α grain boundaries is still visible, and the β grains are determined only by the orientation contrast. Reprinted and reproduced with permission from Elsevier Publishing Ltd. [11] 20
Figure 2.13 Optical micrographs of cp-Ti (grade 2) at cooling rates of a) 1 °C.s^{-1}, b) 50 °C.s^{-1}, c) 91 °C.s^{-1}, d) 356 °C.s^{-1}, e) 651 °C.s^{-1}, and f) 1604 °C.s^{-1}. A_α, M_α, BW_α, and α stand for acicular, massive, basketweave, and martensitic α. Obtained by Kim *et al.* (reprinted and reproduced with kind permission from Springer Science and Business Media) [15] . . 23
Figure 2.14 Plots showing a) fraction transformed over time held at each isotherm and b) the time temperature transformation (TTT) diagram for Ti-5553 obtained by Kar *et al.* (reprinted and reproduced with permission from Elsevier Publishing Ltd.) [57] 25
Figure 2.15 SEM backscatter micrographs of microstructures observed after treatment at 750 °C for a) 5 min and b) 30 min, 650 °C for c) 5 min and d) 30 min, and transmission electron microscope images of α plates precipitated after treatment at 550 °C for a) 5 min and b) 30 min. Obtained by Kar *et al.* (reprinted and reproduced with permission from Elsevier Publishing Ltd.) [57] 26
Figure 2.16 simplified schematic of the optical set-up for two-wave beam mixing method interferometry presented in [75] 30
Figure 2.17 Example of a waveform depicting compressive and shear echo signals in a 3 mm thick commercially pure titanium specimen 31

Figure 4.1 Schematic of cp-Ti specimen in the Gleeble with the normal direction (ND) aligned with the direction of wave propagation, the rolling direction (RD) aligned with the length of the specimen, the transverse direction (TD) aligned with the width of the specimen, and the EBSD image plane is shown in grey lying in the plane defined by the TD normal. . . 49
Figure 4.2 Heat treatment profiles for specimens enduring a) 1 cycle of treatment, b) 2 cycles of treatment, and c) 5 cycles of treatment where the red line indicates the equilibrium transformation temperature of 882 °C. 50

Figure 5.1 (a). 2D generated mesh part with thickness of 2 mm, length of 10 mm and mesh size of 4 μm in the small mesh region (4 mm x 2 mm), (b). horizontal plates, (c). vertical plates and (d). randomly dispersed elements. Vertical displacement (u_y) is measured as the direct output of the simulation from nodes in the generation/detection line (blue), and the vertical displacement direction is indicated by the red arrow. 56
Figure 5.2 a). Time dependence of the Ricker pulse amplitude and b). an example of the Gaussian scaling used to normalize the applied amplitude (at t = 125 s) across the generation boundary, where the peak of the Gaussian is centered on the mid line of the specimen . 58
Figure 5.3 Example of averaged displacement over time data taken from upper boundary nodes responsible for generation and detection of the Ricker's ultrasonic pulse 59
Figure 5.4 Example of a) two waveform echos (f and g), and, b) the corresponding amplitude of cross correlation function 60
Figure 5.5 Ultrasonic velocity computed by the six potential averaging schemes listed in Equations 5.4, 5.5, 5.6, 5.9, 5.10, 5.11, as well as FEM simulation results, where v_{HP}, v_{VP}, and v_{FEM} refer to simulation trial 9 (horizontal plate), trial 10 (vertical plate) and trials 1 - 8 (dispersed), respectively, as defined in Table 5.2.) 62
Figure 5.6 Schematic showing imposed Ricker wavelet a) propagating in horizontal plates where the wavelength is relatively larger than microstructural features, b) propagating in horizontal plates where the wavelength is smaller than microstructural features, c) propagating in vertical plates where the wavelength is relatively larger than microstructural features, d) propagating in vertical plates where the wavelength is smaller than microstructural features. The black lines indicates atoms in the wave, where lines appearing close together show compression of the wave, and lines spread apart indicate refraction. Wavelength is the distance between instances of maximum compression. 65

Figure 5.7 Velocity plotted against a changing ratio of P-wave modulus (ρ_α/ρ_β), where λ_α was fixed at 123.72 GPa, and λ_β is variable for a given phase fraction of β a) $f_\beta = 0.1$, b) $f_\beta = 0.5$, and c) $f_\beta = 0.9$ 67

Figure 6.1 Normal direction (ND) EBSD IPF map showing equiaxed and recrystallized grains in the as-received plate 70

Figure 6.2 Backscatter electron (BSE) images with detailed orientation contrast for the specimens in the a) as-received state (AR), b) after 1 treatment cycle (1-cycle), c) after 5 treatment cycles (5-cycles) of heat treatment, and low magnification BSE images showing typical microstructures d) after 1 treatment cycle (1-cycle), and e) after 5 treatment cycles (5-cycles) of heat treatment 71

Figure 6.3 Representative inverse ND pole figure maps (ND - IPF maps, A = 6.49 x 10^5 μm^2) showing the microstructure and microtexture in the: a) as-received state, b) after 1 treatment cycle, c) after 5 treatment cycles. In a), b), and c) the area of observation corresponds to the region where the ultrasonic pulse was induced and measured. Note that these regions have been cropped from much larger maps, the overall size of the parent map being given in Table 6.1. Full comboscan maps provided in Appendix A. . . 72

Figure 6.4 Grain boundary maps demonstrating: a) the α/α and b) prior β special boundary map of a specimen after 1 treatment cycle, and c) the α/α and d) prior β special boundary map of a specimen after 5 treatment cycles. Full comboscan maps provided in Appendix A. . 74

Figure 6.5 Pole figures showing texture in the: a) as-received state, b) after 1 treatment cycle, c) after 5 treatment cycles 75

Figure 6.6 Comparison of calculated velocity values to LUMet observations for heating and cooling of the a) 1^{st} treatment cycle, b) 2^{nd} treatment cycle, and c) 5^{th} treatment cycle, along with d) a compilation of velocity profiles demonstrating the variation in β velocity during heating in the 1^{st} cycle 76

Figure 6.7 Overview of the model used to calculate the velocity in a bulk aggregate of titanium. *$\Delta v/\Delta T$ back-calculated from average slopes of experimentally observed velocities and off-set so model velocity intersects experimental at 1000 ˚C 78

Figure 6.8 $\alpha \rightarrow \beta$ and $\beta \rightarrow \alpha$ phase transformation kinetics obtained from Equation 3 using the parameters given in Table 6.3 for specimens during the 1^{st}, 2^{nd} and 5^{th} cycle, respectively 81

Figure 7.1 Secondary Electron Image (SEI) demonstrating the as-forged Ti-5553 microstructure at magnifications of a) 1000x b) 10 000x 84

Figure 7.2 Electron backscatter diffraction (EBSD) inverse pole figure (IPF) map demonstrating globular primary α precipitates dispersed in a large β grain 84

Figure 7.3 BSE images taken at 20 kV and at low magnification of a specimen representative of the starting condition at the onset of the 700 ˚C isotherm (solutionized for 15 minutes at 900 ˚C, then cooled to 700 ˚C at 6.7 ˚C.s^{-1} and quenched). 86

Figure 7.4 EBSD phase map taken after a specimen was held at 700 ˚C for 5 minutes where black and white indicate the α and β phases, respectively 86

Figure 7.5 BSE images taken at 20 kV and a magnification of 500x of specimens held at the isothermal treatment for a) 10, b) 33, c) 53, d) 75 and e) 180 minutes. 87

Figure 7.6 Triple point β boundary in a specimen aged for 75 minutes at 700 ˚C demonstrating films of α_{GB} forming between the β grains and the growth of α_{W1} side-plates into the β grain visualized as a a) backscatter electron image and b) inverse pole figure map 88

Figure 7.7 Measurements of isothermal α precipitation obtained via *ex-situ* metallography 88

Figure 7.8 Comparison of a) raw absolute velocities at various isothermal holding times, and b) *in-situ* ultrasonic observation depicting relative change in velocity ($\Delta v = v_t - v_\beta$) 89

Figure 7.9 A comparison of: a) Inverse ND pole figure map (ND - IPF map) showing the microstructure and microtexture in hcp commercially pure titanium after 5 treatment cycles, and b) BSE image of a Ti-5553 specimen solutionized for 15 minutes at 900 ˚C, then cooled to 700 ˚C at 6.7 ˚C.s^{-1} and quenched to depict the bcc microstructure at the on-set of the isothermal treatment 92

Figure 7.10 Schematic showing a) the as-received (AR) 2^{nd} echo reference, fully β (BCC) 2^{nd} echo reference, and an arbitrary and representative high temperature 2^{nd} echo (Current signal), and b) cross-correlation function obtained when the current signal is compared to the as-received reference (red) and to the fully β reference (black). The dashed lines indicate the maximum amplitude, and corresponding time delay of each cross-correlation function. 94
Figure 7.11 Comparison fraction of α precipitation obtained via *ex-situ* metallography and normalized velocity data during isothermal treatment 95

Figure A.1 Full EBSD obtained comboscan a) inverse ND pole figure maps (ND - IPF maps) showing the microstructure and microtexture, b) the α/α special boundary map, and c) prior β special boundary map of a specimen after 1 treatment cycle 107
Figure A.2 Full EBSD obtained comboscan a) inverse ND pole figure maps (ND - IPF maps) showing the microstructure and microtexture, b) the α/α special boundary map, and c) prior β special boundary map of a specimen after 5 treatment cycles. 108

List of Abbreviations

APT atom probe tomography

AR as-received

bcc body center cubic

BOR Burger's Orientation Relationship

BSE backscatter electron

CCT continuous cooling transformation diagram

CLE coefficient of linear expansion

CPE4R four-node bi-linear quadrilateral plane strain elements

cp-Ti commercially pure titanium

CALPHAD computer coupling of phase diagrams and thermochemistry

CTOME computational tools for metallurgy

EBSD electron backscatter diffraction

EQAD equal area diameter

FE finite element

FEM finite element modelling

FFT fast fourier transform

hcp hexagonal closed packed

IFFT inverse fast fourier transform

IPF Inverse Pole Figure map

JMAK Johnson-Mehl-Avrami-Kolmogorov model

KSR Kurdjumov-Sachs relationship

LUMet laser ultrasonics for metallurgy

ND normal direction

ODC orientation distribution coefficients

P-wave modulus pressure wave modulus

RD rolling direction

SANS small angle neutron scattering

SEM scanning electron microscopy

SEI secondary electron image

SE2 single echo technique, with second echo selected as reference

TEM transmission electron microscopy

Ti-5553 Ti - 5 wt.% Al - 5 wt.% Mo - 5 wt.% V - 3 wt.% Cr

TTT time temperature transition

TD transverse direction

XRD X-ray diffraction

Acknowledgments

There are numerous people whose guidance, inspiration, and unwavering support made this thesis possible. I would be honored to take this moment to express my gratitude and respect for my mentors, colleagues, friends and family who have helped me along the way.

First and foremost, I wish to thank my supervisors, Dr. Chad Sinclair and Dr. Thomas Garcin for the support, guidance, and wealth of expertise they provided throughout this work.

I am very grateful to members of the LUMet group at the University of British Columbia. In particular, I wish to thank Dr. Warren Poole and Dr. Matthias Militzer for their expertise and feedback throughout my study. I also want to thank Mahsa Keyvani for her willingness to answer questions and provide insight in the lab.

I am very grateful to Quentin Puydt for his mentorship and willingness to tutor me on the use of ABAQUS and Finite Element Modeling.

I am very appreciative of the faculty and staff of the Department of Materials Engineering. In particular, I wish to thank the machine shop staff (Ross Mcleod, Carl Ng, and David Torok) and Jacob Kabel for their expert services, assistance, and uplifting conversations.

I would also like to thank Beth Sterling, Michael Wong, and Greg Nelson for their comradery, advice and friendship.

I want to thank my family: Mom, Dad, Sarah, Jeremy, and Peter, thank you for your constant encouragement and love.

Lastly, I would like to thank NSERC Canada for their contributions to my research.

Chapter 1

Introduction

Titanium and titanium alloys offer a wide array of benefits when compared to structural steels and nickel based alloys. Benefits include a high strength to density ratio, relatively high melting point, excellent corrosion resistance and comparable strength to structural steels [3–8]. As such, titanium and titanium alloys are used for structural applications in aerospace, biomedical, energy and marine industries, where the high performance characteristics of titanium and its alloys justify its relatively high cost.

In both commercially pure titanium and Ti-5553, the microstructure and mechanical properties are usually optimized by the control of the high temperature solid-state phase transformations that occur during high temperature processing. Upon heating, the low temperature hcp-alpha (α) phase transforms into the high temperature bcc-beta (β) phase at temperatures of about 882 °C[9] and 838 °C[10] for pure titanium and Ti-5553, respectively. This allotropic transformation to the β phase is followed by rapid grain growth [11, 12]. Upon subsequent cooling, the reverse transformation from β to α phase results in the formation of different α phase microstructures, eg. polygonal grains or a martensitic microstructure depending on the cooling conditions[13–15]. These different microstructures impact the final mechanical properties of the part[5, 16]. It is therefore critical to understand the mechanisms underlying this transformation in order to further control and optimize the use of this material for targeted applications.

There are a number of challenges associated with the *in-situ* study of the α-β phase transformation in titanium and titanium alloys. Unlike the austenite-ferrite phase transformation in steels, the volume change between the α-phase and β-phase is very small rendering the measurement of trans-

formation kinetics by dilatometry a significant challenge [17, 18]. Like ultra-low alloyed steels, the observation of the microstructure *post mortem* is also not a viable option for low alloyed titanium alloys as the β-phase cannot be retained at room temperature. Direct observation of the transformation performed *in-situ* at high temperature is possible [11], but limited to the extreme surface of the specimen and unsuitable for the measurement of bulk transformation kinetics. *In-situ* neutron or x-ray diffraction [19, 20] measurements made during continuous heating and cooling are another option but are limited by the acquisition time of the technique (particularly for neutron diffraction) [21] and by the rapid grain growth that occurs in the β-phase at high temperature. *In-situ* electrical resistivity measurements have been shown to be viable for measurements in commercially pure titanium but the method becomes more difficult to interpret in alloys where scattering from interfaces and solute atoms, which redistribute on transformation, can't be neglected [14, 15].

This thesis uses and validates laser ultrasonics as a useful method for the *in-situ* monitoring of phase transformations in commercially pure titanium and Ti-5553. In the case of the commercially pure titanium, a method using laser ultrasound was developed to account for texture changes during the transformation and grain growth above the β-transus. It was found that this was essential to properly account for the observed transformation kinetics. This method was then used to evaluate the isothermal $\beta \rightarrow \alpha$ kinetics for the Ti-5553 alloy. In this case, the ability of laser ultrasonics to measure the transformation kinetics could be compared to *ex-situ* metallography thereby allowing for validation of this technique.

Chapter 2

Literature Review

2.1 General characteristics of the α and β phases in titanium

2.1.1 Crystal structures of the allotropic α and β phases

Titanium and titanium alloys exist in several crystal structures depending on the temperature, composition, and treatment path (eg. cooling rate). The most important phases in titanium are the α and β phases. Another important phase is the orthorhombic ω phase that can result at specific pressures and compositions [13]. This phase is not observed under atmospheric pressure and equilibrium conditions in pure titanium and is not focused on in the current study. The $\beta \leftrightarrow \alpha$ transformation is allotropic and occurs at 882 °C [9]. Titanium exists at room temperature as a hexagonal closed packed (hcp) α phase, as shown in Figure 2.1a. Upon heating above 882 °C the hcp lattice will transform into a body centered cubic (bcc) lattice. When considering non-interacting identical hard spheres packed together in the hcp crystal structure, an ideal hcp cell has a c/a ratio of 1.633 [9]. However, in titanium, a slight atomic distortion occurs resulting in contraction along the c-axis [22]. This results in a c/a ratio of:

$$\frac{4.685\text{A}^\circ}{2.951\text{A}^\circ} = 1.5876 < 1.633 \tag{2.1}$$

The insertion of interstitial atoms such as C, N, O or the addition of substitutional α stabilizers with atomic radii smaller than that of titanium, will result in the increase of the c/a ratio [23, 24].

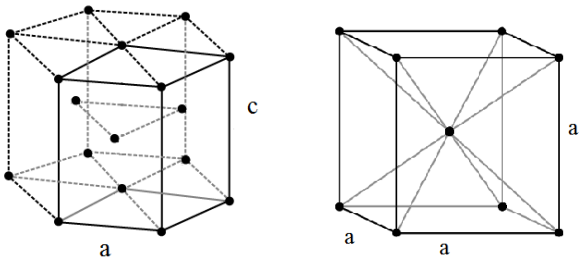

Figure 2.1: Unit cells of a) hexagonal closed packed (hcp) alpha phase titanium and b) body center cubic (bcc) β phase titanium

2.1.2 Temperature dependence of density of α and β phases

One of the properties that is important for determining ultrasonic wave propagation in materials is the density. The density of hcp and bcc titanium can be calculated using the CALPHAD parameters (Table 2.1) outlined in the work of Lu *et al.* [25]. The calculated temperature dependences of density in the hcp and bcc phases are presented in Figure 2.2. This approach makes two assumptions: There are no magnetic effects present, and the properties are calculated at atmospheric pressure. The temperature range was limited to between 298 K and the melting point 1945 K. Under these assumptions, the density (ρ), the molar volume (V_m) of a non-magnetic material, and the coefficient of linear thermal expansion (CLE) can be expressed as [25]:

$$\rho = \frac{M}{V_m} \tag{2.2}$$

$$V_m(T) = V_o \exp\left(\int_{T_o}^{T} 3CLE dT\right) \tag{2.3}$$

$$CLE = \frac{1}{3}\left(a + bT + cT^2 + dT^{-2}\right) \tag{2.4}$$

Where, the coefficients a, b, c, d, the molar volume (V_o) at the reference temperature (T_o = 298 K), and the molar mass of titanium (M) are given below in Table 2.1 [25].

Table 2.1: Parameters used in the Calphad approach for calculation molar volume, density, and CLE

Ti phase	a $(10^{-5}K^{-1})$	b $(10^{-8}K^{-2})$	c $(10^{-11}K^{-3})$	d (K)	V_o $(10^{-6}m^3mol^{-1})$	M $(10^{-3}Kgmol^{-1})$
α (hcp)	2.47929	1.03566	0	-0.144379	10.5463	47.876
β (bcc)	1.53848	1.86567	0	0	10.5919	47.876

In pure titanium, the percent difference in the densities of the α and β phase is 0.18 %, when calculated at the β-transus temperature of 882 °C. Conversely, the percent difference in density of austenite and ferrite in pure iron is 1.2 % at the same temperature, which is an order of magnitude larger than the percent difference in titanium. It can be seen that the volume change between the α-phase and β-phase is very small rendering the measurement of transformation kinetics by dilatometry a significant challenge compared to the austenite-ferrite phase transformation in steels [17, 18].

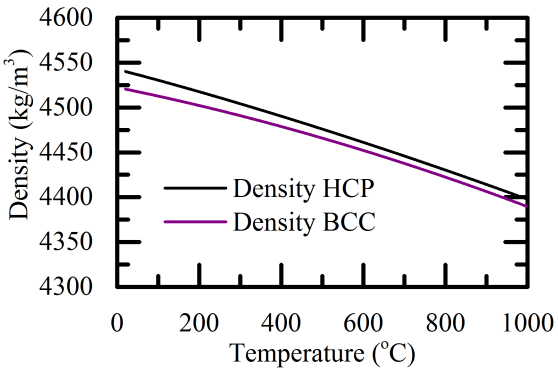

Figure 2.2: Density of titanium hcp and bcc phases obtained using the CALPHAD method [25]

2.1.3 The effect of alloying elements on α and β phase stability in titanium alloys

At a given temperature and pressure, the equilibrium phase of titanium is dependent on the alloying elements [4]. Alloying elements in titanium alloys are commonly described as being α stabilizers, β-isomorphous stabilizers, and β-eutectoid stabilizers. The α stabilized alloys are alloys that require increased temperatures compared to pure titanium to induce the $\alpha \rightarrow \beta$ transformation. The most common α stabilized alloys are Ti-Al based systems. Other α stabilizing elements include, oxygen, carbon, and nitrogen. The effect of introducing α stabilizers was demonstrated in the earliest of the Ti-Al phase diagrams, proposed by Molchanova [26]. Molchanova's phase diagram demonstrated

that with increasing addition of an α stabilizing element, the temperature separating the fully bcc β phase region from the α + β region, called the β-transus, will increase [26, 27]. This effect is demonstrated in the simple schematic representing possible titanium alloy phase diagrams for different stabilizer additions in Figure 2.3, where the β-transus is highlighted purple in each case.

β-isomorphous stabilizers are elements that decrease the β-transus temperature, or the temperature at which the α → β transformation occurs (cf. Figure 2.3b). The most common β -isomorphous stabilized alloys are Ti-Mo alloys. For additions of Mo up to 21 wt.%, a near linear increase in the β transus temperature is exhibited [28]. The solubility of molybdenum in titanium is very limited [28], hence, vanadium is also commonly employed as a β stabilizer since it spans a higher range of solubility [29]. Other β-isomorphous stabilizers include niobium and tantalum [10].

Finally, the β-eutectoid stabilizing elements also lower the β-transus temperature (cf. Figure 2.3c) . The most common β-eutectoid stabilized alloys are Ti-Cr alloys. However, iron is also a fairly common β-eutectoid stabilizer, along with (less commonly used) manganese, cobalt, copper, silicon, and hydrogen [10]. Ti-Cr alloys can form the phase $TiCr_2$, which has three possible crystal structures, and occurs over a very narrow compositional range of 65-68 wt% chromium [10]. Both chromium and iron are termed sluggish eutectoid formers, meaning the presence of these intermetallic compounds in commercial alloys is unlikely [10].

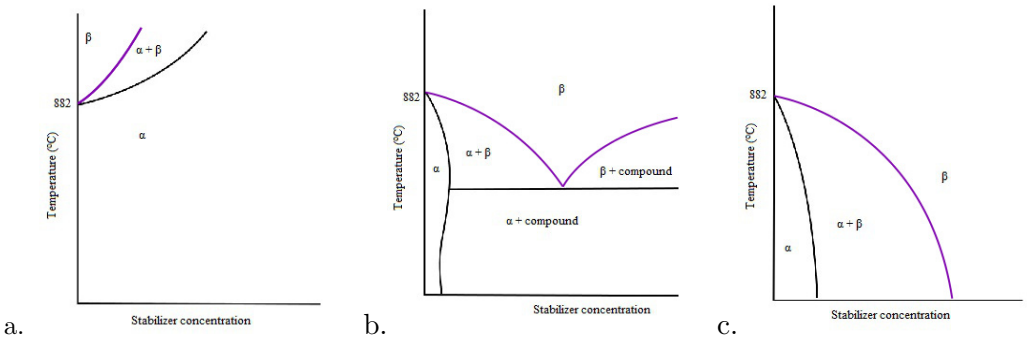

Figure 2.3: The effect of alloying elements on equilibrium titanium phase diagram for additions of a) α b) β-eutectoid and c) β-isomorphous stabilizers. The β-transus is highlighted in purple [30].

Multicomponent alloys, such as alloy Ti-5553, are comprised of both α and β stabilizers. Such alloys allow for the combination of the good forgeability of the bcc crystal structure with the ability to be hardened to fairly high strength levels via aging treatments [3]. While other classification schemes exist, this thesis will make use of the "US Technical Multicomponent Classification" which

subdivides titanium alloys into α, β and α + β alloys where α + β can be further classified as either near-α or near-β alloys. Under this classification, Ti-5553 is described as a β alloy [10]. Interpreting the effects of the numerous stabilizing elements discussed above can be represented more simply by calculating their equivalent α and β stabilizing effects on titanium, where these effects are represented as an equivalent aluminum and molybdenum concentration, respectively. The aluminum equivalent concentration in weight percent ($[Al]_{eq}$) can be calculated based on the weight percent concentrations of Al, Zr, Sn, and O as shown in Equation 2.5 [31].

$$[Al]_{eq} = [Al] + \frac{1}{6}[Zr] + \frac{1}{3}[Sn] + 10[O] \tag{2.5}$$

Conversely, the molybdenum equivalent concentration in weight percent ($[Mo]_{eq}$) can be calculated based on the weight percent concentrations of Mo, Ta, Nb, W, V, Cr and Ni as shown in Equation 2.6 [26].

$$[Mo]_{eq} = [Mo] + \frac{1}{5}[Ta] + \frac{1}{3.6}[Nb] + \frac{1}{2.5}[W] + \frac{1}{1.5}[V] + 1.25[Cr] + 1.25[Ni] \tag{2.6}$$

For the β phase to be retained at room temperature, a minimum $[Mo]_{eq}$ of 10 is needed [10]. Ti-5553 has an $[Mo]_{eq}$ of 13 and can retain a fully β structure upon quenching [10]. Conceptually, titanium alloy classification can be visualized as a β isomorphous pseudo-binary phase diagram [32]. This scheme orders alloys according to their relative abundance of α and β stabilizing elements in terms of $[Mo]_{eq}$ and $[Al]_{eq}$. This representation is provided in Figure 2.4.

In Figure 2.4 the line labeled M_S refers to the martensite start temperature. If an alloy is quenched fast enough below this temperature, the β phase will transform martensitically to form α'. For alloys with compositions lying to the left of the M_s line (shown in Figure 2.4), the martensitic transformation will occur if the cooling rate surpasses a critical value. The martensitic transformation involves a collective movement of atoms to change the crystal lattice from a bcc to a hcp crystal structure. This cooperative motion involves a relatively large number of atoms that are displaced by only a fraction of the inter-atomic spacing relative to their neighbors and occurs by a shear-based, diffusionless mechanism. To date, only two martensitic structures have been reported in titanium alloys. These are the hcp α' structure, common to pure titanium and low alloyed systems, and an orthothrombic α" structure, common to titanium alloy systems alloyed with β stabilizers [33]. The

Ms temperature of Ti-5553 is below room temperature (Figure 2.4). This means that if Ti-5553 is quenched it will form a metastable, fully β microstructure. This is why Ti-5553 is often called a metastable β alloy.

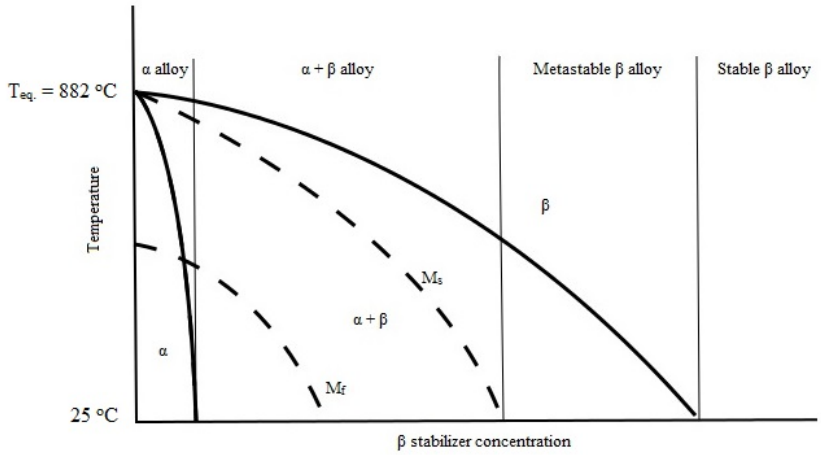

Figure 2.4: Schematic mapping multicomponent alloy classifications on a β isomorphous pseudo-binary phase diagram. M_s and M_f refer to the martensite start and finish lines, respectively [10].

Given its composition, Ti-5553 has a β transus temperature of 838 °C which is much lower than the transformation temperature of pure titanium (882 °C). Figure 2.4 demonstrates that at room temperature, and given equilibrium conditions, that a mixture of α and β is stable. This is important because if Ti-5553 is quenched to form a 100 % β microstructure, it can then undergo an aging heat treatment to precipitate the α phase and create a dual-phase microstructure.

2.1.4 Microstructural design for mechanical properties in β alloys

The value of a metastable β alloy such as Ti-5553 is that it can be produced with lesser quantities of β stabilizer elements, so as to produce alloys with the highest strength-to-density ratios in titanium alloys [34]. Metastable β alloys have high ductility in the quenched (fully β) state, which is beneficial in the fabrication of complex parts. After the part has been formed, high strength can be achieved by aging heat treatments, where the formation of fine α precipitates contributing to the high strength associated with these materials [34].

The nucleation of the α phase occurs heterogeneously on grain boundaries, inclusions and other precipitates. This allows the precipitation strengthening due to α formation to be manipulated by

changing the density and arrangement of nucleation sites. In Ti-5553 this is done by isothermal aging at low temperature to form a fine dispersion of metastable ω_{iso} (Figure 2.5) [35]. After the formation of the ω phase, the material is subjected to a higher temperature aging treatment during which a fine dispersion of the alpha phase forms preferentially on the ω phase.

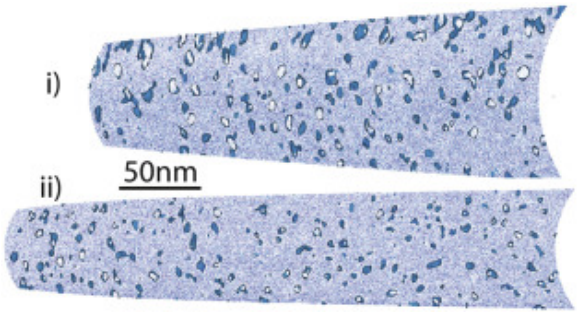

Figure 2.5: Two needles of atom probe tomography (APT) reconstructions demonstrating the presence of homogeneously dispersed ω phases after quenching and ω aging at 300 °C for 8 hours. Reprinted and reproduced with permission from Elsevier Publishing Ltd. [35]

Coakley *et al.* [35] found that ω aging followed by α aging treatments resulted a 90 % increase in hardness compared to the quenched material due to the distribution of fine α precipitates formed after treatment, as shown in Figure 2.6.

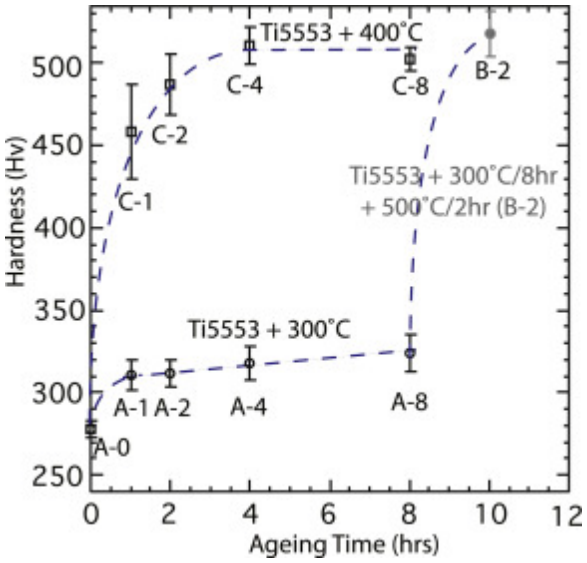

Figure 2.6: Results Coakley *et al.* showing evolution of Vickers micro-hardness of Ti-5553 as a function of ageing time. The data presented shows the hardness of the quenched material (A-0), 300 °C and 400 °C samples with ageing times between 1 and 8 h, labeled A-1 to A-8 and C-1 to C-8 respectively. The hardness of sample B-2 which received a 300 °C/8h + 500 °C/2h aging heat treatment is also presented. Reprinted and reproduced with permission from Elsevier Publishing Ltd. [35]

2.2 Elastic properties of titanium

2.2.1 Temperature dependence of elastic constants

Like density, the elastic properties are also important for determining ultrasonic wave propagation in materials. The bulk elastic properties of hcp and bcc titanium have been explored experimentally [1, 36–39] as well as computationally [40, 41]. The bulk (B) and shear (G) modulus are presented in Figure 2.7a. The bulk and shear modulus of the α phase decreases with increasing temperature. Ogi *et al.* [38] measured that the longitudinal and bulk moduli of the high temperature β phase demonstrate limited temperature dependence. The temperature dependence of single crystalline elastic moduli of hcp (data left of T_{eq} = 882 °C) and bcc (data right of T_{eq} = 882 °C) phases in pure titanium are given in Figure 2.7b [36–39, 41]. Numerous data from various sources have been compiled in Figures 2.7a and 2.7b. The corresponding symbols and color coding used to represent the data and their sources are provided below in Table 2.2.

Table 2.2: Legend of author based color codes and symbols used in Figures 2.7a and 2.7b to describe the elastic response in hcp and bcc titanium

Method	color	phase	Elastic Modulus								
			c_{11} ■	c_{33} ●	c_{44} ▲	c_{66}* ▼	c'* ▼	c_{13} ◆	c_{12} ◀	B +	G ×
ultrasound [36]	—	hcp	x	x	x	x		x	x		
electromagnetic acoustic resonance [38]	—	hcp/bcc	x	x	x	x			x	x	x
ultrasound [37]	—	bcc	x		x		x		x		
coherent inelastic neutron scattering [39]	—	bcc	x		x		x		x	x	x
resonant-ultrasound spectroscopy [41]	—	bcc	x		x		x		x		
laser ultrasound** [1]	—	hcp/bcc								x	x
laser ultrasound*** [1]	—	bcc								x	x
first principle calculations [40]	—	bcc								x	
first principles calculations [42]	—	bcc								x	

* Where $c_{66} = \frac{1}{2}(c_{11} - c_{12})$ in the hcp phase and $c' = \frac{1}{2}(c_{11} - c_{12})$ in the bcc phase
** Data for hcp polycrystalline constants for low alloyed titanium (Ti 0.05 % H) [1]
*** Data for bcc polycrystalline constants for pure titanium at room temperature, extrapolated [1]

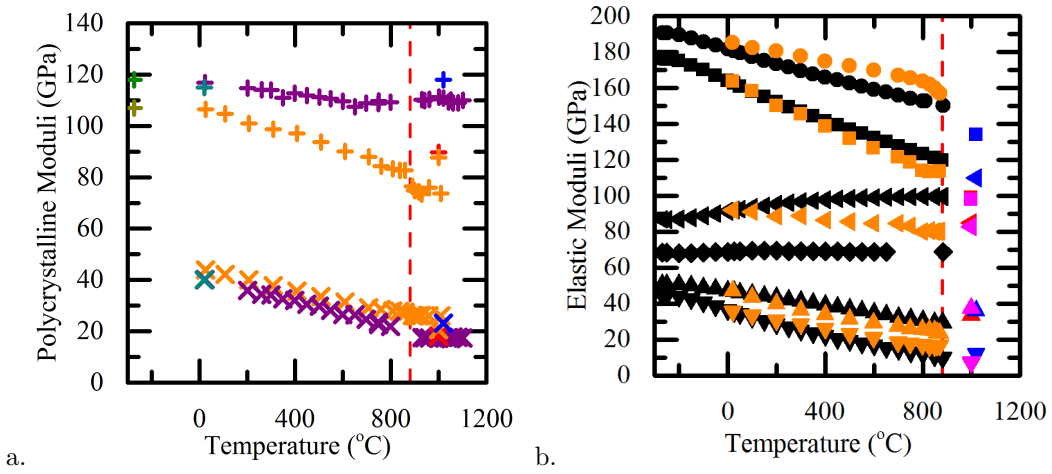

a. b.

Figure 2.7: a) Polycrystalline bulk and shear moduli of the hcp and bcc phases in pure titanium [36–41] and a nearly pure Ti-0.05% H alloy [1]. The red line signifies the transformation temperature T_{eq} of 882 °C; and b) Compilation of single crystalline elastic moduli of hcp (data left of T_{eq} = 882 °C) and bcc (data right of T_{eq} = 882 °C) phases in pure titanium [36–39, 41]. The red line signifies the transformation temperature T_{eq} of 882 °C. The symbols used here indicate the type of modulus plotted while the color indicates the source of the data. See Table 2.2 for details of both.

In hcp titanium, the 5 independent elastic stiffness constants c_{11}, c_{44}, c_{12}, c_{13}, and c_{33} (shown in Figure 2.7) have demonstrated temperature dependence in the single phase elastic region [36, 38]. The linear regressions for each independent elastic constant (in Pa) obtained from Fisher *et al.* [36] as a function of temperature (in ^{o}C) are as follows:

$$c_{11}(\text{Pa}) = \left(-0.0513(\text{GPa.}^{\circ}\text{C}^{-1})\text{T}(^{\circ}\text{C}) + 163.34(\text{GPa})\right) * 10^{9}(\text{Pa.GPa}^{-1}) \quad (2.7)$$

$$c_{12}(\text{Pa}) = \left(0.0118(\text{GPa.}^{\circ}\text{C}^{-1})\text{T}(^{\circ}\text{C}) + 91.313(\text{GPa})\right) * 10^{9}(\text{Pa.GPa}^{-1}) \quad (2.8)$$

$$c_{13}(\text{Pa}) = \left(0.0006(\text{GPa.}^{\circ}\text{C}^{-1})\text{T}(^{\circ}\text{C}) + 68.736(\text{GPa})\right) * 10^{9}(\text{Pa.GPa}^{-1}) \quad (2.9)$$

$$c_{33}(\text{Pa}) = \left(-0.0363(\text{GPa.}^{\circ}\text{C}^{-1})\text{T}(^{\circ}\text{C}) + 181.29(\text{GPa})\right) * 10^{9}(\text{Pa.GPa}^{-1}) \quad (2.10)$$

$$c_{44}(\text{Pa}) = \left(-0.0199(\text{GPa.}^{\circ}\text{C}^{-1})\text{T}(^{\circ}\text{C}) + 46.856(\text{GPa})\right) * 10^{9}(\text{Pa.GPa}^{-1}) \quad (2.11)$$

No temperature dependent profiles of single crystal elastic constants for the bcc titanium phase are currently available. However, single crystal elastic constants were determined at 1000 °C [37, 41] and at 1020 °C [1]. The values from Fisher and Dever [37] can be used when looking at potential

orientation dependent ultrasound velocities in bcc titanium.

$$c_{11} = 99 * 10^9 (\text{Pa}) \tag{2.12}$$

$$c_{12} = 85 * 10^9 (\text{Pa}) \tag{2.13}$$

$$c_{44} = 33.6 * 10^9 (\text{Pa}) \tag{2.14}$$

The first principle calculations of Ahuja *et al.* [43] demonstrated that the bcc structure in titanium is expected to be unstable at 1 atm and absolute zero temperature. Despite this instability, the bcc crystal structure is stable in titanium at sufficiently high temperatures. This is due to the high entropy associated with the bcc crystal structure, and the fact that the structure is stabilized due to the lattice vibration modes of titanium at high temperature. Due to this, it is expected that β titanium would exhibit some anomalous physical properties [43]. Ahuja *et al.* [43] showed that as the pressure increases, so does the stability of the bcc phase, and this is attributed to the decreasing magnitude of the negative single crystal tetragonal shear constant ($c^{'}$) of the bcc phase with decreasing volume until it becomes positive. The tetragonal shear constant in the bcc crystal is given by:

$$c^{'} = \frac{1}{2}(c_{11} - c_{12}) \tag{2.15}$$

Fisher and Renken [36] and Ogi *et al.* [38] measured the single crystal elastic constants of hcp titanium as a function of temperature up until the β-transus temperature of 882 °C. Petry *et al.* [39], Fisher and Dever [37], and Ledbetter *et al.* [41] measured the single crystal elastic constants of bcc titanium at temperatures of 1020 °C, 1000 °C, and 1000 °C, respectively. The single crystal elastic constants presented in the literature [36–39, 41] of the hcp and bcc phases in titanium are presented in Figure 2.7b.

2.2.2 Elastic anisotropy in titanium hcp and bcc single crystals

While it may not be initially obvious by referencing Figures 2.7a and 2.7b, the α and β phases are markedly different in regards to their elastic response. The calculated anisotropies for each phase

at selected temperatures are provided in Table 2.3. In particular, the elastic anisotropy of the bcc phase is much greater than that of the hcp phase. Firstly, it can be observed that the anisotropy in hcp titanium increases with increasing temperature. The elastic anisotropy of hcp titanium at absolute zero was close to one (A = 1.17), indicating near elastic isotropy [36]. As the hcp titanium was heated, both Ogi *et al.* [38] and Fisher and Renken [36] observed increasing values in elastic isotropy, and a value of 3.58 was observed at the β-transus (T = 882 °C) by Fisher and Renken [36]. The elastic anisotropy is further increased upon transformation into the bcc phase, where Fisher and Dever [37] and Ledbetter *et al.* [41] observed values of 4.8 and 5, respectively at 1000 °C. Figure 2.8 demonstrates the non-linear increase in anisotropy in the hcp phase as the transformation temperature is approached.

Table 2.3: Comparison of calculated anisotropies for hcp and bcc titanium

Temperature (°C)	phase (hcp/bcc)	$A = \frac{c_{44}}{c_{66}}$	$A = \frac{c_{44}}{0.5(c_{11}-c_{12})}$	Reference
-273.15	hcp	1.17	-	[36]
20	hcp	1.31	-	[36]
882	hcp	3.58	-	[36]
1000	bcc	-	4.8	[37]
1000	bcc	-	5	[41]
1020	bcc	-	3	[39]

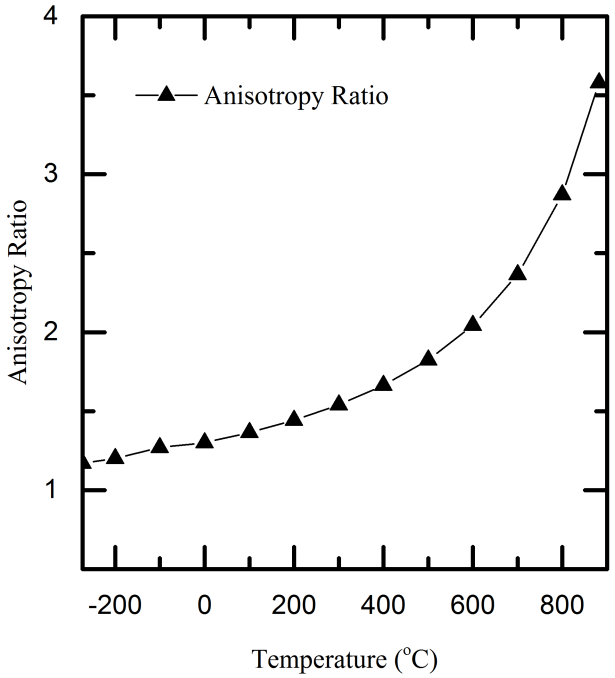

Figure 2.8: Temperature dependence of the anisotropy ratio (A) in hcp titanium [36]

Unfortunately, no studies to date have reported the temperature dependence of the single crystal elastic constants in bcc titanium, so from the data presented above, it is difficult to discern the temperature dependence of its elastic anisotropy. However, if one returns to the work of Ahuja *et al.* [43] outlining the effect of pressure on c', one can make an inference as to the anisotropy of titanium at absolute zero and compare the calculated anisotropy to the experimentally observed high temperature values [37]. The key observation one can make, is that as the pressure approaches atmospheric pressure, c' will become increasingly negative. A negative c' indicates that the crystal structure is mechanically unstable. At atmospheric pressure and absolute zero, a c' of approximately -75 GPa is calculated from first principles [43]. Ahuja *et al.* [43] also calculated the c_{44} at these conditions and achieved a value of 35.8 GPa, which is in relatively good agreement with the experimentally observed values for bcc titanium presented above in Table 2.3. This indicates that c_{44} in bcc titanium is relatively insensitive to temperature. However, the drastic increase in stiffness calculated at absolute zero [43] and observed at 1000 °C [37] in c' (from -75 GPa to 7 GPa) indicates that shear corresponding to c' is strongly altered by vibrational effects at high

temperature [43].

The anisotropy of the bcc crystal has inherent effects on the observed ultrasound velocity during monitoring of the bcc β phase. The elastic response of a crystal along any set of directions may be calculated by resolving the stress state onto the crystal axes [44]. The orientation dependence of the Young's modulus (E) is given by Equation 2.16 and Equation 2.17 for a cubic and hexagonal crystal, respectively [44]. The coordinate system parameters α, β, γ used in Equation 2.16 and Equation 2.17 are given in terms of the direction indices [hkl] in Miller notation (for both the hcp and bcc cases) by Equations 2.18, 2.19, 2.20, respectively [44].

$$\frac{1}{E_{bcc}} = s_{11} + (2s_{12} - 2s_{11} + s_{44})\left(\beta^2\gamma^2 + \gamma^2\alpha^2 + \alpha^2\beta^2\right) \tag{2.16}$$

$$\frac{1}{E_{hcp}} = \left(1-\gamma^2\right)^2 s_{11} + \gamma^4 s_{33} + \gamma^2\left(1-\gamma^2\right)(2s_{13} + s_{44}) \tag{2.17}$$

$$\alpha = \frac{h}{\left(h^2+k^2+l^2\right)^{1/2}} \tag{2.18}$$

$$\beta = \frac{k}{\left(h^2+k^2+l^2\right)^{1/2}} \tag{2.19}$$

$$\gamma = \frac{l}{\left(h^2+k^2+l^2\right)^{1/2}} \tag{2.20}$$

Figure 2.9 shows the Young moduli across varied directions in the bcc and hcp unit cell and was created using Equation 2.16, Equation 2.17, the room temperature single crystal compliances for hcp titanium [36], and the compliances available for bcc titanium at 1000 °C [37].

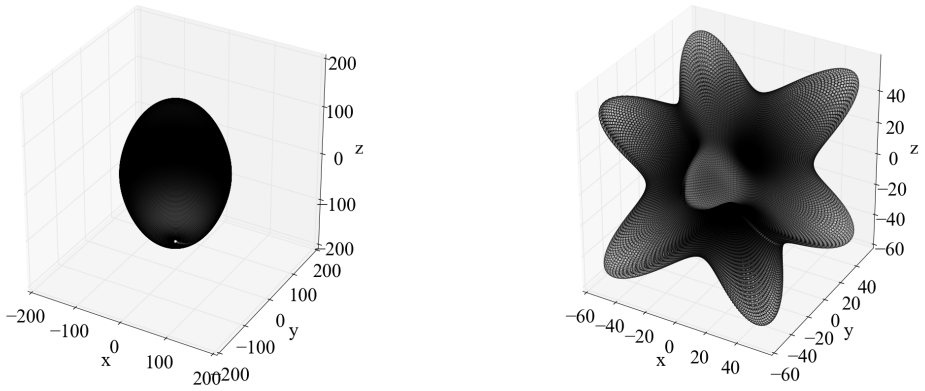

a. b.

Figure 2.9: Young Modulus as a function of orientation where the radius extending from the origin provides E in GPa and axis units are GPa for a) hcp titanium unit cell at 25 °C, and b) bcc titanium unit cell at 1000 °C. Code for calculating the direction dependence of Young modulus is provided in Appendices B.1 and B.2

It can be observed that the elastic response in the hcp crystal is isotropic in the basal plane which is characteristic of all hcp crystals. The Young's moduli observed along the c-axis (E_c) and in the basal plane (E_{basal}) are 146 GPa and 104 GPa, respectively. Thus, sound will travel faster when the sound wave's propagation is aligned with the c-axis of the hcp crystal. Conversely, the bcc crystal demonstrates greatest anisotropy when comparing [100] and [111] directions. The minimum and maximum observed Young's moduli occur along the [100] and [111] directions, respectively, where $E_{[100]} = 20.5$ GPa and $E_{[111]} = 89.6$ GPa.

2.3 Mechanisms involved in the $\alpha \leftrightarrow \beta$ phase transformation

2.3.1 The α to β phase transformation

Crystallography plays a large role in the transformation from the α to β phase and vice versa. Numerous investigations observing the $\beta \longleftrightarrow \alpha$ transformation have described the orientation relationship between a parent β grain and a resulting daughter α grain as being a Burgers orientation relationship [45–47]. This orientation relationship also governs the reverse transformation from a given α grain to a newly formed β grain upon heating. The crystallographic Burgers orientation

relation between the β phase and α phase is defined as [48]:

$$\begin{aligned}(110)_\beta \parallel (0002)_\alpha \\ [1\bar{1}1]_\beta \parallel [11\bar{2}0]_\alpha\end{aligned} \tag{2.21}$$

Where both the diffusional and martensitic transformation follows this relation. There are 6 closest packed planes and 2 slip directions within the β parent grains resulting in a maximum occurrence of 12 distinct orientations that can be formed in the nucleated α phase for a given parent orientation.

Section 2.1.2 had shown the c/a ratio for an hcp titanium unit cell to be approximately 1.59. A c/a < 1.633 implies a larger separation of atoms in the basal planes of the hcp structure than that which exists between different planes, as shown in Figure 2.10 [36].

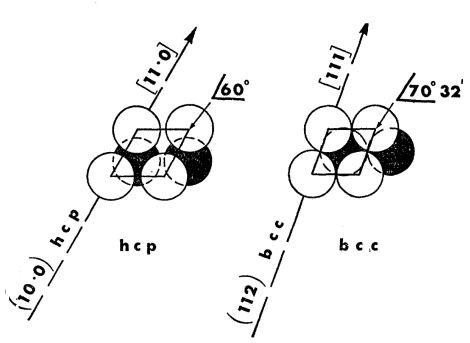

Figure 2.10: Atomic projections on {0001} hcp planes and {110} bcc showing the changes in packing planes which result from the Burger's Orientation Relationship (BOR) observed during the hcp to bcc transformation scheme. Reprinted and reproduced with permission from American Physical Society (APS) [36]

Due to this wide separation, it can be assumed that the thermal energy is most likely going to excite vibrational modes which will alter these separations [36]. Since shear distortions are easier to produce than compressional distortions [36], thermal vibrational modes corresponding to the c_{66} mode are thought to occur in the hcp lattice when approaching the transformation temperature [36, 49]. Fisher and Renken [36] postulated that, in accordance with the work of Zener [49], the large shear vibrations in the basal plane could potentially be vibrating out of phase, contributing to an increased repulsion of the two basal planes. This repulsion would manifest as a higher temperature dependence of the coefficient of linear thermal expansion (CLE) parallel to the c-axis.

The studies of Sirota and Zhabko [50], and Spreadborough and Christian [51] demonstrated that α titanium demonstrates a higher CLE parallel to the c-axis than parallel to the a-axis, and that the anisotropy of the CLE in different directions diminishes with increasing temperature [50]. The onset of positive curvature in the c_{66} modulus at 146 ° C (cf. Figure 2.7b) combined with the decreased anisotropy in the CLE with increasing temperature would suggest a decreasing effect of temperature on the vibrational amplitudes of the lattice. Fisher and Renken [36] also presented resistivity curves that demonstrated a departure from linear dependence at approximately 146 ° C, corresponding to changes in electron scattering probability of the lattice. This aligns well with the changes observed in CLE [50, 51] and the elastic constant c_{66} [36]. Fisher and Renken [36] suggested that the combination of Burger's model for the structural change endured upon transformation from the hcp to bcc lattice, and the extreme temperature dependence of c_{66} and $c^{'}$ in both the hcp and bcc phases, respectively, can be viewed as a sudden shift in the direction of the high amplitude thermal vibrations [36] which is the ultimate driver for this transformation. As observed in Figure 2.10, the atoms in the basal planes of the hcp lattice are transformed into the closer packed {110} planes in the bcc lattice which decreases the amplitudes of the shear modes [36].

There are few publications in the literature characterizing the α(hcp) → β(bcc) transformation in pure titanium. This is due to the requirement for *in-situ* evaluation of the transformation in pure titanium. In a study of super-heated Ti films, specimens were heated by a laser pulse at a rate of 10^{11} K.s^{-1} to just below the melting temperature and it was found that the bcc phase nucleated at a rate of 10^{25} m^{-3}.s^{-1} corresponding to a diffusionless and heterogeneous nucleation scenario and the resulting plates grew at rates near 1400 m.s^{-1} [52]. These results are not consistent with a diffusion controlled transformation and rather is in the order of the velocity of elastic shear waves in hcp titanium (approximately 3000 m.s^{-1}) [52]. Conversely, when heated above the transus with lower thermal rates (below 1000 K.s^{-1}), the transformation will occur massively and is diffusion controlled. A study using *in-situ* electron backscatter diffraction (EBSD) was able to observe the α(hcp) → β(bcc) transformation of intragranular and allotriomorphic β grains [11]. Seward *et al.* [11] found that while the intragranular β grains shared a Burgers orientation relationship with the parent α grain and a morphology similar to a military (diffusionless and shear based) transformation, the interface velocities were more consistent with a diffusional transformation. They

observed the fastest interfaces traveled at 10^{-2} m.s^{-1} [11]. This is far less than the mobility expected in a diffusionless shear based transformation (3000 m.s^{-1}). Conversely, unlike the intragranular plates, the grain boundary allotriomorphs did not have morphologies consistent with a military transformation. Instead, the daughter grain is formed via the massive transformation, nucleating and growing along the $\alpha - \alpha$ grain boundaries. These distinct morphologies are presented in the schematic shown in Figure 2.11.

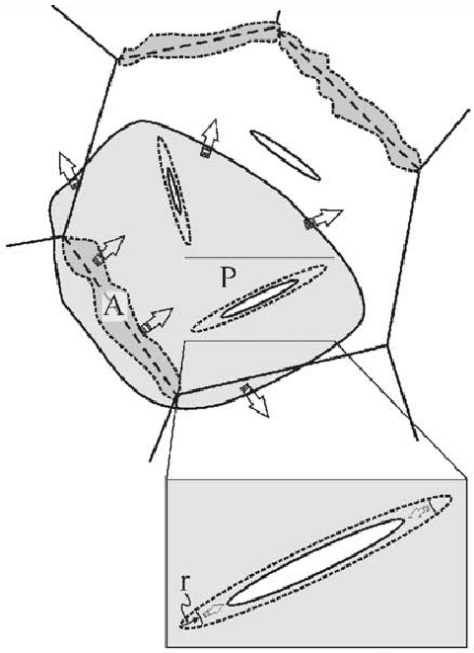

Figure 2.11: Schematic of the competitive growth between two types of β morphology, where the intragranular plates are indicated by P, the allotriomorphs are indicated by A, and the matrix is comprised of α grains. Reprinted and reproduced with permission from Elsevier Publishing Ltd. [11]

Both of these sets of observations [11, 52] are consistent with the mechanism proposed by Fisher and Renken [36] and the data presented above. This is because superheating critically above the transformation temperature would instantaneously change the vibrational directions and intensities in the hcp sublattices, resulting in a shear driven transformation from the hcp lattice to the bcc lattice. Conversely, the lower temperature results of Seward *et al.* [11] shows that while the transformation may have military characteristics, it has kinetics consistent with a diffusional based transformation, which in turn emphasizes the thermal dependence of the changes in vibrations and shear observed over the transformation regime.

2.3.2 Grain growth in β phase titanium

Grain growth is the process where the average size of grains within a polycrystalline aggregate increases. This process is driven by the decrease in free energy that results from a decrease in grain boundary area [12]. The experiment of Gil *et al.* took an initial specimen with an equal area diameter (EQAD) of 54 μm, and isothermally held the specimen at 1000 °C, and 1100 °C. After, EQADs of 358 μm and 429 μm were observed, respectively [12]. The observations of Seward *et al.* [11] also indicated extreme cases of grain growth (demonstrated in Figure 2.12) in commercially pure titanium, where after 110 minutes of holding at 910 °C an area weighted average grain size of approximately 1.2 mm was observed. This extensive grain growth has a direct influence on the number of grains probed during ultrasonic sensing, which leads to an increased contribution of grain orientation effects on the velocity signal. Anisotropy in the hcp and bcc phases in regards to elastic response is explored in Section 2.2.2 and a thorough examination on calculating the effect of orientation and anisotropic response is provided in Section 2.5 .

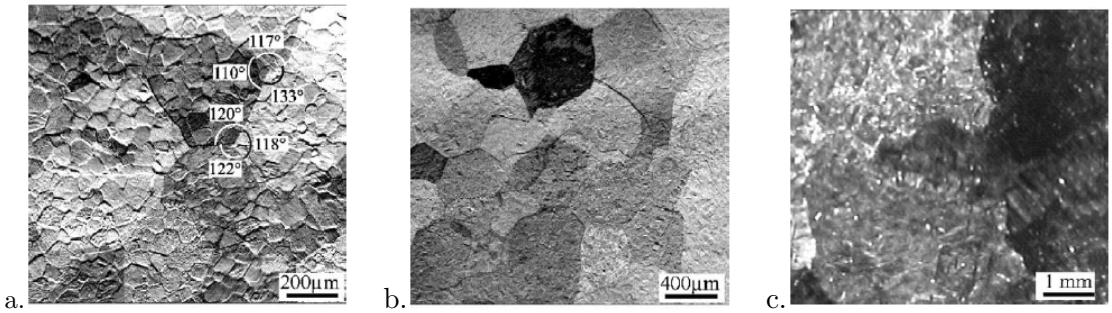

Figure 2.12: Backscatter electron contrast images depicting grain growth of β titanium after a) 30 minutes, b) 1 hr, and c) 4 hrs at temperatures of approximately 910 °C. After 30 minutes, (a) surface relief due to thermal etching of the prior α grain boundaries is still visible, and the β grains are determined only by the orientation contrast. Reprinted and reproduced with permission from Elsevier Publishing Ltd. [11]

2.3.3 The β to α phase transformation

Continuous cooling and the β → α transformation in pure titanium and titanium alloys

The β to α phase transformation observed upon cooling is also heavily effected by the strong thermal dependence of the c_{66} and $c^{'}$ shear constant in both the hcp and bcc phases, respectively (discussed extensively above in Section 2.2 and Section 2.3.1), and much like with the transformation observed

upon heating where the heating rate dictates the character of transformation, the mechanism of transformation upon cooling is affected by the cooling rate.

Depending on the cooling rate from above the β transus, transformations can occur via a variety of mechanisms in titanium alloys. Studies on the phase transformations present in cooling of the α+β alloy Ti -6Al-4V [13], and on commercially pure titanium [14, 15] have demonstrated the effect of cooling on microstructure in α titanium. Ahmed and Rack [13] observed hexagonal martensite formed at high cooling rates. The bcc → hcp martensitic transformation can be described as a result of two basic processes. First, a shuffling of parallel (110) planes in the bcc crystal in the opposite $[1\bar{1}0]$ directions by an amount equal to one sixth of the interplanar spacing between the (110) planes happens. This occurs in conjunction with a pure shear along the {112} family planes of the bcc crystal acting in the $\langle 11\bar{1}\rangle$ directions [53]. The shuffling serves to produce the ABAB stacking characteristic of hexagonal closed packed structures, and the shear serves to convert the irregular hexagonal structure of the (110) bcc planes to a regular hexagonal atomic arrangement with a characteristic angle of $\vartheta = 120°$. The morphology of martensite can be classified as either lath or acicular. Lath martensite refers to a packet martensite structure consisting of 50-100 μm irregular regions containing sub-micron packets of α laths of identical Burgers relationship variant aligned in parallel [10, 54]. Conversely, the acicular structure is characterized as needle-like plates, with adjacent α each having a distinct Burgers relationship variant [10, 54]. Lath martensite has a greater tendency to form in pure titanium or solute lean titanium alloys. The cooling rates at which martensite can be obtained for pure titanium and alloy Ti -6Al-4V are given in Table 2.4.

At slightly slower cooling rates α forms via the massive transformation. The massive transformation involves the original phase decomposing into a new phase of identical composition but different crystal structure, and is a diffusional transformation. Ahmed and Rack [13] observed that decreases in cooling rate corresponded to increases in phase fraction of the observed massive α phase. The massive phase nucleated at grain boundaries and exhibited a blocky appearance. The crystal structure of the massive phase was hexagonal closed packed, where each grain was comprised of a heavily dislocated substructure [13]. As the cooling rate was reduced further, the heterogeneous nucleation of grain boundary primary α was observed to compete with massively formed α phase [13–15]. This resulted in long primary α Widmanstätten plates growing from the grain boundaries with retained β existing between plates. With further decreases in cooling rate, the Widmanstätten

α grew, reaching the center of each β grain. The nucleation of more Widmanstätten plates off of existing plates creates the typically observed basketweave morphology [13–15]. A summary of the effect of cooling rate on observed α morphologies in alloy Ti -6Al-4V and commercially pure titanium is presented in Table 2.4. The optical micrographs depicting the effect of cooling rate on microstructure collected by Kim *et al.* [15] are provided below in Figure 2.13.

Table 2.4: The effect of cooling rate on formed α microstructures when α + β alloy Ti -6Al-4V [13], commercially pure titanium (cp-Ti) [14, 15], and extremely pure (ep-Ti) [14] is cooled from above the transus

	Cooling Rate (°C.s^{-1})			
Microstructure	Ti -6Al-4V [13]	cp-Ti (grade-2)[15]	cp-Ti (grade-4)[14]	ep-Ti [14]
Martensite α′	410	1604	300	1100
Massive α	20 - 410	90 - 1604	30 - 300	350 - 1000
Acicular α	-	58 - 1604	1 - 300	40 - 300
Plate-like	1- 20	1 - 90	1 - 30	1 - 40

The diffusional transformations responsible for the massive and primary α both occur via heterogeneous nucleation, either along existing β grain boundaries or on existing α plates. The case of α precipitation in the near β alloy, Ti-5553, is a complex one, as there are 4 additional alloying elements which will tend to partition. Aluminum, being an α stabilizer, will tend to segregate to the newly formed α precipitates. Conversely, molybdenum, vanadium, and chromium are all β stabilizers and will thus prefer to remain in the β matrix. These elements possess substantial differences in diffusivities relative to one another, leading to significant gradients at the α-β interfaces during nucleation.

Cooling rate have been discussed in the above section as a significant factor in determining the morphology of the transformed microstructure. The cooling rate will also influence compositional partitioning since partitioning is a diffusion dependent effect. The diffusivities of molybdenum, vanadium, and chromium in titanium at 1273K are 3.35 x 10^{-10}, 1.18 x 10^{-9}, and 4.47 x 10^{-9} m^2s^{-1}, respectively [55]. Thus, while molybdenum will be rejected from the newly forming and growing α precipitates, a molybdenum pile-up will occur at α-β interfaces.

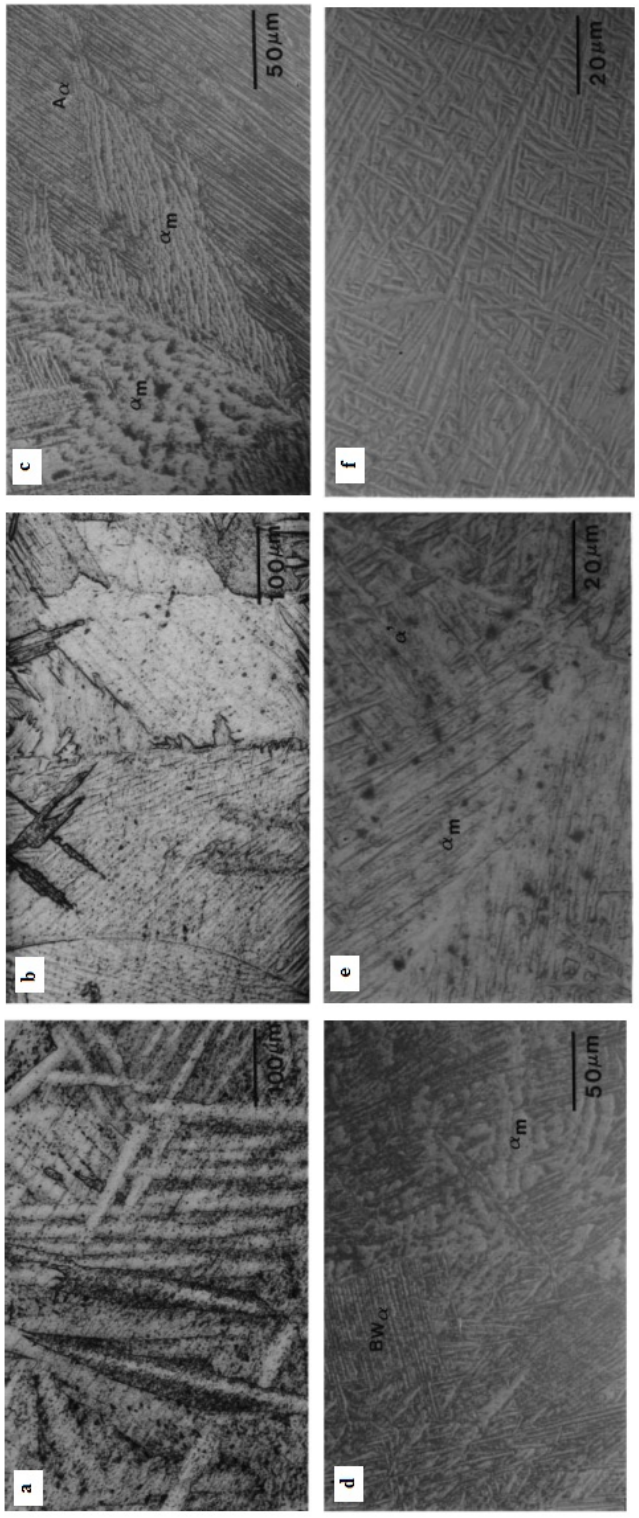

Figure 2.13: Optical micrographs of cp-Ti (grade 2) at cooling rates of a) 1 °C.s^{-1}, b) 50 °C.s^{-1}, c) 91 °C.s^{-1}, d) 356 °C.s^{-1}, e) 651 °C.s^{-1}, and f) 1604 °C.s^{-1}. A_α, M_α, BW_α, and α stand for acicular, massive, basketweave, and martensitic α. Obtained by Kim *et al.* (reprinted and reproduced with kind permission from Springer Science and Business Media) [15]

Isothermal aging in near β titanium alloys

The α precipitation kinetics and mechanism in Ti-5Al-5Mo-5V-3Cr have been explored during low-temperature isothermal holding via *in-situ* resistivity and *in-situ* high energy x-ray diffraction [56], as well as during high temperature holding treatments via *ex-situ* examination such as metallography and hardness testing [57, 58]. Kar *et al.* [57] solution treated and aged at isotherms held at temperatures of 750 °C, 650 °C, and 550 °C for 30 minutes to create a time temperature transformation (TTT) diagram (see Figure 2.14). They observed α volume fractions of 25.5, 37.5, and 32.7 % formed after 30 minutes of undercooled holding at the temperatures 750 °C, 650 °C, and 550 °C, respectively [57]. The α precipitates consisted of allotriomorph grains formed along the $\beta - \beta$ grain boundaries and plate-like precipitates observed throughout the β grains [57] (see Figure 2.15). While limited sources [57, 58] were found documenting high temperature isothermal aging in Ti-5Al-5Mo-5V-3Cr, very similar allotriomorph and plate morphologies were observed in other β alloys such as Ti 17 [18], β21-Ti alloy [59], Ti-15V-3Cr-3Sn-3Al [60] and Ti-8Al-1Mo-1V alloy [61]. Precipitation during isothermal undercooling treatments in near β titanium alloys have been observed to be heterogeneous, occurring initially along grain boundaries, then as plates growing outwards from existing $\alpha - \beta$ interfaces, and finally forming plate packets throughout the β grain.

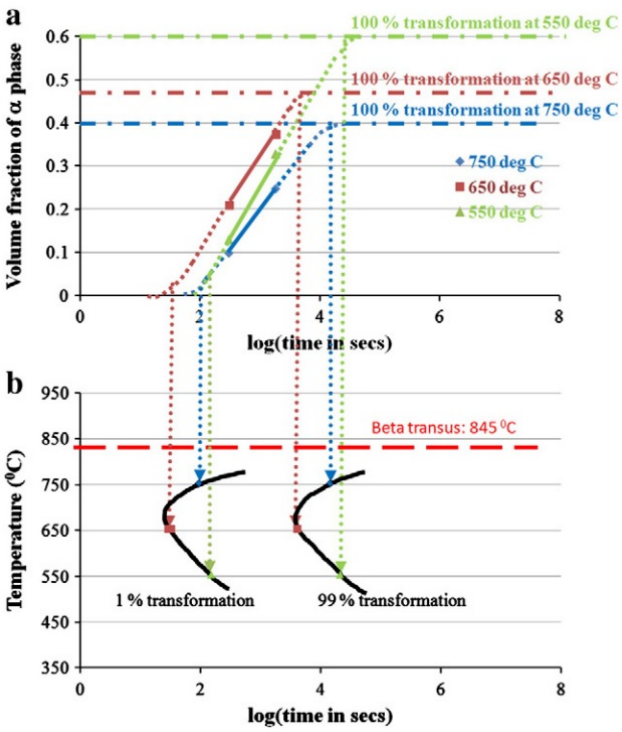

Figure 2.14: Plots showing a) fraction transformed over time held at each isotherm and b) the time temperature transformation (TTT) diagram for Ti-5553 obtained by Kar *et al.* (reprinted and reproduced with permission from Elsevier Publishing Ltd.) [57]

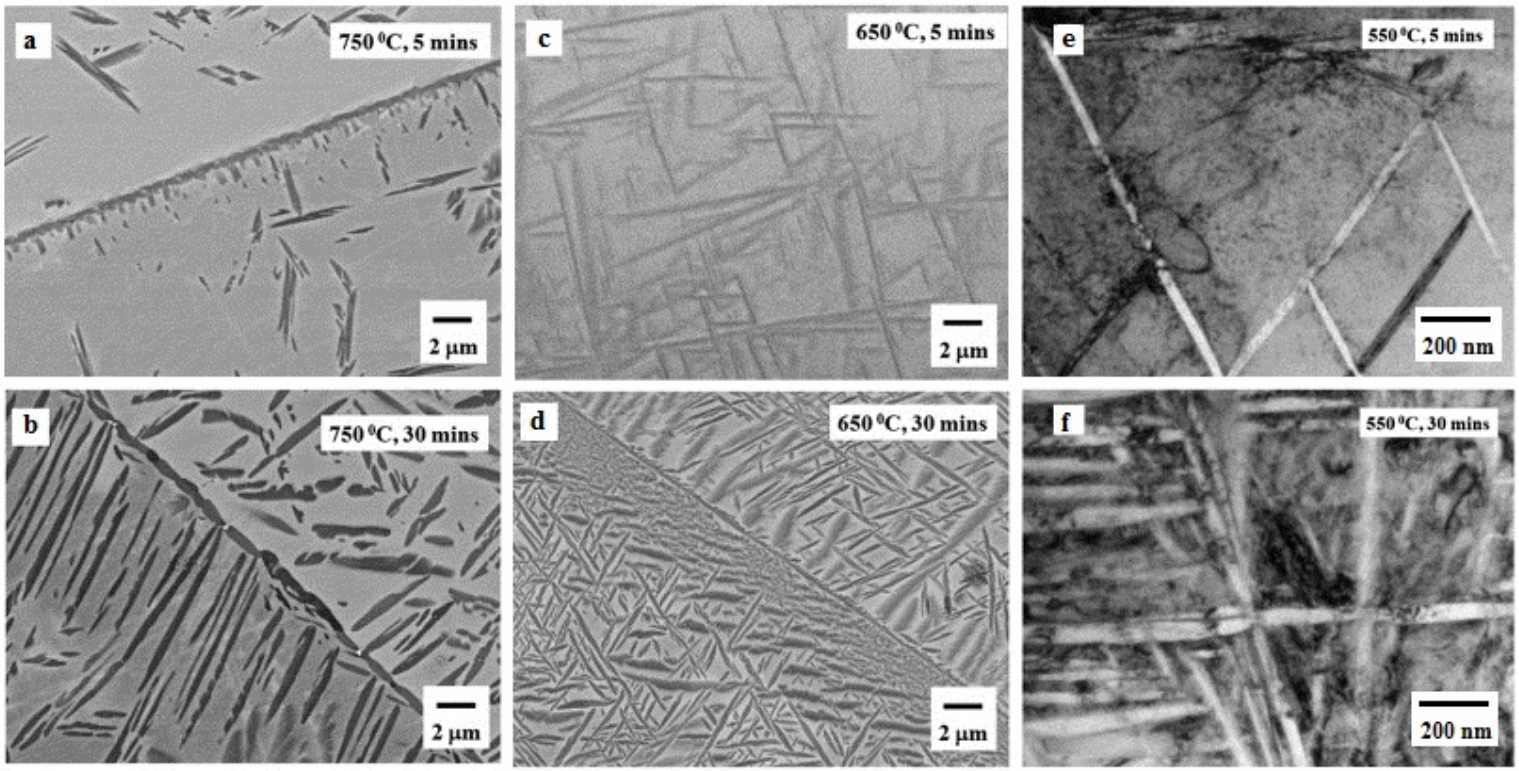

Figure 2.15: SEM backscatter micrographs of microstructures observed after treatment at 750 °C for a) 5 min and b) 30 min, 650 °C for c) 5 min and d) 30 min, and transmission electron microscope images of α plates precipitated after treatment at 550 °C for a) 5 min and b) 30 min. Obtained by Kar *et al.* (reprinted and reproduced with permission from Elsevier Publishing Ltd.) [57]

2.3.4 Observation of phase transformation kinetics in titanium and Ti-5553

Capturing the kinetics of the α to β and the β to α transformation via commonly employed *ex-situ* methods (metallography, SEM) in other systems is not a realistic approach in pure titanium and some low-alloyed titanium materials, since as demonstrated in Sections 2.1.2 and 2.1.3, the transformation is allotropic in nature, and the β phase cannot be retained when quenching from above the transus for many compositions. Furthermore, even quenching to form a martensitic structure, is not readily feasible for many sample geometries, as cooling rates greater than above 1000 °C.s^{-1} have been reported to be necessary to obtain martensite in pure titanium [14, 15] (cf. Section 2.3.3).

Direct SEM/EBSD observation of the α/β transformation in pure titanium performed *in-situ* at high temperatures is possible and can give excellent insight into texture changes and morphological changes observed during transformation [11]. However, this technique is limited to viewing a small area on the extreme surface of the specimen and is unsuitable for measurement of the bulk transformation kinetics. Furthermore, the resolution is limited by the rastering time for the electron beam to sample the entire area, and, as such, small area sizes must be selected to resolve fast transformations. *In-situ* neutron or x-ray diffraction [19, 20] measurements made during continuous heating and cooling are another option but are limited by the acquisition time of the technique (particularly for neutron diffraction) [21] and by the rapid grain growth that occurs in the β-phase at high temperature, where having a small sample of large grains of particular orientation can cause issues with peak detection. *In-situ* electrical resistivity measurements have been shown to be viable for measurements in commercially pure titanium but the method becomes more difficult to interpret in alloys where scattering from interfaces and solute atoms, which redistribute on transformation, can not be neglected [14, 15]. Furthermore, the departure from linearity observed in single phase α resistivity data corresponding to changes in the scattering probability of the hcp lattice [36] can also complicate the measurement. Dilatometry is also made difficult due to the anisotropy present in the coefficients of thermal expansion along the c-axis and a-direction in the hcp phase [50, 51], indicating that the measurement would be texture and grain size sensitive.

Conversely, capturing the kinetics of the α to β and the β to α transformation via commonly employed *ex-situ* methods (metallography, SEM) in Ti-5553 is much easier, due to its ability as

a metastable alloy to retain the β phase upon quenching from above the β-transus temperature. However, as Ti-5553 is intended for landing gear applications, and often undergoes forging and aging treatments [10], a non-contact, *in-situ*, and industrially feasible method to monitor phase transformations during complex thermo-mechanical processing steps would be highly beneficial. The need for controlling the α + β microstructure was discussed in Section 2.1.4. Recently, an extensive study conducted by Coakley *et al.* [35] monitored ω and α aging via *ex-situ* approaches such as atom probe tomography (APT), x-ray diffraction (XRD), and transmission electron microscopy (TEM), as well as *in-situ* small angle neutron scattering (SANS). However, the authors acknowledged the modeling of SANS data is not simple, and requires complimentary microscopy, as well as a neutron source [35]. Laser ultrasonics could be an additional technique to help monitor the complex phases and microstructures that develop in Ti-5553 and commercially pure titanium. The basis of this technique is explored in the following section (Section 2.4).

2.4 Laser ultrasonics

Conventional ultrasound analysis has been used to measure thickness, detect cracks and voids, inspect weld quality, and to characterize materials [62]. This technique involves a piezoelectric transducer that is capable of emitting and receiving ultrasound pulses. While ultrasonic testing has been a very successful and cost effective non-destructive technique, it is subject to a variety of constraints. A key limiting factor is the need to have the specimen either immersed in a tank or have direct contact to achieve ultrasonic coupling [62]. This requirement limits the application of ultrasound to low temperature scenarios in the context of having the specimen immersed, or, if high temperatures are required, direct contact must be made between the transducer and specimen. Both of these constraints place impositions on monitoring microstructural changes *in-situ* during complex thermomechanical processing steps. Furthermore, the bandwidth of the piezo-transducers is limited, which limits the shape of the specimen to pieces with limited concavity.

These limitations can be negated via the use of laser light for the generation and detection of ultrasound in a material [62, 63]. Advantages of laser ultrasonic measurement includes the fact that it is completely non-contact, effective at high temperatures, and that it has a high precision for the capture of sound wave velocity [63]. Due to the versatility stemming from the non-contact nature,

laser ultrasonics has been successfully utilized in numerous applications, including determining elastic constants [63, 64], observing recrystallization [65–68] and phase transformations [67, 69, 70], measuring grain size [68, 71, 72], and monitoring strip and specimen thicknesses [63, 67]. The following section describes the principle for generation and detection of ultrasound with lasers, as well as outline examples of the applications for velocity-based and attenuation-based monitoring.

2.4.1 Laser generation and detection of ultrasonic pulse

The generation of ultrasound by a laser source can be either caused by a thermo-elastic mechanism or an ablation mechanism [62]. The thermo-elastic mechanism involves the laser light being absorbed to some depth into the material and is completely non-destructive [62, 73]. This produces heat, causing the material to expand. This expansion induces strain and a corresponding stress that is the source of the waves propagating through the material and along the material's surface [62, 73]. Thermo-elastic generation is very successful at generating surface waves when the source beam is focused on the surface as a small point. This creates a circle wave of cylindrical symmetry emitting from the spot [74].

By increasing the energy density, the material surface will melt and eventually a thin layer of material at the surface will vaporize. Upon vaporization, the vapor (and surrounding air if present), will ionize. This ionization creates a plasma cloud that expands away from the point of interaction. This expansion of plasma creates a reactionary force in the specimen perpendicular to the surface causing a displacement that propagates through the material as an ultrasound pulse with primarily longitudinal components. This technique is not purely non-destructive, as with each instance of ablation, a thin layer of metal material is removed from the sample surface. After prolonged treatment, a small crater of diameter equal to the beam diameter may be visible upon the sample surface [62].

A second laser will illuminate the sample surface continuously or in pulses of sufficient duration to detect the ultrasonic signal of interest. The light is either scattered or reflected upon hitting the surface and can be collected by an interferometer. The interferometer detects the microscopic changes in the sample surface caused by the arrival of the ultrasound wave at the detection surface [75]. While there are many interferometry techniques such as the confocal Fabry-Perot interferometer [76] and the Michelson interferometer [75], the two-wave beam mixing method [77] is the

interferometer set up used for this thesis work. In the two-wave beam mixing method, the detection beam first strikes the surface and is scattered producing a signal beam (S_o). The signal beam interferes with a plane wave beam sourced directly from the laser called the pump beam (P_o). This interference occurs within a photo-refractive crystal. The general schematic of an optical set-up sensitive enough to detect the phase shifts in the signal beam produced by the ultrasonic induced displacements on the sample surface is provided in figure 2.16.

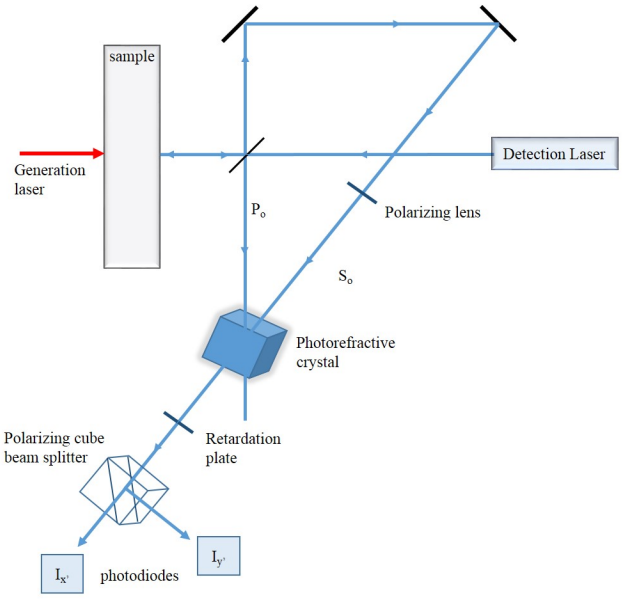

Figure 2.16: simplified schematic of the optical set-up for two-wave beam mixing method interferometry presented in [75]

2.4.2 Interpretation of waveform signal

After collection and demodulation using the active, two beam mixing interferometry approach, the output can be displayed as an amplitude (in voltage) plotted over time, as shown in Figure 2.17. The amplitude is proportional to the monitored surface displacement.

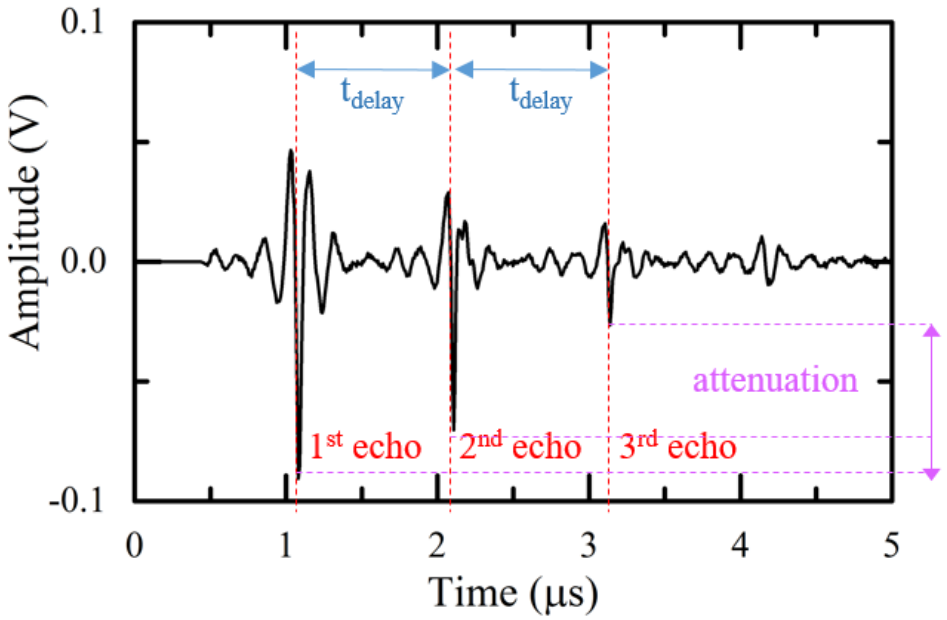

Figure 2.17: Example of a waveform depicting compressive and shear echo signals in a 3 mm thick commercially pure titanium specimen

The signal presented in Figure 2.17 corresponds to a set up where the detection and generation lasers are directed at the same surface (meaning the wave must travel a distance equal to twice the thickness of the specimen to be measured). Shortly after generation, the first compressive echo can be observed. The compressive echos correspond to the longitudinal component of the planar wavefront. The appearance of the first echo means after generation, the wavefront has traveled through the material to the point where it is being monitored as a surface displacement.

The compressive echos provide two essential parameters. The first is the time delay. When evaluating longitudinal velocity, the time delay is the time between two compressive echos and corresponds to the time needed for the wavefront to travel from the original surface, through the medium and back again to be measured. By knowing the time delay and the thickness of the specimen being observed, the longitudinal sound velocity can be calculated for the material. The second key parameter is the attenuation. Attenuation is the loss in amplitude observed over time. This is affected by the average grain size in a given material, as well as the texture in anisotropic materials. Attenuation is due to the elastic scattering of the longitudinal wave by grains [62, 63, 66, 68, 71, 72].

Ultrasonic velocity measurement in observations of texture and phase transformation

Ultrasonic velocity is a function of the temperature, texture and phase composition of a material, as all three factors will affect the aggregate elastic properties and density of the material.

The work of Dubois, Moreau and Bussière [70] also investigated extensively the phase transformations in steels. They observed that the ferromagnetic-paramagnetic transition that occurs at the Curie temperature (750 °C) affected the ultrasound velocity noticeably. They were also able to observe hysteresis in velocity signal depicting transformations in steels with carbon concentrations above 0.05 %. However, what is of interest to this particular study is their modeling of velocity based on textural changes observed in the steel specimens. Dubois *et al.* [70] calculated the orientation distribution coefficients (ODC) from the ultrasonic data of the as-received state. This was then used to compute the bulk texture of the austenite phase, and the returning ferrite phase after one cycle of continuous treatment using the Kurdjumov-Sachs relationship (KSR). This model approach was built upon the assumption that each of the 24 variants defined under the KSR are equally probable to form and that the number of grains within the probed volume is large enough to allow for each variant to be selected equally often statistically and is truly a statistically relevant bulk texture. They cited a lack of grain growth during the duration of the treatments to ensure that the assumption is a good approximation. Under these assumptions, Dubois *et al.* [70] modeled the expected velocity based on the as-received texture information and found it to be comparable to the experimentally determined values. Velocity profiles obtained via laser ultrasonics were also used to monitor recrystallization and phase transformations in aluminum[65], low carbon steels [67], Ti-6Al-4V [2] and zirconium [78]. To date, laser ultrasound has seen limited usage in the context of evaluating titanium and titanium alloys [1, 2]. In particular, this technique is of interest in evaluating transformation kinetics in commercially pure titanium since the high temperature bcc phase is not stable at room temperature for *ex-situ* evaluation.

2.5 Ultrasonic wave propagation in metals

2.5.1 Calculation of velocity from the Christoffel equation

In an elastic medium the velocity of an ultrasonic pulse is dependent on the elastic stiffness tensor. In particular, the Christoffel equation can be used to calculate elastic wave velocity in an anisotropic medium and is derived from solving for the characteristic equation of the wave equation after substituting in Hooke's law [79]. For a unit vector of propagation direction n, the Christoffel tensor is given by [79, 80]:

$$\langle \mathrm{T} \rangle = \sum_{\mathrm{j}=1}^{3} \sum_{\mathrm{l}=1}^{3} \mathrm{c}'_{\mathrm{ijkl}} \mathrm{n_j n_l} \tag{2.22}$$

Where $\mathrm{c_{ijkl}}$ is the 4^{th} order crystallographic tensor describing the elasticity in a given media, and n is the propagation direction of the pulse.

As the elastic tensor is symmetric, the Christoffel tensor is also symmetric, and thus is invariant upon altering the sign of the propagation direction. The elastic strain energy of a stable crystal is always positive and real, the the eigenvalue solutions to the 3 x 3 Christoffel tensor are also real and positive, and are related to wave velocities propagating through the crystal. The P wave velocity, S1 wave velocity, and S2 wave velocity are related the square root of the fraction of the first, second and third eigenvalue over density, respectively [80].

$$\mathrm{v_P} = \left(\frac{\lambda_1}{\rho} \right)^{0.5} \tag{2.23}$$

$$\mathrm{v_{S1}} = \left(\frac{\lambda_2}{\rho} \right)^{0.5} \tag{2.24}$$

$$\mathrm{v_{S2}} = \left(\frac{\lambda_3}{\rho} \right)^{0.5} \tag{2.25}$$

The three polarization directions, or displacement vectors, are the eiganvalue solutions of the Christoffel tensor. The three displacement vectors are mutually perpendicular since the Christoffel tensor is symmetric. The p-wave displacement direction is parallel to the propagation direction,

and signifies the longitudinal component of the wave [80]. Conversely, the two S wave components are perpendicular to the propagation direction (n), and are termed quasi-S waves [80].

2.5.2 Ultrasound velocity in an isotropic medium

The stiffness matrix of an isotropic continuum ($[c]_{iso}$) only contains the two independent elasticity parameters c_{11} and c_{44}, and is defined as [44, 81]:

$$[c]_{iso} = \begin{bmatrix} c_{11} & c_{11}-2c_{44} & c_{11}-2c_{44} & 0 & 0 & 0 \\ c_{11}-2c_{44} & c_{11} & c_{11}-2c_{44} & 0 & 0 & 0 \\ c_{11}-2c_{44} & c_{11}-2c_{44} & c_{11} & 0 & 0 & 0 \\ 0 & 0 & 0 & 2c_{44} & 0 & 0 \\ 0 & 0 & 0 & 0 & 2c_{44} & 0 \\ 0 & 0 & 0 & 0 & 0 & 2c_{44} \end{bmatrix} \tag{2.26}$$

The $[c]_{iso}$ matrix is invariant upon rotation, meaning that if rotated by an arbitrary direction, the stiffness matrix will not change.

The two independent elasticity parameters are often expressed as Lamé parameters [81]:

$$\lambda_o = c_{11} - 2c_{44} \tag{2.27}$$

$$\mu = 2c_{44} \tag{2.28}$$

The two independent Lamé parameters are closely related to the Eigenvalues of the elasticity matrix, where μ can also be referred to as G and is the shear modulus. The elasticity matrix can

be rewritten as [81]:

$$[c]_{\text{iso,Lamé}} = \begin{bmatrix} \lambda_o + 2\mu & \lambda_o & \lambda_o & 0 & 0 & 0 \\ \lambda_o & \lambda_o + 2\mu & \lambda_o & 0 & 0 & 0 \\ \lambda_o & \lambda_o & \lambda_o + 2\mu & 0 & 0 & 0 \\ 0 & 0 & 0 & \mu & 0 & 0 \\ 0 & 0 & 0 & 0 & \mu & 0 \\ 0 & 0 & 0 & 0 & 0 & \mu \end{bmatrix} \tag{2.29}$$

Upon expansion of $[c]_{\text{iso,Lamé}}$ into its corresponding 4^{th} order elasticity tensor [82] and substitution of the elasticity tensor into Equation 2.22, and recalling that the P-wave velocity can be defined by Equation 2.23, it can be seen the velocity of P-waves is related to elastic moduli in isotropic media by [83]:

$$v_{\text{P,iso,single}} = \left(\frac{\lambda_o + 2\mu}{\rho}\right)^{0.5} \tag{2.30}$$

Where $\lambda_o + 2\mu$ can be defined as the P-wave modulus (λ), and thus, alternatively, velocity can be defined as:

$$v_{\text{P,iso,single}} = \left(\frac{\lambda}{\rho}\right)^{0.5} \tag{2.31}$$

2.5.3 Rotation of elastic stiffness tensors

The hcp unit cell of titanium has anisotropic elastic properties (cf. Section 2.2.2). Ultrasound velocity is approximated to be proportional to the square root of the fraction P-wave modulus of a material over it's density. Thus, any anisotropy present in the elastic properties of the material will produce a anisotropic response in the velocity. The velocity of a wave in any given direction of the crystal can be evaluated by applying the appropriate rotation to the stiffness tensor prior to computation of the P-wave velocity.

Each orientation given in Bunge Euler notation describing a discrete volume in the orientation

distribution (OD) must be converted to Bond notation. This was accomplished by transforming first the three Bunge Euler angles (φ_1, φ_2, Φ) to Roe angles (ψ, ϑ, φ_R) via:

$$\psi = \begin{cases} \varphi_1 & \Phi = 0 \\ \varphi_1 + \frac{\pi}{2} & \Phi \geq \pi \\ \varphi_1 + \frac{3\pi}{2} & \Phi \leq \pi \end{cases}; \quad \vartheta = \begin{cases} \Phi & \Phi = 0 \\ 2\pi - \Phi & \Phi \geq \pi \\ \Phi & \Phi \leq \pi \end{cases}; \quad \varphi_R = \begin{cases} \varphi_2 & \Phi = 0 \\ \varphi_2 + \frac{3\pi}{2} & \Phi \geq \pi \\ \varphi_2 + \frac{\pi}{2} & \Phi \leq \pi \end{cases} \tag{2.32}$$

Next, it is necessary to convert the above Roe angles to Bond angles:

$$\xi_z = -\varphi_R; \qquad \eta = -\vartheta; \qquad \xi_p = -\psi \tag{2.33}$$

The Bond angle description for each discrete orientation can be used to rotate the stiffness matrix [c] to find the corresponding matrix responsible for describing the elastic properties at that given orientation. There are 3 rotations in total applied: one about the z axis, one about the new y axis, and finally one about the newly formed z axis. Provided the absolute value of ξ_z, η, and ξ_p are greater than zero, the following rotation can be applied to the stiffness matrix [79]:

$$[c'] = [M_z][M_y][M_z][c][M_z]^T[M_y]^T[M_z]^T \tag{2.34}$$

The rotation matrix $[M_z]$ is defined as [79]:

$$[M_z] = \begin{bmatrix} \cos(\xi_z)^2 & \sin(\xi_z)^2 & 0 & 0 & 0 & \sin(2\xi_z) \\ \sin(\xi_z)^2 & \cos(\xi_z)^2 & 0 & 0 & 0 & -\sin(2\xi_z) \\ 0 & 0 & 1 & 0 & 0 & 0 \\ 0 & 0 & 0 & \cos(\xi_z) & -\sin(\xi_z) & 0 \\ 0 & 0 & 0 & \sin(\xi_z) & \cos(\xi_z) & 0 \\ \frac{-\sin(2\xi_z)}{2} & \frac{\sin(2\xi_z)}{2} & 0 & 0 & 0 & \cos(2\xi_z) \end{bmatrix} \tag{2.35}$$

The rotation matrix $[M_y]$ is defined as [79]:

$$[M_y] = \begin{bmatrix} \cos(\eta)^2 & 0 & \sin(\eta)^2 & 0 & -\sin(2\eta) & 0 \\ 0 & 1 & 0 & 0 & 0 & 0 \\ \sin(\eta)^2 & 0 & \cos(\eta)^2 & 0 & \sin(2\eta) & 0 \\ 0 & 0 & 0 & \cos(\eta) & 0 & \sin(\eta) \\ \frac{\sin(2\eta)}{2} & 0 & \frac{-\sin(2\eta)}{2} & 0 & \cos(2\eta) & 0 \\ 0 & 0 & 0 & -\sin(\eta) & 0 & \cos(\eta) \end{bmatrix} \tag{2.36}$$

Now, each rotated stiffness matrix [c'] must be converted back to the 4^{th} order crystallographic tensor $[c_{ijkl}]$, which can then be converted to the Christoffel Tensor $\langle T \rangle$ by Equation 2.22 (Section 2.5.1). The longitudinal, or P-wave, velocity is then given by Equation 2.23 (Section 2.5.1).

2.5.4 Elastic properties of polycrystalline aggregates in the isotropic assumption

Isotropic polycrystalline aggregates of hcp crystals

The stiffness matrix for an hcp crystal is denoted by $[c]_{hcp}$ throughout the following sections and is given by:

$$[c]_{hcp} = \begin{bmatrix} c_{11} & c_{12} & c_{13} & 0 & 0 & 0 \\ c_{12} & c_{11} & c_{13} & 0 & 0 & 0 \\ c_{13} & c_{13} & c_{33} & 0 & 0 & 0 \\ 0 & 0 & 0 & c_{44} & 0 & 0 \\ 0 & 0 & 0 & 0 & c_{44} & 0 \\ 0 & 0 & 0 & 0 & 0 & c_{66} \end{bmatrix} \tag{2.37}$$

Where $c_{66} = \frac{c_{11}-c_{12}}{2}$.

The macroscopic elastic properties of a polycrystal can be calculated under the assumption of an isotropic polycrystalline aggregate. This corresponds to the aggregate consisting of small grains of random orientation, where there is a sufficient grain count for the sample as a whole to be considered isotropic in elastic property. Two methods of calculating the polycrystalline averages of macroscopic properties are typically employed: the Voight and Reuss methods [82, 84, 85].

In 1889, Voight [84] chose to analyze the stiffness constants [c] under the assumption that

homogeneous strain was maintained throughout the stressed polycrystal in all directions. Via 3-D integration, under the isotropic polycrystalline assumption, Voight derived general equations for the bulk modulus (B^{Voight}) and the shear modulus (G^{Voight}) [82, 84].

The bulk modulus accounts for a volume change with no observed shape change, and is described as:

$$B^{Voight} = \frac{2c_{11} + c_{33} + 4c_{13} + 2c_{12}}{9} \tag{2.38}$$

Conversely, the shear modulus accounts for a shape change with no observed volume change, and is described as:

$$G^{Voight} = \frac{3.5c_{11} + c_{33} - 2c_{13} - 2.5c_{12} + 6c_{44}}{15} \tag{2.39}$$

Contrarily, Reuss [85] chose to analyze the compliances [s] under the assumption that homogeneous stress was maintained throughout the strained polycrystal. Under the isotropic polycrystalline assumption, Reuss also derived general equations for: the bulk modulus (B^{Reuss}) and the shear modulus (G^{Reuss}) [82].

The Reuss bulk modulus is described as [82, 85]:

$$B^{Reuss} = [2s_{11} + s_{33} + 4s_{13} + 2s_{12}]^{-1} \tag{2.40}$$

Conversely, the shear modulus accounts for a shape change with no observed volume change, and is described as [82, 85]:

$$G^{Reuss} = 15\,[14s_{11} + 4s_{33} - 8s_{13} - 10s_{12} + 6s_{44}]^{-1} \tag{2.41}$$

In practice, experimental measurements suggest that the elastic response lies between the bounds set forth by the Voight [84] and Reuss [85] assumptions, and thus an arithmetic average, called the Hill average(B^{Hill}, G^{Hill}), of the two is used. The pressure wave (P-wave) modulus can then be calculated as[83]:

$$\lambda^{\text{Hill}} = \text{B}^{\text{Hill}} + \frac{4}{3}\text{G}^{\text{Hill}} \tag{2.42}$$

Isotropic polycrystalline aggregates of bcc crystals

The stiffness matrix for a bcc crystal is denoted by $[\text{c}]_{\text{bcc}}$ throughout the following sections and is given by [44]:

$$[\text{c}]_{\text{bcc}} = \begin{bmatrix} \text{c}_{11} & \text{c}_{12} & \text{c}_{12} & 0 & 0 & 0 \\ \text{c}_{12} & \text{c}_{11} & \text{c}_{12} & 0 & 0 & 0 \\ \text{c}_{12} & \text{c}_{12} & \text{c}_{11} & 0 & 0 & 0 \\ 0 & 0 & 0 & \text{c}_{44} & 0 & 0 \\ 0 & 0 & 0 & 0 & \text{c}_{44} & 0 \\ 0 & 0 & 0 & 0 & 0 & \text{c}_{44} \end{bmatrix} \tag{2.43}$$

The P-wave modulus ($\lambda = \lambda_{\text{o}} + 2\mu$) and shear modulus ($\mu = \text{G}$) are given under the Voight assumption that homogeneous strain was maintained throughout the stressed polycrystal as [86]:

$$\lambda^{\text{Voight}} = \text{c}_{11} - \frac{2}{5}\left(\text{c}_{11} - \text{c}_{12} - 2\text{c}_{44}\right) \tag{2.44}$$

$$\mu^{\text{Voight}} = \text{c}_{44} + \frac{1}{5}\left(\text{c}_{11} - \text{c}_{12} - 2\text{c}_{44}\right) \tag{2.45}$$

Conversely, if it is assumed that homogeneous stress was maintained throughout the polycrystal, the Reuss averaged Lamé parameters are given as [86]:

$$\lambda^{\text{Reuss}} = \frac{2\left(\text{s}_{11} + \text{s}_{12} - \frac{(\text{s}_{11} - \text{s}_{12} - 0.5\text{s}_{44})}{5}\right)}{\left(\left(\text{s}_{11} + 2\text{s}_{12}\right)\left(\text{s}_{44} + \frac{4}{5}\left(\text{s}_{11} - \text{s}_{12} - 0.5\text{s}_{44}\right)\right)\right)} \tag{2.46}$$

$$\mu^{\text{Reuss}} = \left(\text{s}_{44} + \frac{4}{5}\left(\text{s}_{11} - \text{s}_{12} - 0.5\text{s}_{44}\right)\right)^{-1} \tag{2.47}$$

2.5.5 Ultrasound velocity in a textured polycrystalline aggregate

Until this section, the effect of temperature and orientation on velocity had only been considered for a single crystal or a polycrystalline aggregate in the isotropic assumption (i.e. weakly textured). However, the section through which the planar, longitudinal wavefront travels through in the LUMet scenario contains many grains of varying orientations. Thus, it is prudent to effectively describe the orientation distribution (OD), to determine the volume fraction of grains at a given orientation, and to calculate a weighted average of the Christoffel tensor to compute a velocity representative of the aggregate's texture.

At each set of Euler angles describing a bin in the OD, the intensity of occurrence can be used to calculate the volume fraction of grains that possess that current orientation [87].

$$f(i) = \frac{I\Delta\varphi_1\Delta\varphi_2\left(\cos\left(\Phi - \frac{\Delta\Phi}{2}\right)\right)}{\pi^2} \tag{2.48}$$

$$V_m(i) = \frac{f(i)}{\sum_{i=1}^{n} f(i)} \tag{2.49}$$

Where each iteration, i, corresponds to a discrete orientation, $\Delta\varphi_1$, $\Delta\varphi_2$, $\Delta\Phi$ are equal to $\frac{\pi}{180}$.

This results in a volume fraction for each discrete orientation occurrence mapped in the OD, where each discrete orientation occurrence can be used to rotate the given stiffness tensor, and thus Christoffel tensor, to one descriptive of the elastic response at that given orientation. This creates a weighted distribution of possible Christoffel tensors, where volume fraction serves as the weight.

The polycrystalline averages can be calculated under the Voight, Reuss or Hill convention [80]. Under the Voight convention, it is assumed homogenous strain was maintained in all directions throughout the polycrystal as it is stressed [82]. This corresponds to the induced tensor (strain) at every position is set to equal the macroscopic induced tensor of that specimen [82, 84]. The Voight average of the Christoffel tensor, $\langle T\rangle^{\text{Voight}}$, is defined as the volume weighted average of the individual tensors (T) at a given orientation (g_m) with a volume fraction of V_m [80]:

$$\langle \mathrm{T} \rangle^{\mathrm{Voight}} = \sum_{\mathrm{m}=1}^{\mathrm{M}} \mathrm{V_m T}\left(\mathrm{g_m}\right) \tag{2.50}$$

Conversely, the Reuss average employs the assumption of homogeneous stress [82, 85]. This implies that the applied tensor (stress) at each location is set to equal the macroscopic applied tensor of the entire specimen. The Reuss average of the Christoffel tensor, $\langle \mathrm{T} \rangle^{\mathrm{Reuss}}$, is then defined as the volume weighted average of the inversed individual tensors (T^{-1}) at a given orientation ($\mathrm{g_m}$) with a volume fraction of $\mathrm{V_m}$ [80]:

$$\langle \mathrm{T} \rangle^{\mathrm{Reuss}} = \left[\sum_{\mathrm{m}=1}^{\mathrm{M}} \mathrm{V_m T^{-1}}\left(\mathrm{g_m}\right) \right]^{-1} \tag{2.51}$$

Empirical observations have demonstrated that tensor of an aggregate material lies in between the Voight and Reuss assumptions, and thus the Hill average can be utilized:

$$\langle \mathrm{T} \rangle^{\mathrm{Hill}} = \frac{1}{2} \left[\langle \mathrm{T} \rangle^{\mathrm{Voight}} + \langle \mathrm{T} \rangle^{\mathrm{Reuss}} \right] \tag{2.52}$$

Thus, the average Christoffel tensor, and therefore the average longitudinal velocity, of a polycrystalline aggregate can be computed at a given temperature by substituting the Hill averaged Christoffel tensor (Equation 2.52) into Equations 2.22 and 2.23.

2.5.6 Velocity in the two phase region

The ultrasonic velocity dependence on the phase fraction of a multiphase compound consists of numerous inputs, including the morphology of phases, elastic constants, texture effects, and density. However, Kruger and Damm [69] proposed that for constituent phases of similar elastic properties and densities, complex modeling can be simplified to a volume fraction-weighted-average of individual constituent velocities independent of morphology and obtained by the rule of mixtures.

For a general case considering a dual phase system, this rule of mixtures can be taken on velocity

as:

$$v = f_\alpha v_\alpha + f_\beta v_\beta \tag{2.53}$$

Kruger and Damm applied the ultrasonic lever-rule method to the monitoring of austenite decomposition into ferrite [69]. During measurement they observed a monotonic increase as the steel was cooled from the austenite phase. Because the specimen was being continuously cooled, it was necessary to compute the single phase profile for ferrite and austenite region, so that these curves could be averaged and compared to the experimentally obtained laser ultrasound results. The austenite fraction over temperature profile was obtained using laser ultrasonics and dilatometry, and were found to be comparable[69]. Section 5 explores this assumption in greater detail using a Finite Element Model and compares various averaging methods.

Chapter 3

Scope and Objectives

An integral step in ensuring titanium and its alloys meet their demanding performance criteria is controlling the mechanical properties via strict control of the microstructure. In particular, the various phase transformations present in titanium were shown to greatly alter the microstructure in titanium and its alloys. Thus, it would be prudent to monitor and evaluate phase transformations in titanium during thermo-mechanical processing. However, phase transformations in titanium occur at a high temperature, and in the context of commercially pure titanium (cp-Ti) and some Ti-alloys, the high temperature phase (β) does not exist at room temperature. As such, conventional methods for monitoring and studying phase transformation kinetics are not always viable for this material.

As discussed in the previous chapter, Laser ultrasonics for metallurgy (LUMet) provides an option for monitoring phase transformations during thermo-mechanical processing and, to date, only two studies have attempted to use this technique on titanium alloys [1, 2]. The objective of this work is to evaluate the feasibility of LUMet as a non-destructive tool for monitoring the α/β phase transformation kinetics in pure and near-β titanium alloy.

In order to achieve this goal, three studies were conducted. Firstly, a finite element modeling (FEM) approach was used to simulate the ultrasound response in a simulated 2 dimensional microstructure for a 2-phase material, in order to understand the effects of precipitate spatial arrangement and increasing phase fraction on the velocity signal. In particular, this initial study identified how the measured ultrasonic velocity could be obtained from the phase fraction and the respective properties of the two phases.

Secondly, cp-Ti specimens were subjected to continuous heating and cooling treatments through the β transus (882 °C). Cp-Ti was selected in order to monitor a 100% $\alpha \rightarrow \beta$ transformation, and thus the largest possible change in velocity due phase transformation could be detected and resolved with the ultrasound technique. Continuous heating as opposed to isothermal holding was selected to minimize heating and cooling overshoot error, since the α/β transformation in cp-Ti is allotropic and would begin before the isotherm was established in the system. Specimens were cycled 5 times to determine repeatability of the velocity response and examine the effects of bulk texture changes on the velocity profile. *Ex-situ* metallography and electron backscatter diffraction (EBSD) were employed to analyze the microstructure and texture of the specimens before and after treatment.

Finally, Ti-5553 specimens were subjected to a 15 minute hold at 900°C to fully transform the alloy to the β phase, cooled at 7 °C.s^{-1} to 700°C and then held for 5, 10, 33, 53, 75, or 180 minutes before being quenched. During each isotherm, LUMet was employed to monitor the α precipitation kinetics *in-situ*. *Ex-situ* metallography and EBSD provided a direct method for observing microstructural evolution, as well as the nucleation and growth kinetics during the precipitation process, and was correlated against the LUMet results. The isothermal holding temperature (700°C) for precipitation was selected to provide the fastest rate of transformation according to the published time temperature transformation (TTT) diagram [57]. Other isothermal holding temperatures located either above or below this peak would result in extensive treatment and monitoring times needed to reach equilibrium, and can result in signal degradation during LUMet observation due to surface damage endured over this time.

Chapter 4

Experimental Methodology

4.1 As-received materials

4.1.1 Commercially pure titanium

A commercially pure (99.7 wt% Ti) titanium (cp-Ti) plate purchased from Alfa-Aesar was used for this study. The primary impurities in this material were oxygen (1800 wt.ppm), iron (500 wt.ppm), nitrogen (100 wt.ppm) and hydrogen (15 wt.ppm). Thin plate specimens having dimensions of 60 x 10 x 3 mm were machined from the as-received plate for the laser ultrasonic experiments, with the plate's normal direction (ND) corresponding to the smallest specimen dimension and the rolling direction (RD) to the largest (Figure 4.1). The 3 mm thickness of the specimens provided a good compromise when optimizing the ultrasonic response in the specimens since it was not thick enough to cause significant attenuation (where the second and third echos would no longer be resolved) and was not so thin as to cause an overlap between subsequent echos.

4.1.2 As-received Ti-5Al-5Mo-5V-3Cr

The material used for this study is a near-β titanium alloy (Ti- 5553) provided by UTC Aerospace Systems and developed by Verkhana Salda Metallurgical Production Association of composition: 5.34 - 5.43 wt.% Al, 4.84 - 5.18 wt.% V, 4.96 - 5.12 wt.% Mo, and 2.73 - 2.86 wt.% Cr. In addition, the alloy contains approximately 0.3 - 0.34 wt.% Fe, 0.029 - 0.031 wt.% Si, 0.003 - 0.008 wt.% Zr, 0.148 - 0.151 wt.% O, 0.0011 - 0.0026 wt.% H_2, and 0.006 - 0.007 wt.% C.

4.2 *Ex-situ* microstructural characterization

4.2.1 Scanning electron microscopy

Specimens for scanning electron microscopy (SEM) and electron backscatter diffraction (EBSD) observation were prepared by surface grinding using 400, 600, 800, and 1200 grit silicon carbide papers using water as a lubricant. The specimen surfaces were then mechanical polished using 6 μm and 1 μm diamond suspension followed by a finishing step using a 5:1 (by volume) mixture of 0.05 μm colloidal silica to 30 wt % hydrogen peroxide solution. To ensure the specimens were not heavily contaminated with colloidal sillica particles, the polishing cloth was flooded with water until it was clean and the samples were polished just with water to remove the colloidal sillica from the surface. After each grinding step the samples were rinsed under cool tap water for 30 seconds, and then immediately rinsed with denatured ethanol, and immediately dried with compressed air. Additionally, after the final colloidal sillica polishing step, the specimens were ultrasonicated in denatured ethanol for 30 minutes, before being dried using compressed cool air, and being stored under vacuum to prevent the formation of hydrides and oxides on the sample surface.

SEM observations were made using either a Hitatchi S-570 scanning electron microscope with a tungsten filament source and an applied voltage of 20 kV, or a Carl Zeiss NTS Ltd. Sigma scanning electron microscope with a field emission source and an applied voltage of 20 kV. Backscatter electron contrast, where phase contrast or orientation contrast in single-phased materials, was used to determine the microstructure. Phase contrast was thresholded to determine the fraction of α produced after each isothermal holding time, and the standard deviation of all measurements were used as error descriptors. Grain sizes were taken as the diameter of a circle of equal area (EQAD).

4.2.2 Electron backscatter diffraction

EBSD observations were made using a Carl Zeiss NTS Ltd. Sigma scanning electron microscope with a field emission source and an applied voltage of 20 kV and 60 μm aperture size. The EBSD patterns were collected with a Digiview detector and indexed using the EDAX TSL Orientation Imaging Microscopy (OIM) data collection software.

Using the EDAX TSL OIM Analysis 6 software, grains were defined as clusters of at least 5 points in size and grain boundaries were identified using a disorientation angle of 5° or greater. The

grain confidence index standardization method was employed to ensure indexed points with lower confidence indices that shared the same orientation as their surrounding grains were not excluded. Finally, an instance of grain dilation was performed and the resulting map was visually checked to ensure false grains were not created by the dilation step.

The area of each grain was extracted and the grain sizes were taken as the diameter of a circle of equal area (EQAD). The location of the prior β grain boundaries for the as-treated specimens were estimated using the 6 reduced axis-angle pairs method as described by Wang *et al.* [88]. This approach allows for the approximate reconstruction of the β grain structure from a fully α microstructure by identifying special grain boundary disorientations between α grains within a tolerance of ± 5 °. The grain boundaries that do not share special axis-angle relationships arising from the Burgers orientation relationship between the α-phase and β-phase are considered as prior β grain boundaries.

EBSD map files, containing, x, y coordinates, and the corresponding Euler angles describing the orientation of the given pixel, were acquired using the Carl Zeiss NTS Ltd. Sigma Scanning Electron Microscope with a Digiview detector, using EDAX TSL Orientation Imaging Microscopy (OIM) Data Collection software. The MTEX quantitative texture analysis tool was used to create a discretized OD with step size of 5^{o}. An OD was taken for each specimen, and used to predict velocity for a given texture following Sections 2.5.3 and 2.5.5 [80].

4.3 *In-situ* microstructural characterization

4.3.1 Laser ultrasonics

Heat treatments were conducted in a Gleeble 3500 thermomechanical direct resistance heating furnace (Dynamic System Inc. Poestenkill, NY) with a window transparent to the excitation laser and infrared laser wavelengths. A series of pumping steps involving a first stage of rough pumping using a mechanical pump and a later high vacuum stage involving a diffusion pump were employed to create a vacuum environment within the testing chamber of pressure at most 0.5 Pa. A low friction force jaw assembly was used ensuring the treatment was purely thermal. The specimens were secured on either end by two sets of water cooled copper grips. A current was applied to the grips and flowed through the specimen, resulting in resistive heating of the specimen. The

temperature of the specimen was measured and controlled with a pair of K-type thermocouple wires spot-welded at the mid-length of the specimen on the opposite side of the laser beams.

Laser ultrasonic measurements were conducted in the Gleeble 3500 thermomechanical simulator using a Laser Ultrasonics for Metallurgy (LUMet) sensor. The LUMet sensor is attached to the rear door of the Gleeble chamber. A frequency-doubled Q-switched Nd:YAG laser with a wavelength of 532 nm is used for the generation of a wide band compressive ultrasonic pulse. The duration of the laser pulse is approximately 6 ns, it has a maximum energy of 72 mJ and up to 50 pulses can be generated per second. The laser pulse produces a broadband ultrasonic pulse by vaporizing a small quantity of material at the surface (of the order of one micrometer per hundred laser pulses). The ultrasonic pulse propagates back and forth through the thickness of the specimen and its amplitude decreases by interacting with the material and its microstructure. Successive arrivals of the ultrasonic pulse at the generation surface are detected with a frequency-stabilized Nd:YAG pulsed laser which illuminates the surface with infrared radiation at a wavelength of 1064 μm and a pulse duration of 90 μs. The infrared detection laser that is reflected on the specimen surface is demodulated inside a photo-refractive crystal using an active interferometer approach [75]. After only a few oscillations of the ultrasonic pulse between the two parallel surfaces of the specimen, its intensity is only weakly diffused in other directions and the ultrasonic properties measured are representative of the average properties of the material over a volume created by the surface of the laser spot (about 2 mm) multiplied by the specimen thickness. Both generation and detection laser beams are co-linearly aligned at the center length of the specimen. The time required for the ultrasonic pulse to travel back and forth through the specimen thickness is calculated using a cross correlation algorithm applied on two echoes collected at the specimen surface. The velocity is then computed by the ratio of the propagation distance by the time between two echoes. Cross correlation and velocity calculation was conducted using the software package CTOME (Computational Tools for Metallurgy) [89] developed by Thomas Garcin at the University of British Columbia. Figure 4.1 shows a schematics illustration of the measurement configuration for the cp-Ti tests. The Ti-5553 specimens were oriented identically as shown in Figure 4.1, with the exception that the backscatter surfaces were taken by cutting down the TD plane at the center-line.

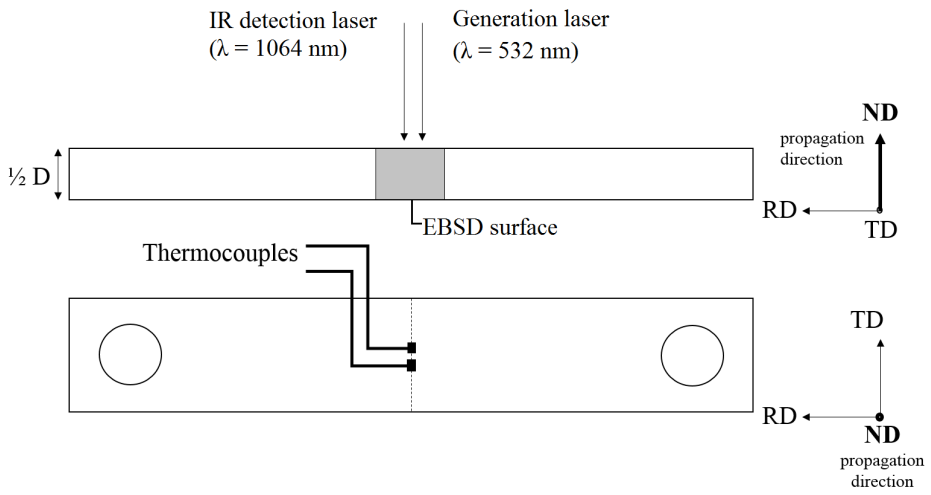

Figure 4.1: Schematic of cp-Ti specimen in the Gleeble with the normal direction (ND) aligned with the direction of wave propagation, the rolling direction (RD) aligned with the length of the specimen, the transverse direction (TD) aligned with the width of the specimen, and the EBSD image plane is shown in grey lying in the plane defined by the TD normal.

4.3.2 Thermal treatments

Continuous heat treatments to evaluate phase transformation kinetics in cp-Ti

Continuous heating and cooling cycles were conducted at a rate of 3 °C.s^{-1}. Three conditions were selected for monitoring the α/β transformation. As will be shown below, these cyclic thermal treatments led to three distinct microstructures and textures allowing the technique to be evaluated for different conditions. In the first set of tests the as-received material was continuously heated to 1000 °C followed by cooling to room temperature where the microstructure was observed. In a second set of tests, specimens were heated to 1000 °C followed by cooling to room temperature. This same specimen was then subjected to the same cycle, the transformation kinetics being monitored in the 2nd heating/cooling cycle and the microstructure observed after the 1st cycle. In the final set of experiments, specimens were cycled 4 times between room temperature and 950 °C. On the 5th cycle the transformation kinetics were monitored, the microstructure being observed following the final cooling. In the third set of experiments it was decided to limit the upper temperature to 950 °C so as to avoid excessive grain growth. The first two sets of tests were conducted to 1000 °C so as to allow for the ultrasonic velocity to be monitored over as large a range of temperatures in the β-phase as possible. If a specimen was to endure repeated cycling, between each cycle, it would

be polished gently to remove any oxides that would prevent attachment of thermocouples or cause scattering of the infrared laser. The cycling treatment profiles are shown in Figure 4.2.

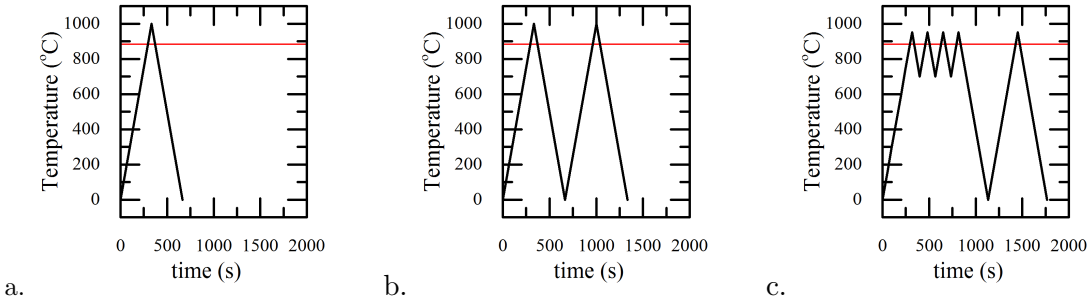

Figure 4.2: Heat treatment profiles for specimens enduring a) 1 cycle of treatment, b) 2 cycles of treatment, and c) 5 cycles of treatment where the red line indicates the equilibrium transformation temperature of 882 °C.

Isothermal heat treatments to evaluate precipitation kinetics in Ti-5553

Specimens were heated to 900 °C and held for 15 minutes to fully dissolve the α phase. Specimens were then cooled at 6.7 °C.s^{-1} to 700 °C. Specimens were held at 700 °C for times of: 5, 10, 33, 53, 75, and 180 minutes before being quenched with helium gas to room temperature. A control specimen, after being cooled at 6.7 °C.s^{-1} to 700 °C was quenched immediately to determine the full β microstrucuture at the onset of the isotherm. Laser ultrasonic measurements were taken during the isothermal segments of each specimen's treatment to monitor the α phase precipitation and *ex-situ* metallographic evaluation was conducted after each quench.

4.3.3 Interpretation of waveform data in CTOME

The velocity is then computed by the ratio of the propagation distance by the time between two echoes. Cross correlation and velocity calculation was conducted using the software package CTOME [89]. Within the CTOME software, velocity was calculated using the single echo technique (SE2), where the software calculates the cross correlation function between the second echo of each waveform and the second echo of a waveform in a reference file. Using this technique, the velocity is calculated using the equation:

$$v = \frac{z}{t_R + \Delta t} = \frac{2ne}{t_R + \Delta t} \tag{4.1}$$

Where z is the propagation distance, t_R is arrival time of the reference echo, e is the sample thickness, Δt is the delay time calculated from cross-correlating the observed echo with the reference echo, and n is the echo number. The arrival time of the reference echo, t_R, is measured by locating the time at the local minimum for the reference echo. The time of travel (τ) of the considered echo, is then $t_R + \Delta t$.

Processing of cp-Ti velocity data

Each data file was compared using the second echo as a reference echo with the SE2 algorithm in CTOME. The reference file (reference C) was taken in the as-received state, under vacuum, at room temperature, and was kept constant for each data set. The reference waveform used in the analysis was the 20^{th}, as it was representative and of sufficient quality. The window size was set to be 0.35 μs, the maximum frequency was set to 15 MHz, and the window was centered on the minimum of each waveform.

Processing of Ti-5553 velocity data

Each data file was compared using the second echo as a reference echo with the SE2 algorithm in CTOME. The reference file (reference A) was taken in the as-received state, under vacuum, at room temperature, and was kept constant for each data set. The reference waveform used in the analysis was the 20^{th}, as it was representative and of sufficient quality. The window size was set to be 0.35 μs, the maximum frequency was set to 15 MHz, and the window was centered on the minimum of each waveform.

4.3.4 Interpretation of error in laser ultrasound measurements

There are two important error descriptors in velocity, including, the absolute error in velocity and the precision (relative error in velocity) of the velocity measurements.

Velocity is typically measured with an accuracy (absolute error) equal to the accuracy of the

thickness measurement, i.e. of about 1 %. Velocity is defined as distance traveled (2ne) where e is the thickness of the piece and n is the echo number, divided by time of travel (τ). The error can be calculated by summation in quadrature since the two quantities are independent. Application of the logarithm to both sides of the equation before differentiation and addition in quadrature yields:

$$v = \frac{2ne}{\tau} \tag{4.2}$$

$$\ln(v) = \ln(2n) + \ln(e) - \ln(\tau) \tag{4.3}$$

$$\left(\frac{\delta v}{v}\right)^2 = 0 + \left(\frac{\delta e}{e}\right)^2 + \left(\frac{\delta \tau}{\tau}\right)^2 \tag{4.4}$$

$$\delta v = v\left(\left(\frac{\delta e}{e}\right)^2 + \left(\frac{\delta \tau}{\tau}\right)^2\right)^{0.5} \tag{4.5}$$

Where δe is the error in thickness due to the caliper reading, and is equal to 0.01 mm, and $\delta\tau$ is an estimate of the error in the measurement of the delay that is obtained from the normal regression (Gaussian fit) applied to the cross-correlation function for the localization of the local maximum in CTOME [89]. The software Gnuplot [90] estimates a standard deviation for each fitting parameters from the variance-covariance matrix. In this study, the standard deviation for the value of delay is of the order of 1%. For time delays in titanium of approximately 0.98 μs, the error is given as ± 0.009 μs.

With this, relative error is given as:

$$\frac{\delta v}{v} = \left(\left(\frac{\delta e}{e}\right)^2 + \left(\frac{\delta \tau}{\tau}\right)^2\right)^{0.5} \tag{4.6}$$

$$\frac{\delta v}{v} = \left(\left(\frac{0.01\text{mm}}{3\text{mm}}\right)^2 + \left(\frac{0.009\mu\text{s}}{0.98\mu\text{s}}\right)^2\right)^{0.5} \tag{4.7}$$

$$\frac{\delta v}{v} = 0.97\% \tag{4.8}$$

This absolute error of approximately 1 % is used to compare velocity profiles of different treatments to one another.

The precision (repeatability) of the measurement was taken by capturing multiple velocity

measurements at the same location on a titanium sample, held at room temperature. The standard deviation of the velocity measurements corresponded to 0.01 % which was used to describe the relative error in velocity, when comparing points on the same velocity profile.

Chapter 5

Finite Element Modeling of Ultrasonic Wave Propagation in Dual Phase Material

5.1 Introduction

The purpose of this section is to describe the results of a finite element (FE) simulation of ultrasound propagation in a two dimensional specimen containing two isotropic phases, and perform a sensitivity analysis on six possible averaging schemes that could be used to calculate velocity in the aggregate. In particular, this modeling approach intended to evaluate the proper way to predict the average ultrasonic velocity, as measured in an experiment, from the velocities of the individual phases. The effect of phase fraction, and particle geometry was explored.

5.2 Input parameters, construction and assumptions

Explicit, 2-D finite element modelling (FEM) simulations were performed in Abaqus CAE version 6.13. Each phase was assumed to be elastically isotropic, and defined by its respective density, Young's modulus, and Poisson ratio (Table 5.1), where values were decided to be representative of α and β titanium.

Table 5.1: Input parameters defining two isotropic phases used in an explicit 2-D FEM simulation of an ultrasound pulse propagating in a dual phased polycrystalline aggregate structure

Phase (α/β)	Density (ρ) ($kg.m^{-3}$)	Young Modulus (E) (GPa)	Poisson Ratio (υ)
α	4502	120	0.3
β	4382	70	0.3

The 2-D meshed specimen had a thickness of 2 mm, a length of 10 mm, and a mesh size of 4 μm in the small meshed region (4 mm by 2 mm) located in the center of the specimen. In order to fix the sample geometry in space during the pulse propagation, additional boundary conditions are defined for the elements of the mesh located along the left and right vertical edges of the geometry such that no rotation and translation are permitted, i.e. $U_1 = U_2 = U_3 = U_{R1} = U_{R2} = U_{R3} = 0$ (Abaqus Boundary Condition: Mechanical-Encastre).

The mesh size in the simulation region is adjusted to ensure that the smallest longitudinal wavelength present in the system during the simulation is described by at least 10 elements of the mesh. An estimate of the smallest wavelength is obtained by the ratio of the longitudinal velocity ($C_d \simeq 5000$ m.s^{-1}) by the maximum frequency of vibration ($f_{max} \simeq 100$ MHz) [91]. The mesh size must therefore be smaller than $Cd/(f_{max}*10) = 5000/(100*10) = 5$ μm. The element size (L_e) is then set to 4 μm for the set of simulations presented in this chapter.

The elements in the small meshed region were defined as four-node bi-linear quadrilateral plane strain (CPE4R) elements, meaning that per element there are four straight element sides with 4 nodes, where one node is located at each corner. Conversely, the larger mesh structure outside the small meshed region served the purpose of dissipating transverse components of the wavefront, so only the longitudinal component that returned to the monitoring region would be accounted for within the simulation time.

The time increment for the simulation is calculated by ensuring that at least 4 time steps are required for a longitudinal wave to propagate a distance of one mesh, i.e. $\Delta t = 1/4\ (L_e/C_d) = 1/4*(4/5) = 0.2$ ns [91].

Scripts to assign the material properties of the elements were generated in MATLAB version 2013a. As shown in Figure 5.1, three different geometric arrangements of the two phases were

considered. The plate structures, shown in Figure 5.1b and Figure 5.1c were created with 50 % of the elements being β phase elements. The motivation behind the creation of the horizontal and vertical plate geometries was to compare the simulated results to theoretically determined ultrasonic velocities under series and parallel assumptions, respectively. The dispersed element structure shown in Figure 5.1d was modeled at various phase fractions of β phase, ranging from 0 % to 100 %. Table 5.2 summarizes the relative phase fraction and seeded microstructure imposed unto the small meshed region of the FEM specimen for each trial.

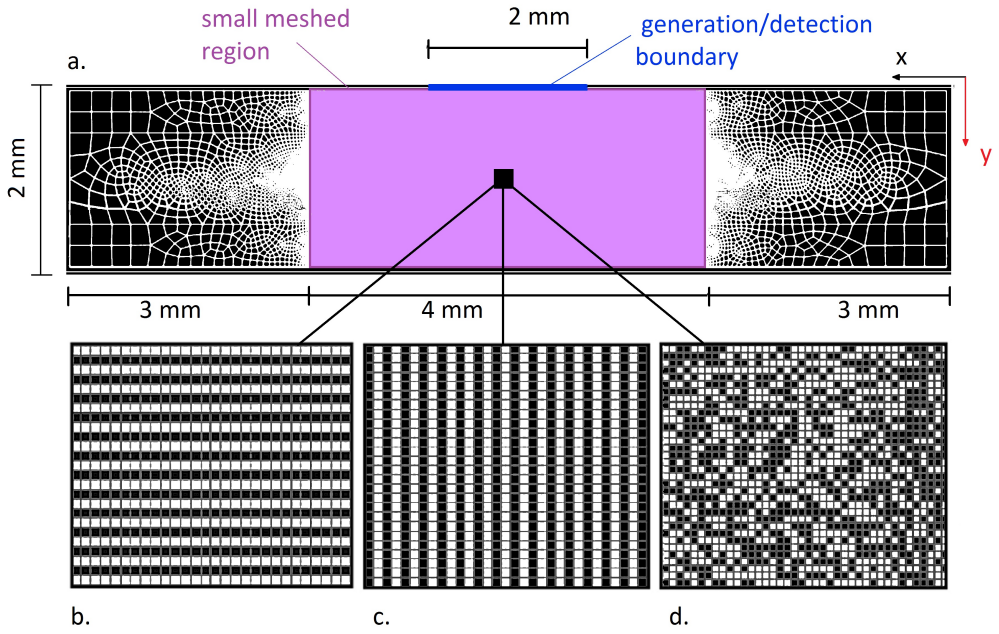

Figure 5.1: (a). 2D generated mesh part with thickness of 2 mm, length of 10 mm and mesh size of 4 μm in the small mesh region (4 mm x 2 mm), (b). horizontal plates, (c). vertical plates and (d). randomly dispersed elements. Vertical displacement (u_y) is measured as the direct output of the simulation from nodes in the generation/detection line (blue), and the vertical displacement direction is indicated by the red arrow.

Table 5.2: Summary of imposed microstructures seeded to the core interaction region of the meshed specimen

Trial	f_α (%)	f_β (%)	Imposed microstructure
1	0	100	dispersed
2	10	90	dispersed
3	30	70	dispersed
4	50	50	dispersed
5	70	30	dispersed
6	80	20	dispersed
7	90	10	dispersed
8	100	0	dispersed
9	50	50	horizontal plates
10	50	50	vertical plates

5.2.1 Wavelet generation

An initial displacement was applied to a region 2 mm in size located at the center of the top boundary of the meshed part (cf. Figure 5.1). The displacement is applied in the form of a Ricker wavelet (frequency = 10 MHz) because it provided a means to center the frequency range within the experimental frequency range of LUMet (5 - 20 MHz). The amplitude of a Ricker wavelet is given by [92, 93]:

$$A_o = 1.1\left(1 - 2\pi^2 f^2\left(\frac{t-b}{c}\right)^2\right) e^{-\pi^2 f^2\left(\frac{t-b}{c}\right)^2} \tag{5.1}$$

Where b is 125 ns, and serves to center the Ricker peak at 125 ns, and d is 1.1 and applied for scaling the amplitude, f is the frequency (Hz), t is time (s), and A is the displacement amplitude. The absolute amplitude selected for convenience has little effect in the model as the medium was considered with no elastic limit, and the amplitude of the pulse does not effect the measured response (velocity). The reader is referred to the work of Murray and Wagner [94] for a more in depth analysis on modeling displacement amplitudes in the ablative regime. Constants b and c are

implemented to scale the Ricker pulse to better match experimental observations from the LUMet measurement. The Ricker pulse generated over a span of 250 ns is displayed in Figure 5.2a. As the ultrasonic wave is characterized by setting the frequency to 10 MHz and setting the material properties of the system which define a velocity range of [4600, 6000] $m.s^{-1}$ (calculated from the 100 % β and α conditions shown in Table 5.1), the range of wavelengths for the ultrasound pulse used in each trial spans from 0.46 mm to 0.6 mm. The wavelength constitutes approximately a third of the specimen's thickness (2 mm). In order to prevent a discontinuity between the nodes in the generation region and the adjacent nodes, a normalized Gaussian function (Figure 5.2b) symmetric about the centerline, defines the amplitude of the Ricker wavelet spatially along the generation line (2 mm) as:

$$A = A_o * e^{\left(\frac{x^2}{2(0.5)^2}\right)} \tag{5.2}$$

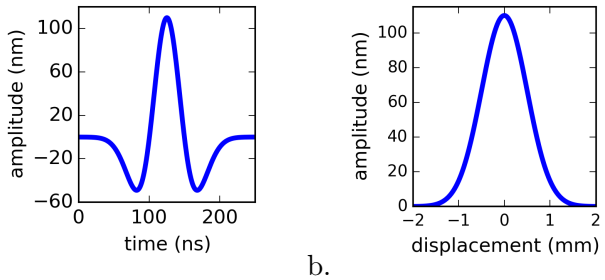

a. b.

Figure 5.2: a). Time dependence of the Ricker pulse amplitude and b). an example of the Gaussian scaling used to normalize the applied amplitude (at t = 125 s) across the generation boundary, where the peak of the Gaussian is centered on the mid line of the specimen

5.3 Interpretation of FEM data

Along the boundary length where generation occurred, vertical displacement data was extracted from the nodes at the excitation area and averaged at each time step (8 ns) for a total time of 2000 ns. The excitation area corresponds to along the 2 mm highlighted in blue in Figure 5.1. This length of 2 mm was selected because it is consistent with the diameter of the laser spot used in LUMet. When the averaged displacement data (u_y) is plotted against time, the simulated waveform

is visible. An example of such a waveform is shown in Figure 5.3.

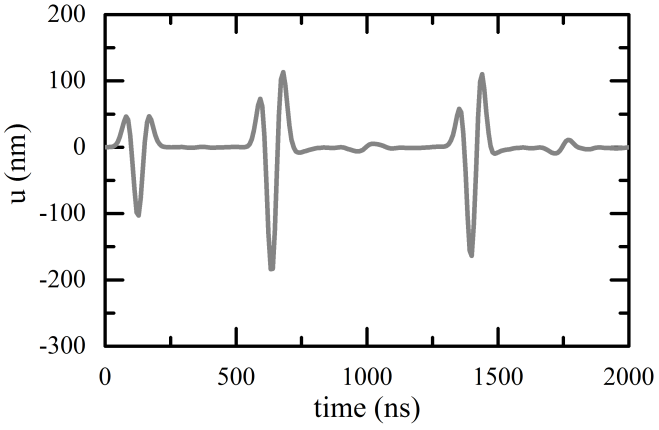

Figure 5.3: Example of averaged displacement over time data taken from upper boundary nodes responsible for generation and detection of the Ricker's ultrasonic pulse

From the above waveform, it is then possible to calculate the average velocity of the ultrasonic pulse. This average velocity is calculated as twice the thickness of the specimen($2 * 2$ mm $= 4$ mm) divided by the time it takes for the pulse to travel through the specimen and back to the monitored surface (t_{delay}). The t_{delay} is found by calculating the maximum amplitude of the cross correlation between the first and second echo shown in Figure 5.3. Cross correlation was calculated as:

$$A_{x-corr} = \text{IFFT}\left(\text{FFT}\,(f) * \overline{\text{FFT}}\,(g)\right) \tag{5.3}$$

Where FFT is the fast fourier transform of the echos, IFFT is the inverse fourier transform of the echos, and the overbar indicates the complex conjugate.

The amplitude of the cross correlation function and respective time delay was calculated using the software package CTOME, where a sample output of the cross correlation function for a given waveform is provided in Figure 5.4. The maximum of the cross correlation amplitude signifies the time delay. The two echo technique (TE1) was used to cross-correlate the first echo to the second echo in the same waveform to find time delay in the FEM study.

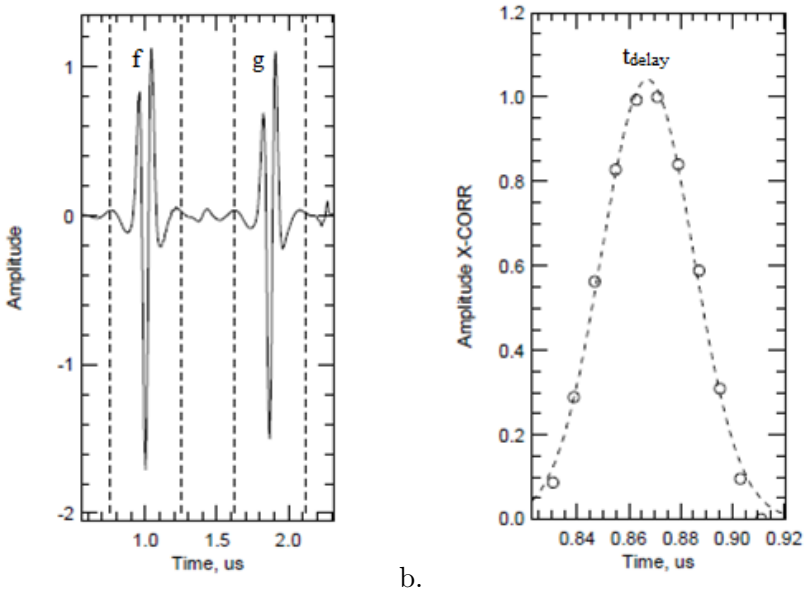

a. b.

Figure 5.4: Example of a) two waveform echos (f and g), and, b) the corresponding amplitude of cross correlation function

5.4 Calculation of average velocities

One intention of these simulations was to compare the FEM computed average velocity to ways one could compute the average velocity based on the moduli and the densities of the two phases (cf. Equations 5.4, 5.5, 5.6, 5.9, 5.10, 5.11). First the prediction based on approximating the inhomogeneous material as a homogeneous material using either the upper bound averaged elastic modulus to calculate velocity (v_1) or the lower bound averaged elastic modulus to calculate velocity (v_2), and the arithmetic average (v_3) was tested and are given as:

$$v_1 = \left(\frac{1}{\rho} \frac{(1-\upsilon)}{(1+\upsilon)(1-2\upsilon)} \left(f_\alpha E_\alpha + f_\beta E_\beta \right) \right)^{1/2} \tag{5.4}$$

$$v_2 = \left(\frac{1}{\rho} \frac{(1-\upsilon)}{(1+\upsilon)(1-2\upsilon)} \frac{E_\alpha E_\beta}{f_\beta E_\alpha + f_\alpha E_\beta} \right)^{1/2} \tag{5.5}$$

$$v_3 = \left(\frac{1}{\rho} \frac{(1-\upsilon)}{(1+\upsilon)(1-2\upsilon)} \frac{1}{2} \left(\left(f_\alpha E_\alpha + f_\beta E_\beta \right) + \frac{E_\alpha E_\beta}{f_\beta E_\alpha + f_\alpha E_\beta} \right) \right)^{1/2} \tag{5.6}$$

Where the density (ρ) calculated at a given phase fraction is given using the rule of mixtures:

$$\rho = f_\alpha \rho_\alpha + f_\beta \rho_\beta \tag{5.7}$$

And the P-wave modulus had been expressed in terms of the Young modulus (E) and Poisson ratio (υ):

$$\lambda = \frac{(1-\upsilon)}{(1+\upsilon)(1-2\upsilon)} E \tag{5.8}$$

Alternatively, the predicted velocities obtained by assuming that the wave spends equal time in the two phases (v_4) or that the wave causes equal displacement in the two phases (v_5) were tested, and an arithmetic average of the two were taken (v_6).

$$v_4 = f_\alpha v_\alpha + f_\beta v_\beta \tag{5.9}$$

$$v_5 = \left(\frac{f_\alpha}{v_\alpha} + \frac{f_\beta}{v_\beta} \right)^{-1} \tag{5.10}$$

$$v_6 = \frac{1}{2} \left(\left(f_\alpha v_\alpha + f_\beta v_\beta \right) + \left(\frac{f_\alpha}{v_\alpha} + \frac{f_\beta}{v_\beta} \right)^{-1} \right) \tag{5.11}$$

Where v_α and v_β are the velocities observed in the individual α and β phases, respectively:

$$v_\alpha = \left(\frac{(1-\upsilon)}{(1+\upsilon)(1-2\upsilon)} \frac{E_\alpha}{\rho_\alpha} \right)^{1/2} \tag{5.12}$$

$$v_\beta = \left(\frac{(1-\upsilon)}{(1+\upsilon)(1-2\upsilon)} \frac{E_\beta}{\rho_\beta} \right)^{1/2} \tag{5.13}$$

5.5 FEM results

In the literature [69], it has been argued that the averaging scheme is not very important when the difference in properties (density and elastic moduli) are small. This idea can be demonstrated by using titanium as an example, which is the intention of the following section.

The FEM simulated velocity (corresponding to trial 1 - 8 of Table 5.2) demonstrated an increase in average velocities as additions of α phase particles were randomly added to the β matrix. Figure 5.5 compares the FEM simulated velocities for dispersed, horizontal plate, and vertical plate arrangements of the two phases. Also shown are the predicted velocities according to the averaging schemes listed in Equations 5.4, 5.5, 5.6, 5.9, 5.10, and 5.11.

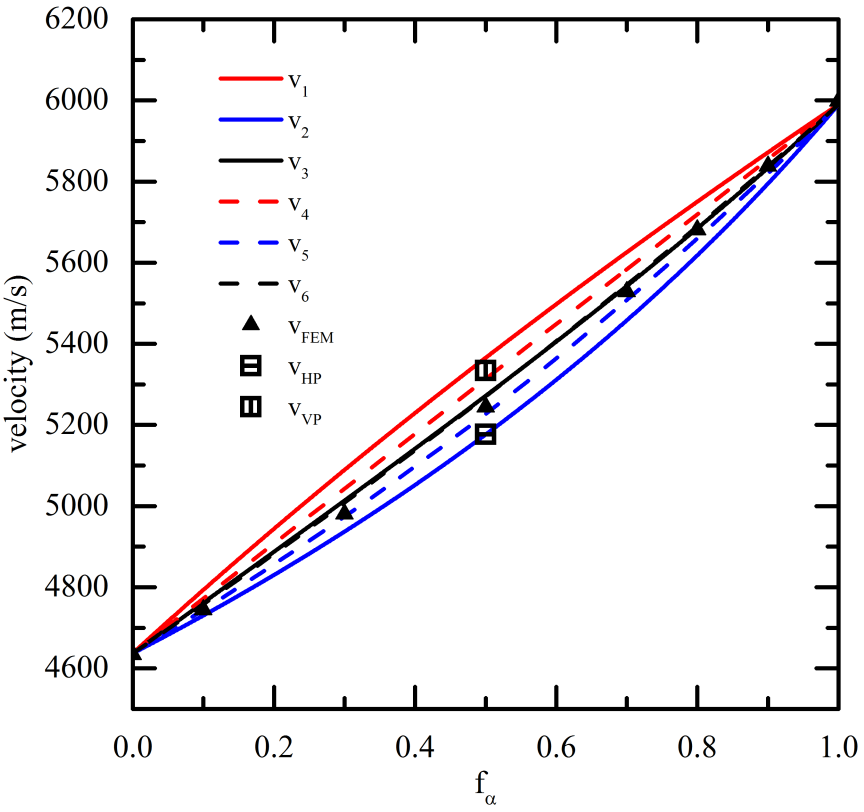

Figure 5.5: Ultrasonic velocity computed by the six potential averaging schemes listed in Equations 5.4, 5.5, 5.6, 5.9, 5.10, 5.11, as well as FEM simulation results, where v_{HP}, v_{VP}, and v_{FEM} refer to simulation trial 9 (horizontal plate), trial 10 (vertical plate) and trials 1 - 8 (dispersed), respectively, as defined in Table 5.2.)

It is important to note that predictions from v_3 and v_6 overlap such that only v_3 is visible.

It appears that the FEM simulation containing the horizontal plated microstructure (trial 9 of Table 5.2) is in complete agreement with the value calculated at $f_\alpha = 50$ % when using the harmonic averaging approach on the Young's modulus (v_2, Equation 5.5). When transverse loading

is assumed and velocity averaged by Equation 5.10, the velocity (v_5) lay between the FEM velocities (Trials 1 - 8, Table 5.2) and the velocity obtained using v_2. Conversely, the v_{VP} value obtained by the FEM simulation containing the vertical plated core interaction region (trial 10 in Table 5.2) lay in between the v_1 and the rule of mixtures applied to velocity (v_4).

One can see that averaging based on the elastic moduli and wave velocities gives distinctly different results in the case of the upper (v_1 and v_4) and lower (v_2 and v_5) bound predictions.

First, upon examining the FE simulated lower bound containing horizontal plates, it was observed that the simulated velocity (v_{HP}) coincided perfectly with v_2. To understand why v_{HP} is consistent with v_2 instead of v_5, it is important to consider the relative size of the wavelength of the applied wavelet, which is between 0.45 and 0.6 mm, compared to the size of the microstructural features (plates of alternating phases), which are 4 μm in size.

When the wavelength of the applied wave is approximately the same size or smaller than the width of each microstructural feature (Figure 5.6a), it is possible to solve for the aggregate velocity in the following way:

$$v = \frac{d}{t} \tag{5.14}$$

$$v = \frac{L_\alpha + L_\beta}{t} \tag{5.15}$$

Where $t = t_\alpha + t_\beta$ which corresponds to time, t_α and t_β are time spent in the α and β phases, respectively, d is the distance traveled, and L_α and L_β are the widths of the α and β plates, respectively (as shown in Figure 5.6).

Substituting for t_α and t_β using Equation 5.14:

$$t = \frac{L_\alpha}{v_\alpha} + \frac{L_\beta}{v_\beta} \tag{5.16}$$

And substituting Equation 5.16 into Equation 5.15 yields:

$$v = \frac{L_\alpha + L_\beta}{\frac{L_\alpha}{v_\alpha} + \frac{L_\beta}{v_\beta}} = \left(\frac{\frac{L_\alpha}{v_\alpha} + \frac{L_\beta}{v_\beta}}{L_\alpha + L_\beta} \right)^{-1} \tag{5.17}$$

Where $L_\alpha + L_\beta = L_{total}$, and therefore:

$$v = \left(\frac{L_\alpha}{L_{total}} \left(\frac{1}{v_\alpha} \right) + \frac{L_\beta}{L_{total}} \left(\frac{1}{v_\beta} \right) \right)^{-1} \tag{5.18}$$

$$v = \left(\frac{f_\alpha}{v_\alpha} + \frac{f_\beta}{v_\beta} \right)^{-1} = v_5 \tag{5.19}$$

Conversely, if the wavelength of the applied wavelet is larger than the distinct microstructural features (Figure 5.6b), as observed in the FE simulation, then the above formulation is no longer valid. The waveform no longer lies in one feature at a distinct unit in time but contacts many features simultaneously. Instead of imagining the wave propagating through the aggregate feature by feature (step by step), it is now more accurate to imagine the waveform moving through one continuous medium where the medium's properties are defined as an average of the properties in each phase. For the horizontally plated microstructure, this average is calculated in series using the harmonic averaging approach on the Young modulus (v_2). The fact that v_2 matches v_{HP} is due to the relatively large wavelength of the Ricker pulse when compared to the horizontal plate thickness. Thus, the formulation described above in Equations 5.14 through 5.19 is only appropriate for coarser microstructures.

However, comparison of the upper bounds (v_1 and v_4) to the FE simulated velocity in a vertical plated microstructure (v_{VP}), shows that $v_4 \leq v_{vp} \leq v_1$. Even when the wavelength of the applied Ricker pulse is less than the size of the width of the vertical plates (Figure 5.6c), the wavefront cannot separate and thus will spend equal time in each phase (each plate) while propagating in this configuration. The wavefront must remain intact and can only travel at one velocity, and therefore it is not expected to produce a direct match to v_5. It is interesting to see that v_1 also did not match the simulated velocity, demonstrating that even with a larger wavelength (Figure 5.6d), since distinct segments of the wavefront will touch distinct features, the complex interactions involved to ensure the wavefront remains intact still have an effect.

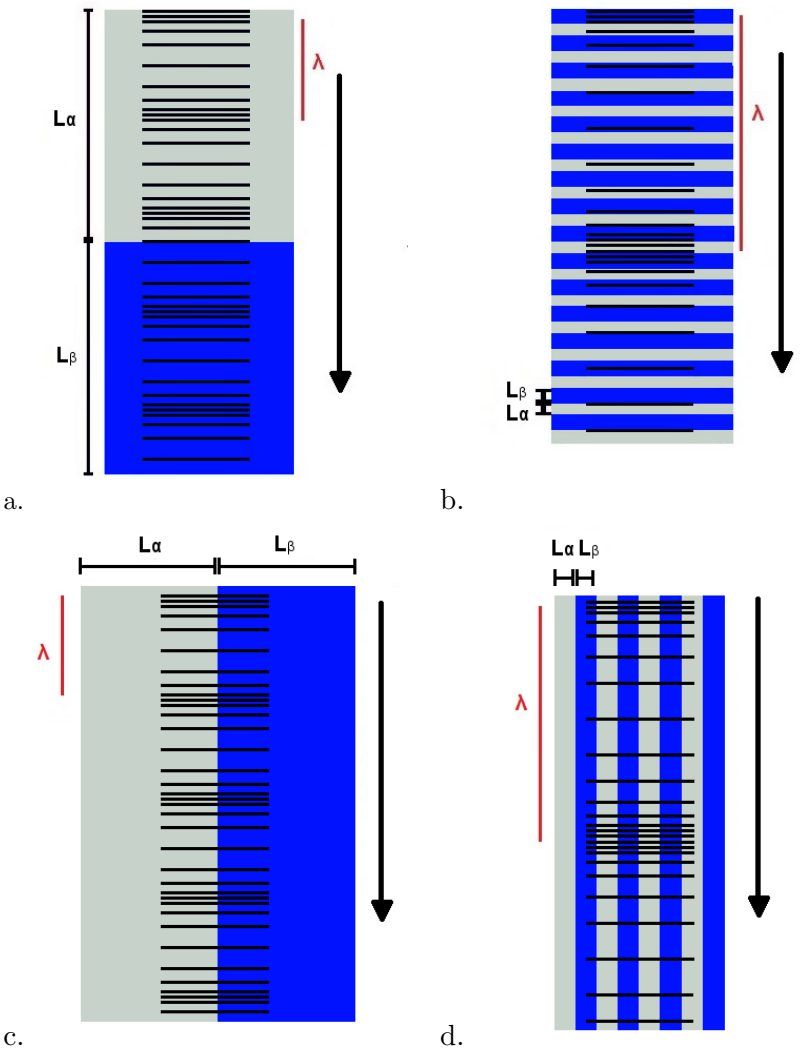

Figure 5.6: Schematic showing imposed Ricker wavelet a) propagating in horizontal plates where the wavelength is relatively larger than microstructural features, b) propagating in horizontal plates where the wavelength is smaller than microstructural features, c) propagating in vertical plates where the wavelength is relatively larger than microstructural features, d) propagating in vertical plates where the wavelength is smaller than microstructural features. The black lines indicates atoms in the wave, where lines appearing close together show compression of the wave, and lines spread apart indicate refraction. Wavelength is the distance between instances of maximum compression.

Finally, the FE simulated results for wave propagation in a dispersed microstructure (v_{FEM}), appeared to fall between v_3, v_6 and v_5, where v_3 and v_6 are nearly identical. Given that the velocity in a randomly dispersed mixture is often approximated as the average of the upper and lower bounds, which when computed using FE simulations were v_{VP} and v_{HP}, and where v_{VP} was lower than v_1, it appears intuitive that v_{FEM} is slightly lower than the arithmetic averages v_3 and

v_6.

5.6 Sensitivity of averaging schemes

In the literature [69], it has been arugued that the averaging scheme is not very important when the difference in properties (density and moduli) are small. This is demonstrated using titanium as an example in the following section by evaluating the sensitivity of averaging schemes v_1 - v_6 to changes in the P-wave modulus (λ) which under a polycrystalline and isotropic assumption is given by Equation 5.8.

The relevant polycrystalline material properties in pure titanium are calculated at the transformation temperature of 882 °C and are provided in Table 5.3.

Table 5.3: Density (ρ) and P-wave moduli (λ) of polycrystalline α and β titanium at 882 °C

Phase (α/β)	Density (ρ) ($g.m^{-3}$)	P-wave Modulus (λ) (GPa)	Reference
α	4417.19	123.72	[25, 36]
β	4409.34	115.3	[25, 38]

This corresponds to a state where the elastic modulus of the β phase is 93 % of the elastic modulus of the α phase ($\lambda_\beta/\lambda_\alpha$ = 93 %), and the density of the β phase is 99.8 % of the density of the α phase (ρ_β/ρ_α = 99.8 %). If λ_α is fixed to its polycrystalline value of 123.72 GPa, and λ_β is variable, the sensitivity of each averaging scheme presented in Equations 5.4, 5.5, 5.6, 5.9, 5.10, and 5.11 can be computed for given phase fractions. Figure 5.7 shows the sensitivity of averaging schemes v_1 - v_6 for β phase fractions of a. $f_\beta = 0.1$, b. $f_\beta = 0.5$, and c. $f_\beta = 0.9$. Regardless of phase fraction, it can be observed that in instances where the material properties (λ, ρ) are similar, the selection of an averaging scheme has little effects on the resulting computed velocity.

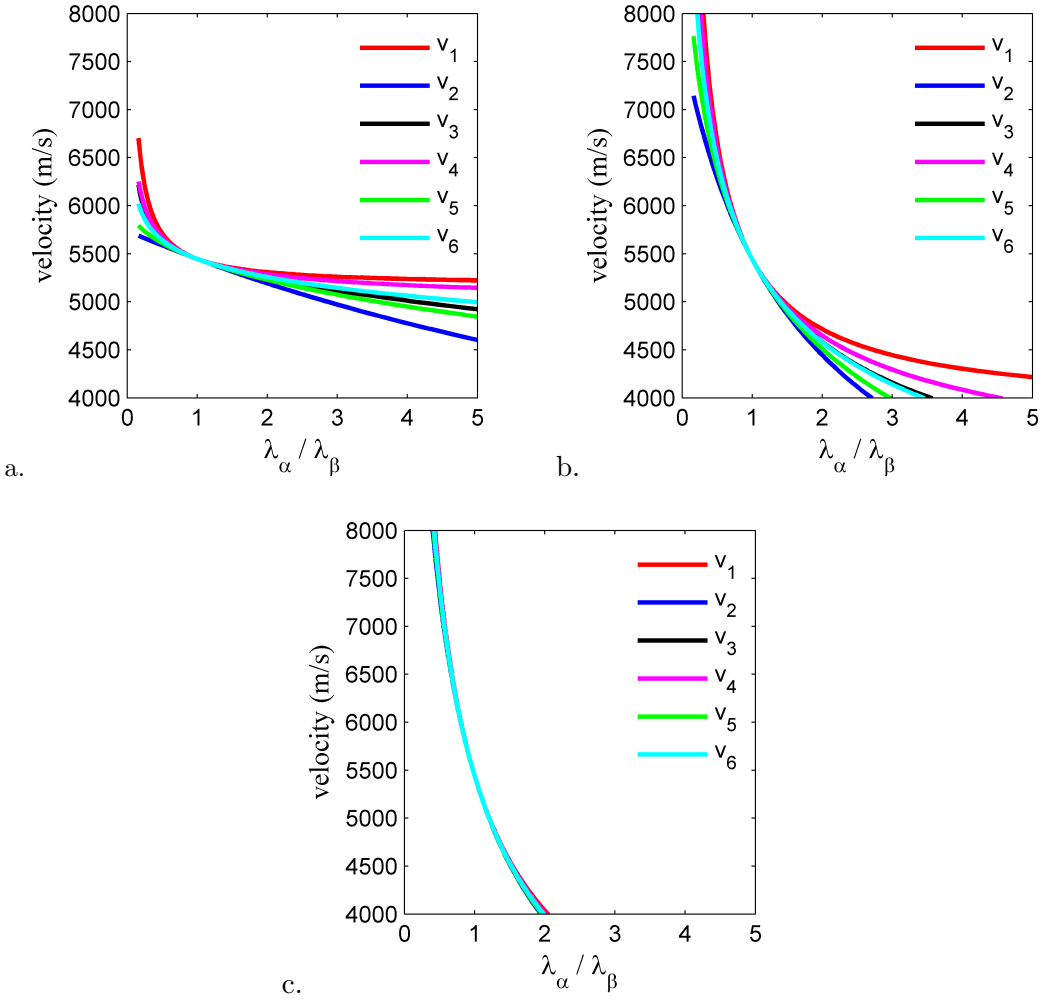

Figure 5.7: Velocity plotted against a changing ratio of P-wave modulus (ρ_α/ρ_β), where λ_α was fixed at 123.72 GPa, and λ_β is variable for a given phase fraction of β a) $f_\beta = 0.1$, b) $f_\beta = 0.5$, and c) $f_\beta = 0.9$

Given the similarity in elastic moduli of α phase and β phase titanium, a rule of mixtures on velocity (Equation 5.9) will suffice when modeling the effects of phase change. The application of a rule of mixtures has been used before in laser ultrasonic evaluation of phase transformations in steels by Kruger and Damm [69].

5.7 Chapter summary

This chapter examined the propagation of an ultrasonic pulse in different geometric arrangements of two phase mixtures using a 2-D, explicit finite element model. The selection of a correct averaging

scheme to predict velocity was found to not only depend on the geometric configuration of the two phases but also the relative size of the wavelength compared to the width of the microstructural features. When the FE simulation ran on a series of horizontal plates, the resulting velocity was predicted by taking the lower bound average of the Young modulus (v_2), due to the relatively large wavelength of the pulse compared to the plate thickness. Conversely, when vertical plates were used in the simulation, neither averaging assumptions (v_1 and v_4) were able to predict the resulting velocity exactly, demonstrating that interactions are at work to ensure the wavefront remains in tact. Finally, in the context of titanium, predicting velocity via a rule of mixtures over velocity is sufficient given the similarities in the bulk P-wave moduli and densities of the two phases.

Chapter 6

In-situ Laser Ultrasonic Measurement of the HCP to BCC Transformation in Commercially Pure Titanium

6.1 Introduction

Here, laser ultrasonic measurements are presented for the continuous heating and cooling of a commercially pure titanium plate with the goal being to provide a quantitative assessment of the transformation kinetics. By performing experiments that thermally cycled through the β transus, the kinetics of the α to β and β to α-phase transformations could be assessed. Quantitative *ex-situ* metallography and EBSD have also been used to evaluate grain size and texture of the α-phase *post mortem*. The purpose of examining specimens after different numbers of thermal treatment cycles through the β transus was to illustrate the importance of grain size (particularly in the β-phase) and crystallographic texture on phase fraction. From this, a systematic method is presented for analyzing the ultrasonic velocity to obtain the fraction of α-phase and β-phase accounting for the effects of material property and texture changes on phase transition.

6.2 Characterization of the as-received material

The as-received microstructure of the commercially pure titanium specimens (composition dictated in Section 4.1) was composed of polygonal α grains with a mean equivalent area diameter (EQAD) of 42 μm as determined by electron backscatter diffraction (EBSD). The as-received microstructure is shown in Figure 6.1.

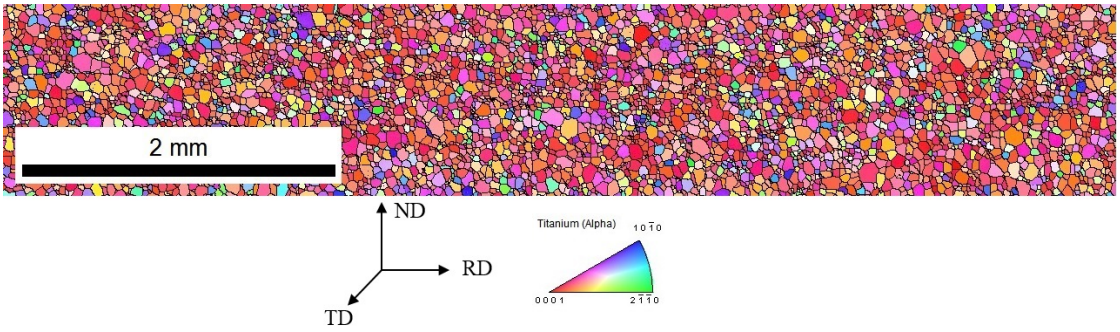

Figure 6.1: Normal direction (ND) EBSD IPF map showing equiaxed and recrystallized grains in the as-received plate

6.3 *Ex-situ* observation of microstructural changes upon thermal cycling

Figure 6.2 shows examples of backscatter electron (BSE) images with orientation contrast for the specimens in the a) as-received state (AR), b) after 1 treatment cycle (1-cycle), and c) after 5 treatment cycles (5-cycles) of heat treatment. It can be observed that the as-treated structures contain arrangements of α packets containing substructures of plates aligned in parallel, growing out from prior β grain boundaries. Figure 6.2d and 6.2e show low magnification BSE images of the plated structure after 1 treatment cycle (1-cycle), and after 5 treatment cycles (5-cycles) of heat treatment, respectively.

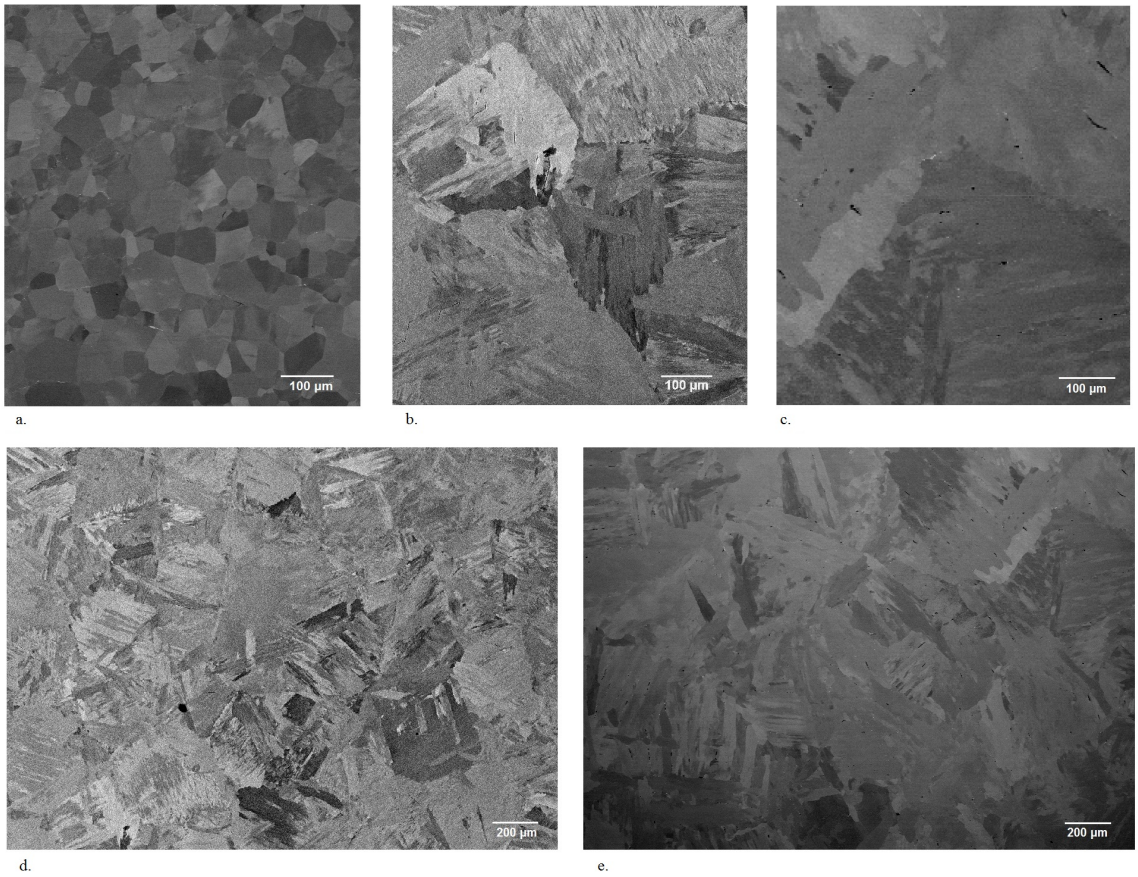

Figure 6.2: Backscatter electron (BSE) images with detailed orientation contrast for the specimens in the a) as-received state (AR), b) after 1 treatment cycle (1-cycle), c) after 5 treatment cycles (5-cycles) of heat treatment, and low magnification BSE images showing typical microstructures d) after 1 treatment cycle (1-cycle), and e) after 5 treatment cycles (5-cycles) of heat treatment

Figure 6.3 shows representative portions of inverse pole figure maps measured for the specimens in the a) as-received state (AR), b) after 1 treatment cycle (1-cycle), and c) after 5 treatment cycles (5-cycles) of heat treatment. In each case the observations were made on the plane normal to the TD direction at the center of the specimen. Moreover, the location of observation was selected to coincide with the region sampled by the ultrasonic pulse. Measurements were made in only one two-dimensional plane. All the EBSD maps were $\geq$ 1.5 x 1.5 mm in the plane of wave propagation (cf. Figure 4.1). This includes a large fraction of the grains that interacts with the ultrasonic pulse. This is important so as to have the local texture for velocity prediction.

As can be seen in Figure 6.3a, the as-received state is composed of polygonal grains, whose size is relatively homogeneous. In contrast, the microstructure of the specimens subjected to 1

and 5 treatment cycles (Figure 6.3b and 6.3c) are composed of coarse grains with irregular grain boundaries resulting from the cycling between the α and β-phases. The plate-like substructure of each grain in the as-treated conditions, which was visible under BSE orientation contrast (cf. Figure 6.2), was not observed in Figures 6.3b and 6.3c indicating that the plate packets were of similar orientation, with disorientations less than 5°. The grain size (EQAD) for the three microstructure are reported in Table 6.1 together with the total number of grains sampled for each specimen. Note that the total area sampled is much larger than the size of the representative maps shown in Figure 6.3. After 1 treatment cycle, a 2 fold increase in grain size is measured for the α-phase, while after 5 treatment cycles a grain size 3 times that of the as-received material was obtained.

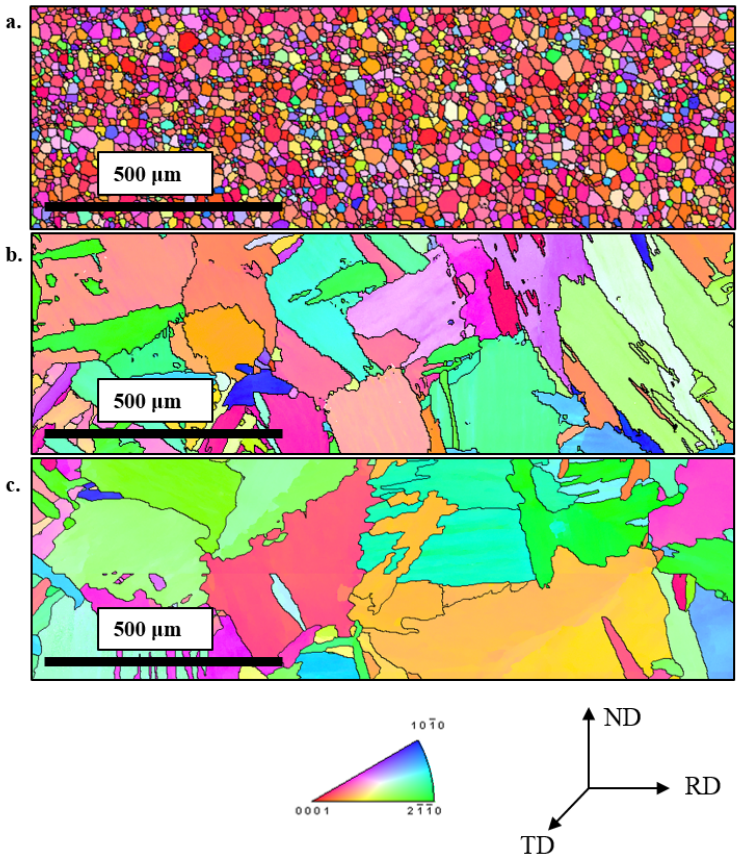

Figure 6.3: Representative inverse ND pole figure maps (ND - IPF maps, A = 6.49 x 10^5 µm^2) showing the microstructure and microtexture in the: a) as-received state, b) after 1 treatment cycle, c) after 5 treatment cycles. In a), b), and c) the area of observation corresponds to the region where the ultrasonic pulse was induced and measured. Note that these regions have been cropped from much larger maps, the overall size of the parent map being given in Table 6.1. Full comboscan maps provided in Appendix A.

Table 6.1: Microstructural parameters of commercially pure titanium in the: as-received condition, after 1 treatment cycle, after 5 treatment cycles

Specimen	EQAD (μm)		Grains Sampled		Overall Map Size (10^6 μm^2)
Cycles of Treatment	α	β	α	β	
as-received	42	-	6371	-	8.67
1 cycle	70	242	846	60	3.24
5 cycles	145	289	316	67	5.23

Grain boundary disorientations for specimens following 1 treatment cycle (Figure 6.3b) and 5 treatment cycles (Figure 6.3c) were calculated from the grain orientations. Each boundary was selected according to the classification proposed by Wang et al. [88] with a tolerance of ± 5°. The results of this analysis are shown in Figure 6.4a and Figure 6.4b where coloured boundaries correspond to one of the 6 reduced axis-angle pairs (provided in Table 6.2) that describe α/α boundaries in the case where both crystals nucleated from the same β grain as distinct α variants defined by the Burgers orientation relationship. The black grain boundaries do not share a special orientation relationship and therefore are taken as the boundaries between α grains nucleated from two different β grains. Assuming that the α grains nucleate at β grain boundaries [95], the boundary between these two α grains can be considered as the approximate location of a prior β grain boundary. The resulting grain boundaries of the parent β-phase are given in Figure 6.4c and Figure 6.4d for specimens after 1 and 5 treatment cycles respectively. This method allows for the estimation of the mean EQAD of the β grains for these two specimens, which are presented in Table 6.1. The β grain size is estimated to be very large by this technique. After 1 treatment cycle, a 6 fold increase in grain size is measured for the β-phase when compared to the as-received EQAD. After 5 treatment cycles, a grain size 7 times that of the as-received material was obtained (cf. Table 6.1). This observation suggests extensive grain growth occurring above the β transus, which has been observed before for commercially pure titanium [11].

Table 6.2: Reduced axis/angle pairs for each type of α/α boundaries that can result from the same parent β grain [88]

Type	Axis	Angle	Color
1	I	0°	
2	[1 1 $\bar{2}$ 0]	60°	
3	[$\bar{1}$8 13 31 8]	60.83°	
4	[$\bar{1}$0 5 5 $\bar{3}$]	63.26°	
5	[8 $\bar{1}$9 11 0]	90°	
6	[0 0 0 1]	10.53°	

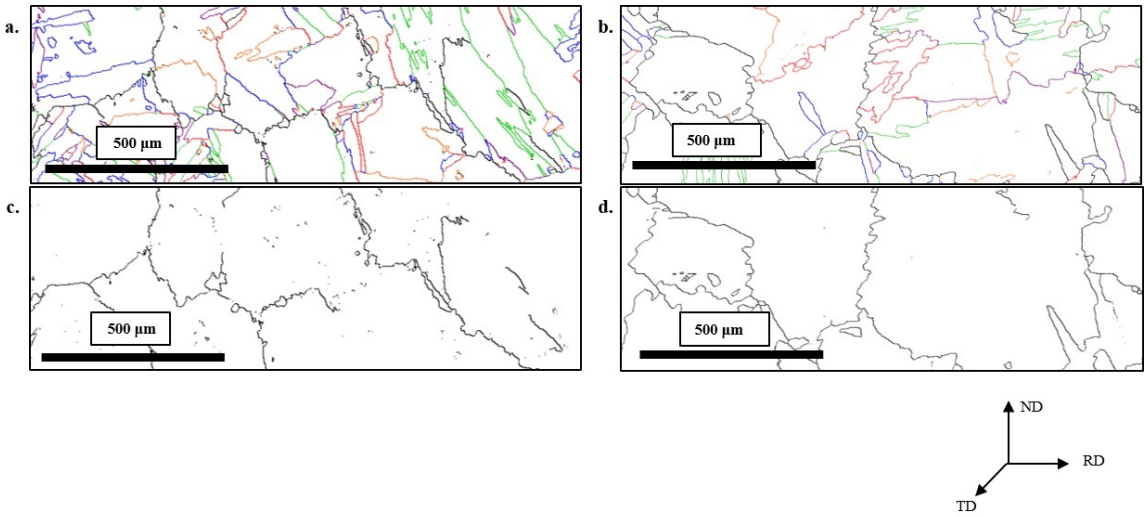

Figure 6.4: Grain boundary maps demonstrating: a) the α/α and b) prior β special boundary map of a specimen after 1 treatment cycle, and c) the α/α and d) prior β special boundary map of a specimen after 5 treatment cycles. Full comboscan maps provided in Appendix A.

Figure 6.5 shows the pole figures extracted from the full set of EBSD measurements (cf. Table 6.1) for specimens in the as-received state, after 1 treatment cycle and after 5 treatment cycles. The initial as-received texture shown in Figure 6.5a has a near basal texture with a distinct split around the rolling direction, characteristic of a microstructure initially cold-rolled and annealed [11, 96]. The spotty textures observed after 1 cycle and after 5 cycles in Figure 6.5b and Figure 6.5c are characteristic of the coarse α grain size given in Table 6.1.

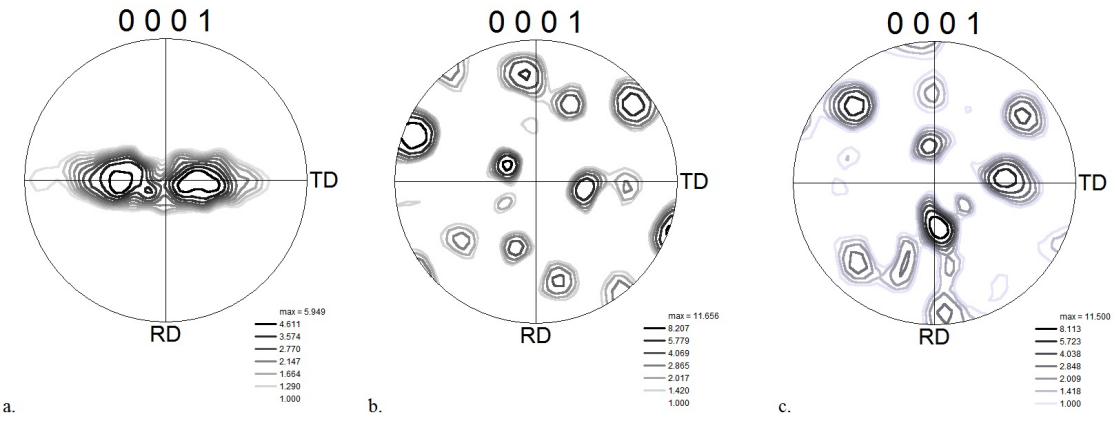

Figure 6.5: Pole figures showing texture in the: a) as-received state, b) after 1 treatment cycle, c) after 5 treatment cycles

6.4 Evaluation of the ultrasonic velocity

Figure 6.6 presents the ultrasonic velocity measured during the 1st, 2nd, and 5th thermal cycles. The velocity in the α-phase is observed to decrease linearly with temperature as expected based on the change in density [25] and elastic constants [36, 38]. In all cases, the linear portion of the heating segment of the curves was observed up until a temperature of approximately 885 °C, which is close to the expected equilibrium β transus temperature for pure titanium (882 °C) [9]. Similarly, a linear increase of velocity with decreasing temperature was observed in the α-phase for temperatures below $\sim$ 850 °C. At high temperature, the β-phase exhibits a weakly temperature dependent ultrasonic velocity, which is consistent with previous experiments [38].

The velocity in the α-phase is measurably higher at 700 °C in the heating stage of the 1st cycle compared to the value observed at 700 °C after cooling. This difference suggests a strong evolution of the texture during the $\alpha \rightarrow \beta \rightarrow \alpha$ transitions, which is consistent with the texture and grain size changes shown in Figure 6.4a and Figure 6.4b. Aside from as-received specimen, the velocity measured at 700°C for all other conditions (on heating and on cooling) were found to be the same within experimental error. This suggests that, while the texture change on the 1st treatment cycle strongly affects the velocity measurement, subsequent texture changes on heating/cooling do not. In contrast, the absolute value of the velocity of the β-phase measured, for example, at 920 °C was found to vary strongly from one experiment to another. Repetitions of the 1 cycle experiment (Figure 6.6d) showed a wide range of final velocities of the β-phase. As will be discussed

below, this specimen-to-specimen variation is indicative of statistical scatter arising from having few grains in the measurement volume. The increasing grain size observed upon repeated cycling was demonstrated in the *ex-situ* results, and as a consequence, the number of grains sampled in the volume scanned by the ultrasonic is also reduced (cf. Table 6.1).

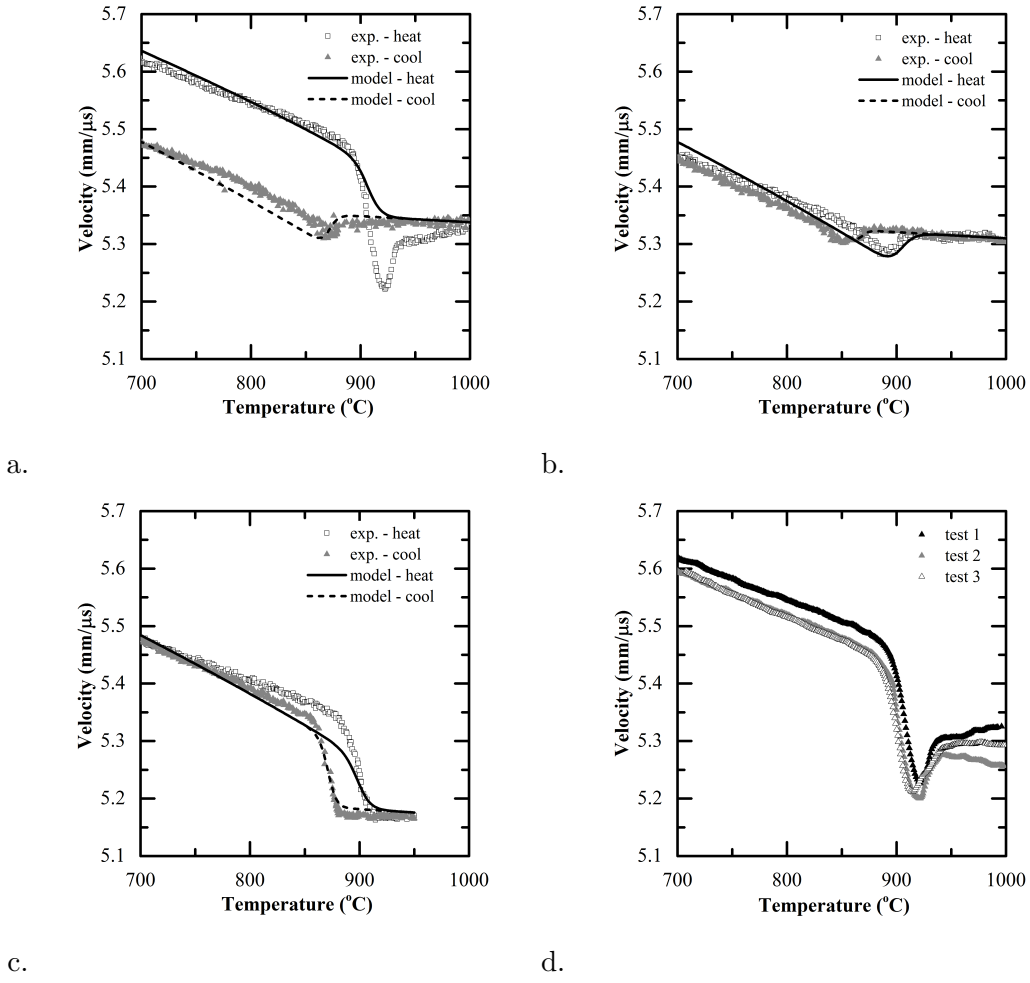

Figure 6.6: Comparison of calculated velocity values to LUMet observations for heating and cooling of the a) 1st treatment cycle, b) 2nd treatment cycle, and c) 5th treatment cycle, along with d) a compilation of velocity profiles demonstrating the variation in β velocity during heating in the 1st cycle

To extract the phase transformation kinetics from the measurements shown in Figure 6.6, a model is required that combines the temperature dependence of the density and elastic constants. The temperature variation of the density of the α-phase and β-phase was estimated based on the CALPHAD approach described in Lu *et al.* [25]. The temperature dependence of the five independent elastic constants of the α-phase for pure titanium were obtained by linearization of the data

provided by Ogi *et al.* [38], and Fisher and Renken [36]. To calculate the polycrystalline ultrasonic velocity of the α-phase, the polycrystalline averaged stiffness tensor was calculated using EBSD measured texture data (Sections 2.5.3 and 2.5.5) [80]. The Cristoffel tensor was next constructed from the polycrystalline stiffness tensor, and the pressure wave modulus, $\lambda_{1,\alpha}^{\text{Hill}}$, obtained as the appropriate eigenvalue [79]. The single crystal elastic constants for unalloyed β-phase in Ti have been reported by Fisher and Dever [36]. These experiments as well as those of Senkov *et al.* [1] point to a very low temperature dependence for the β-phase. Notably, the results also show a very high elastic anisotropy with $2C_{44}/\left(C_{11}-C_{12}\right) \approx 4.8$ [36]. As with the α-phase, one can calculate the expected ultrasonic velocity knowing the elastic constants only if the crystallographic texture is also known. In the present work, the texture of the β-phase could not be directly evaluated. Lacking this data, the value of the pressure wave modulus for the β-phase was fixed based on observed experimental velocity at 1000 °C. The temperature dependence of $\lambda_{1,\beta}^{\text{poly}}$ was then fit to the experiments. Averaging the slope of the velocity-temperature plot for all runs within the fully β condition led to a temperature dependence of -0.0001 $\text{mm.}\mu\text{s}^{-1}.^{\circ}\text{C}^{-1}$. This was therefore used in the model as the temperature dependence of the velocity in the β-phase. Figure 6.7 provides an overview of the anisotropy dependent modeling of velocity.

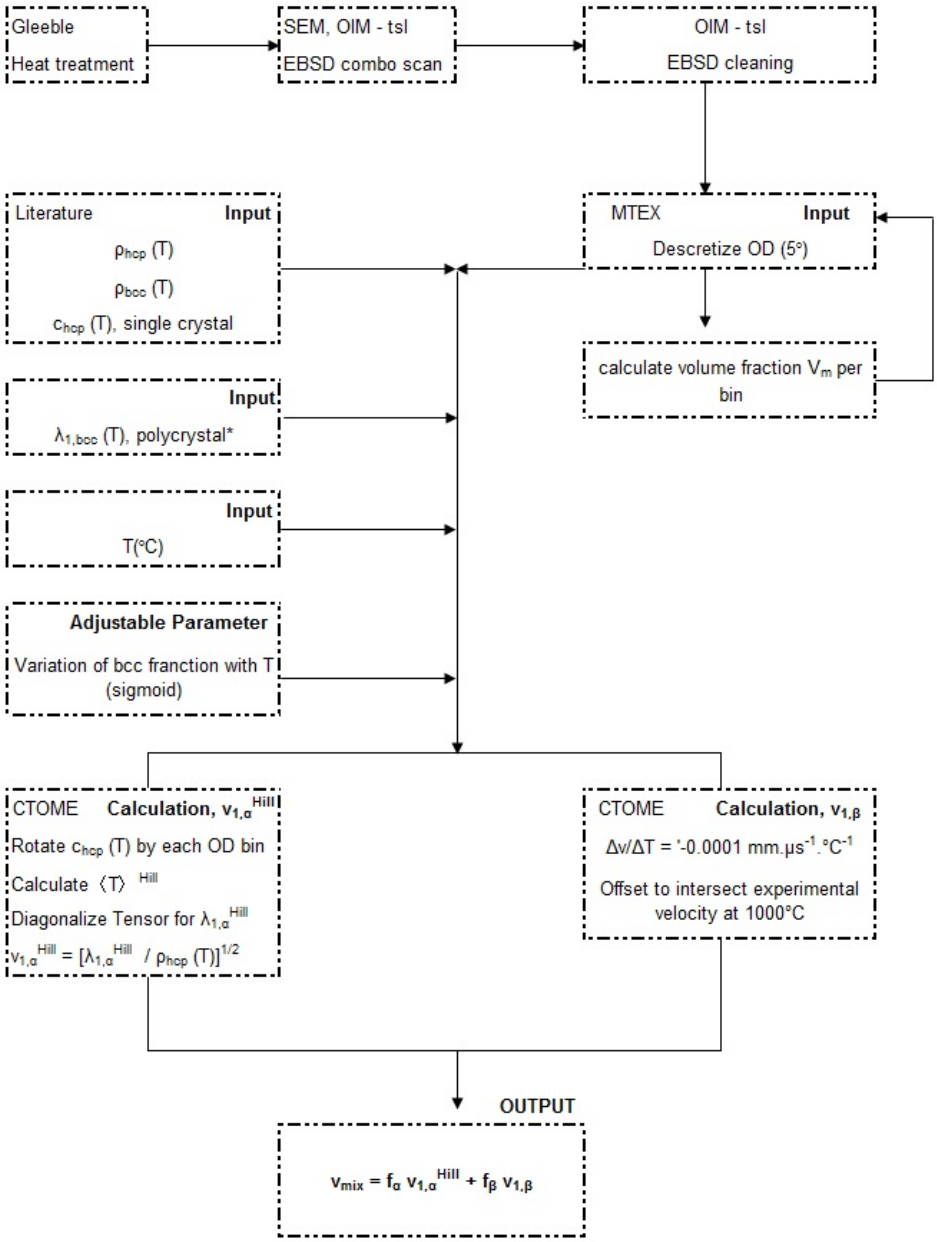

Figure 6.7: Overview of the model used to calculate the velocity in a bulk aggregate of titanium. *$\Delta v/\Delta T$ back-calculated from average slopes of experimentally observed velocities and off-set so model velocity intersects experimental at 1000 °C

To calculate the ultrasonic velocity in the regime where two phases co-exist, one must make an assumption regarding the way in which the velocities of the individual phases contribute. As explored in Chapter 5, the predicted velocity is only weakly dependent on the assumed averaging scheme when the density and moduli are similar. In the present alloy, the percent differences in the modulus and densities of the α-phase and β-phase are 6.8% and 0.18 %, respectively when

calculated at the β-transus temperature under a polycrystalline aggregate assumption. Given these small differences and the sensitivity curves provided in Section 5.6 a simple linear addition law is sufficient to predict the aggregate velocity:

$$v_{mix} = \left(1 - f_\beta\right) v_\alpha + f_\beta v_\beta = \left(1 - f_\beta\right) \left(\frac{\lambda_{1,\alpha}^{Hill}}{\rho_\alpha}\right)^{1/2} + f_\beta \left(\frac{\lambda_{1,\beta}^{poly}}{\rho_\beta}\right)^{1/2} \tag{6.1}$$

Using the values of $\lambda_{1,\alpha}^{Hill}$, $\lambda_{1,\beta}^{poly}$, ρ_α and ρ_β as described above, the only unknown parameter is the volume fraction of the β-phase, f_β. To simplify fitting the experimental data, the variation of f_β with temperature was assumed to vary sigmoidally:

$$f_\beta = \frac{1}{\left(1 + e^{(-A_1 * (T - A_2))}\right)} \tag{6.2}$$

Where A_1 and A_2 are adjustable parameters, and T is temperature in °C. The optimal values of adjustable parameters for each cycle are shown in Table 6.3.

Table 6.3: Best fit values of the adjustable parameters (A_1 and A_2) in equation 6.2 obtained by comparing during fitting the heating and cooling portions of the experimental data in Figure 6.6 for the 1^{st}, 2^{nd}, and 5^{th} cycles

	heating		cooling	
Cycle	A_1	A_2	A_1	A_2
1^{st}	0.219	908	0.260	871
2^{nd}	0.166	903	0.361	868
5^{th}	0.166	899	0.260	872

Figure 6.6 compares the experimentally measured and numerically predicted ultrasonic velocities (via equation 6.1). Figure 6.8 shows that the transformation kinetics required to fit the experiments (via equation 6.2) are nearly the same for the all of the heating cycles and all of the cooling cycles, as one would expect. The model described above, accounting for the temperature dependence of the material properties, texture, and phase fraction, adequately describes the variation of ultrasonic velocity during cooling in each of the cycles shown in Figure 6.6. In the case of the 5-cycle specimen during the heating stage one sees a discrepancy between the temperature dependence of the velocity

in the α-phase during heating. As noted above, for this specimen the texture of the α-phase was measured only after the 5^{th} treatment cycle, not before. This result would suggest that the texture before and after the 5^{th} treatment cycle was not the same, leading to the good prediction of the velocity in the α-phase on cooling but a poor fit on heating. If this was the case, then one might expect the same problem in the case of the specimen cycled twice where the texture was measured prior to, but not after, the thermal cycle. Another factor must be considered in this analysis, however. Examining the data in Table 6.1, one sees that the α grain size increases drastically between the 2^{nd} and 5^{th} treatment cycle. This suggests that the discrepancy in the model fit to the heating and cooling segments of the 5^{th} treatment cycle comes from the sampling of too few grains in the α-phase. This leads to incomplete statistical sampling of the texture and the unsuitability of the texture measured after the cycle as a replacement for the texture before the cycle. Conversely, the α-phase grain size in the case of the specimen after one treatment cycle is only approximately half of the grain size after 5 treatment cycles.

A more drastic discrepancy between the model and experiments occurred during the $\alpha \rightarrow \beta$ transformation on heating during the 1^{st} cycle. In this case the experiments reveal a surprising variation in the velocity, its value first dropping before once again increasing. This result was reproduced on 3 specimens, though as noted above, the final high temperature velocity of the β-phase varied strongly from one specimen to the next (cf. Figure 6.6d). One interpretation of this result could be that the $\alpha \rightarrow \beta$ transformation does not finish until the end of the strong increase in velocity following the minimum at 922 °C. This, however, would suggest drastically different transformation kinetics on the first heating compared to all of the other specimens studied. If, however, one considers the bottom of the minimum in velocity as the end of the transformation, then one finds very close agreement for the transformation kinetics with the other two conditions during heating. This observation suggests that another mechanism is more likely to cause the strong increase in velocity in the β-phase following the end of the transformation. It is notable that this increase in velocity continues to the highest temperature monitored, this temperature dependence being abnormal compared to the other two specimens.

One possible explanation for the rapid increase in velocity is that it is due to the very rapid grain growth that has been reported in the β-phase just following the completion of the phase transformation [11, 12]. The α grain size of the as-received material was shown in Table 6.1 to be

42 μm while the back-constructed β grain size after the 1st treatment cycle was estimated to be ∼ 242 μm. As shown by the *in-situ* EBSD observations of Seward *et al.* [11], the formation of the β-phase occurs both within the grain and from the α/α grain boundaries simultaneously. They were able to observe directly and *in-situ* a drastic evolution in both the grain size and texture of the β-phase. Significantly, the texture at the end of the α → β transformation has been noted to be strongly cube-like, this texture having a very low longitudinal wave velocity [11, 97, 98]. Using the single crystal elastic constants from Fisher and Dever [36] at 1000 °C a lower-bound velocity of 5.139 mm.μs^{-1} would be expected for propagation along a ⟨100⟩ direction. The fact that all tests performed showed very similar values of the minimum in velocity would be consistent with all specimens transforming to a similar cube texture on the 1st heating cycle. The scatter in the velocities of the β-phase at high temperature would also be consistent with this interpretation as this is what would be expected to arise from the large elastic anisotropy of the β-phase combined with statistical scatter in texture as the number of grains sampled by the ultrasonic wave decreases with further grain growth.

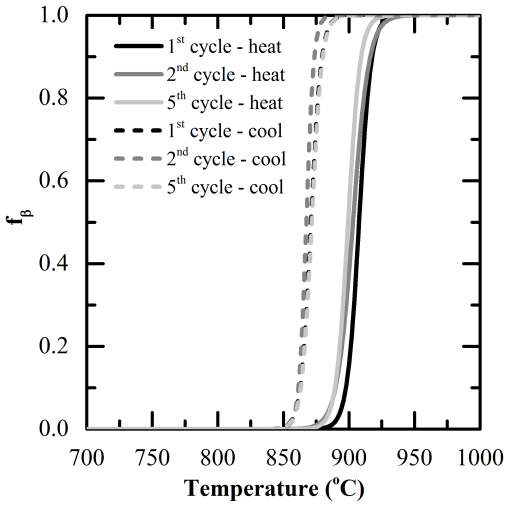

Figure 6.8: α → β and β → α phase transformation kinetics obtained from Equation 3 using the parameters given in Table 6.3 for specimens during the 1st, 2nd and 5th cycle, respectively

6.5 Chapter summary

The ultrasonic velocity has been shown to be sensitive to $\alpha \rightarrow \beta$ and $\beta \rightarrow \alpha$ transformation in commercially pure titanium, despite the similarity of density and elastic modulus of the two phases. Converting this ultrasonic velocity to a phase fraction is, however, complicated by the effect of a strong starting texture and extensive grain growth in the β-phase. Under such conditions it is shown that one needs to accurately incorporate the local texture into the analysis in order for one to predict the experimentally measured ultrasonic velocity from known material properties. For tests where the texture is well known, e.g. in cases where we were able to measure the texture on cooling, an excellent agreement between the predicted and measured velocity could be obtained. In contrast, the variation of ultrasonic velocity in cases where the texture was not well known led to an inability to directly match the simulation results. Most notably, the non-monotonic variation of the velocity with temperature during the 1^{st} treatment cycle was attributed to a velocity change caused first by the phase transformation (decrease in velocity) followed by rapid grain growth in the β-phase (increase in velocity). This change is qualitatively consistent with the recent observations of the $\alpha \rightarrow \beta$ transformation by *in-situ* EBSD [11].

Chapter 7

In-situ Laser Ultrasonic Measurement During Aging of Ti-5553

7.1 Introduction

In this Chapter, the laser ultrasonic technique is used to monitor the $\beta \rightarrow \alpha$ phase transformation in the alloy Ti-5Al-5Mo-5V-3Cr. The measurements are conducted during isothermal aging scenarios at 700 °C after solution treating. In particular, the evolution of the longitudinal wave velocity is measured during the precipitation reaction that occurs during the isothermal hold below the transus. Quantitative *ex-situ* metallography are correlated to the variation of the velocity observed during the precipitation sequence. Finally, the absolute change in velocity is modelled to contrast and compare *ex-situ* obtained information and the *in-situ* measurement of ultrasonic velocity for the prediction of the α precipitation kinetics in this material.

7.2 Characterization of the as-received material

The initial microstructure of the forged ingot was composed of large and deformed β grains, with globular primary α regions. When viewing along the transverse direction, the globular primary α precipitates are consistently round, with a mean equivalent area diameter (EQAD) of 2.58 μm, as shown in Figure 7.1. The as received condition also demonstrated a relatively large β grain size relative to the α precipitates. Figure 7.2 shows globular primary α precipitates dispersed throughout

a large β grain.

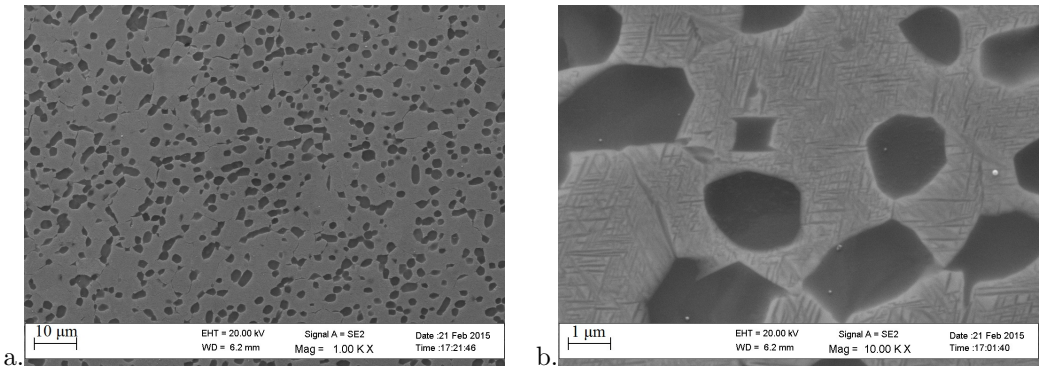

Figure 7.1: Secondary Electron Image (SEI) demonstrating the as-forged Ti-5553 microstructure at magnifications of a) 1000x b) 10 000x

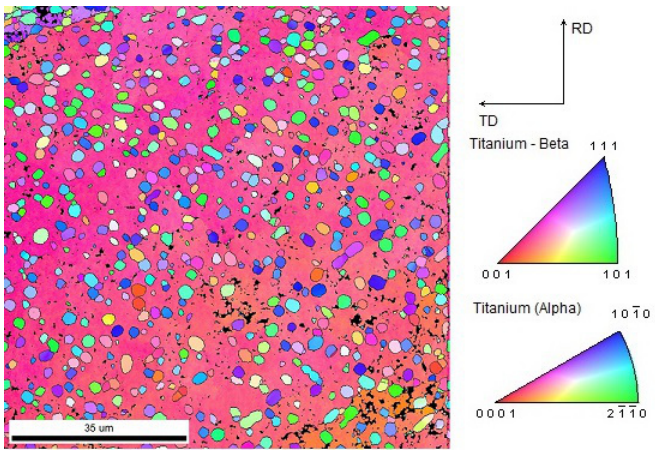

Figure 7.2: Electron backscatter diffraction (EBSD) inverse pole figure (IPF) map demonstrating globular primary α precipitates dispersed in a large β grain

7.3 *Ex-situ* metallography

Figures 7.3, 7.4 and 7.5 shows the microstructural evolution with time during an isothermal holding treatment at 700 °C. Figure 7.3 shows the control specimen, after being cooled at 6.7 °C.s^{-1} to 700 °C and then quenched immediately. A fully β microstructure with an EQAD of 182 µm is observed after the 15 minute solutionizing treatment. Figure 7.4 shows an EBSD phase map demonstrating precipitation along β grain boundaries after 5 minutes of treatment. EBSD was employed in this instance because the phase amount was very limited (0.3 vol. % α), and the phase contrast was difficult to distinguish from the overwhelming orientation contrast between β grains. Conversely,

Figure 7.5a through 7.5e were taken using backscatter electron (BSE) contrast. Figure 7.5a shows α_{W1} Widmanstätten plates initiating at the grain boundaries and growing in parallel packets into the grain after 10 minutes where 2.0 α vol. % has formed. After 33 minutes 12.2 α vol. % has formed and α plate packets (α_{W2}) are seen nucleating throughout the β grain in addition to growing out from the β grain boundaries (Figure 7.5b). Figure 7.5c shows that after 53 minutes 16.3 % of the microstructure was α and demonstrated a mixture of morphologies. After 75 minutes, 31.5 % of the microstructure is composed of the α phase and the majority of the α phase is still present near the β grain boundaries (Figure 7.5d). Finally, after 180 minutes 39.4 % of the microstructure is homogeneously distributed α precipitates (Figure 7.5e). The fraction of α observed after each time along with the standard deviation (calculated from 5 BSE measurements per specimen) is summarized in Table 7.1.

Table 7.1: Phase fraction of α (f_α) precipitated during isothermal holding at 700 °C

Holding Time (min.)	f_α (%)	Standard Deviation
5	0.3	-
10	2.0	0.5
33	12.2	2.5
53	16.3	3.7
75	31.5	3.0
180	39.4	2.9

Figure 7.6 demonstrates the variety of morphologies that result during precipitation of the α phase in an aged specimen. Figure 7.6a presents a BSE image demonstrating grain boundary alpha (α_{GB}), Widmanstätten side plates (α_{W1}) growing out from the α_{GB}/β interface, along with plate packets nucleating within the grain (α_{W2}). Figure 7.5 and 7.6 demonstrate that the pre-existing β grain boundaries are the dominant nucleation sites for the α phase. Similar morphologies have been observed during aging treatments of β-stabilized alloys in the literature [60] [58]. Figure 7.6b shows the inverse pole figure (IPF) map of the same area photographed in Figure 7.6a. The α_{GB} is shown as a thin film resulting from the coalescence of α precipitates nucleating between the two prior existing β grains. Figure 7.6b shows that the plates nucleating near a respective boundary line of α_{GB} will often share the same orientation as the α_{GB}. However, other α_{W1} variants are observed as plates extending from the boundaries.

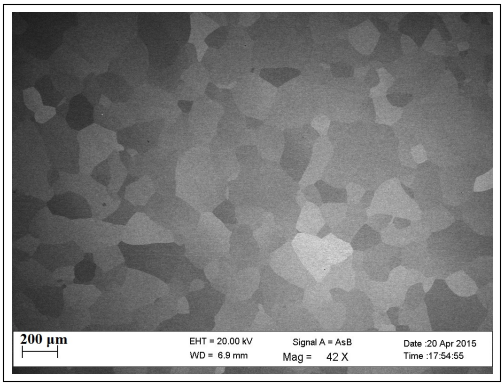

Figure 7.3: BSE images taken at 20 kV and at low magnification of a specimen representative of the starting condition at the onset of the 700 °C isotherm (solutionized for 15 minutes at 900 °C, then cooled to 700 °C at 6.7 °C.s^{-1} and quenched).

Figure 7.4: EBSD phase map taken after a specimen was held at 700 °C for 5 minutes where black and white indicate the α and β phases, respectively

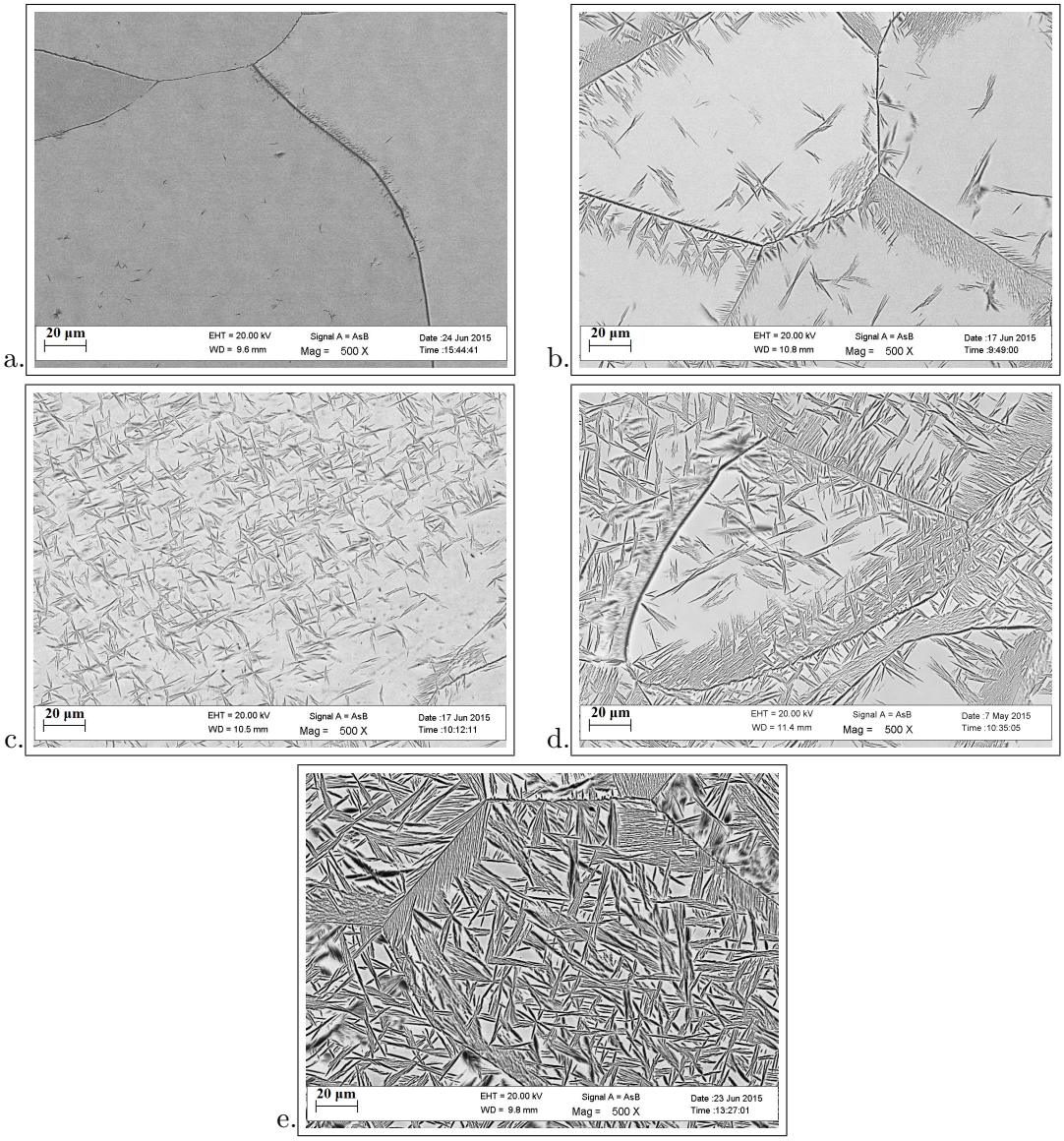

Figure 7.5: BSE images taken at 20 kV and a magnification of 500x of specimens held at the isothermal treatment for a) 10, b) 33, c) 53, d) 75 and e) 180 minutes.

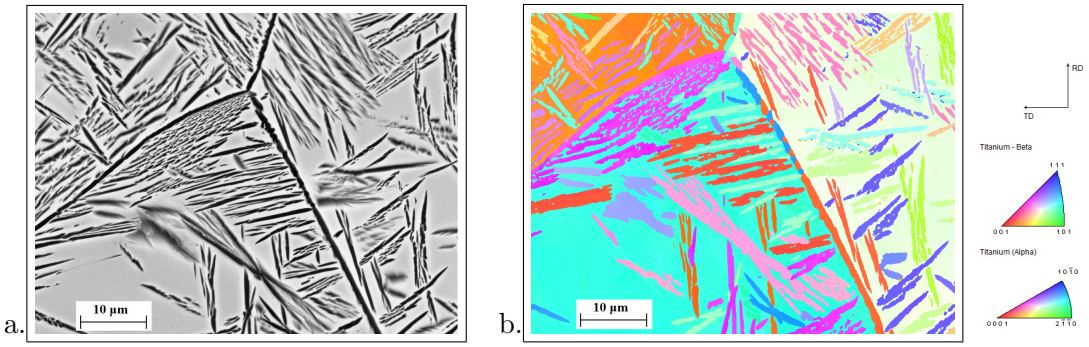

Figure 7.6: Triple point β boundary in a specimen aged for 75 minutes at 700 °C demonstrating films of α_{GB} forming between the β grains and the growth of α_{W1} side-plates into the β grain visualized as a a) backscatter electron image and b) inverse pole figure map

Figure 7.7 shows the plot of the precipitate phase fraction (f_α) evolving over the time held at treatment. A sigmoidal shape is clearly evident with kinetics slowing at the three hour mark, near a volume fraction of 39.4 ± 2.9 % which is in good agreement with the equilibrium value of α, $f_{\alpha,eq}$ = 43%, calculated via the TTTI3 database in Thermocalc at the holding temperature T = 700 °C. A sigmoidal fit (the blue line in Figure 7.7) is shown as a guide to the eye.

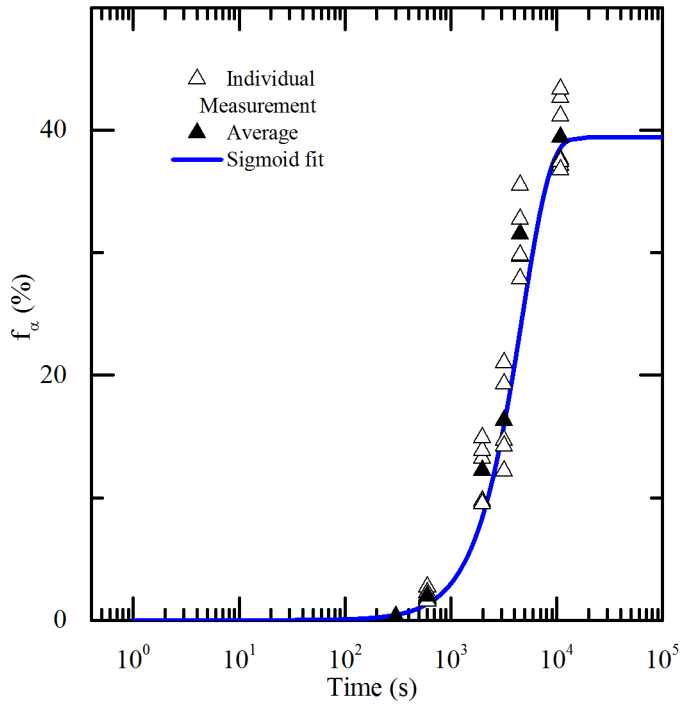

Figure 7.7: Measurements of isothermal α precipitation obtained via *ex-situ* metallography

7.4 Evaluation of ultrasonic velocity

Figure 7.8a shows that the initial value of velocity for the fully β condition varies from 5.85 to 5.97 $mm.\mu s^{-1}$. This variation is related to various uncertainties in the absolute measurement of velocity and will be discussed further in this section. When the polycrystalline P-wave moduli computed under isotropic assumption at 700 °C and densities are used (as described in Section 2.5.4), the computed velocities in the α and β phases are $v_{\alpha,poly} = 5.48$ $mm.\mu s^{-1}$ and $v_{\beta,poly} = 5.107$ $mm.\mu s^{-1}$ which means a change of 0.373 is expected for the complete (100 %) $\beta \rightarrow \alpha$ transformation. This means that after 180 minutes, given the *ex-situ* observed α phase fraction of $f_{\alpha,t=180min} = 39.4$ % (cf. Table 7.1), the predicted velocity would increase by 0.147 $mm.\mu s^{-1}$. This is comparable to the LUMet observed increase in velocity of 0.152 $mm.\mu s^{-1}$.

When the relative change in velocity ($\Delta v = v_t - v_\beta$) is calculated from the laser ultrasound data for each specimen, the curves collapse on one another as shown in Figure 7.8b. However, the absolute values of the raw velocities measured in LUMet seem to be substantially higher than what is predicted using the material properties under a polycrystalline assumption.

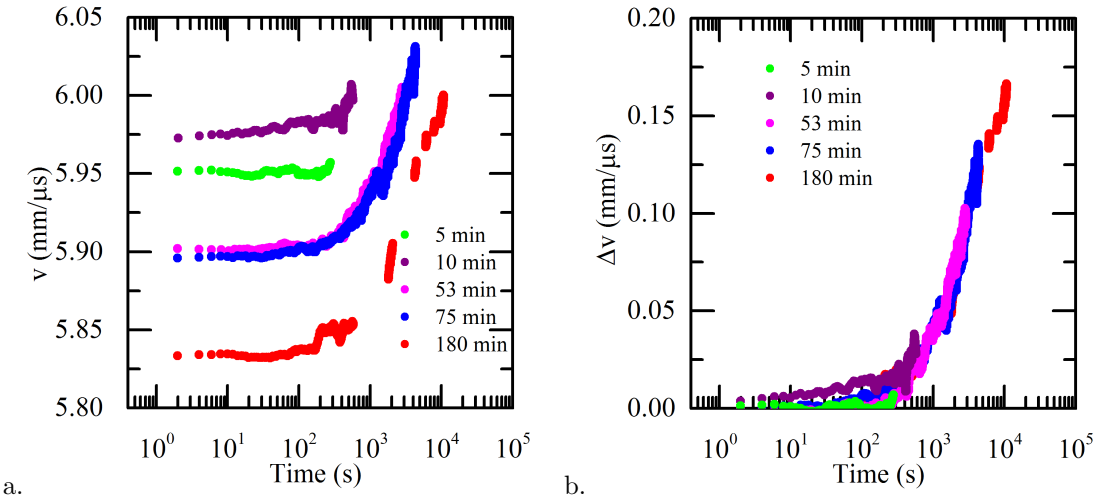

Figure 7.8: Comparison of a) raw absolute velocities at various isothermal holding times, and b) *in-situ* ultrasonic observation depicting relative change in velocity ($\Delta v = v_t - v_\beta$)

Four possible sources of error were investigated as the cause of the observed offset of absolute value in velocity. These sources of potential errors included the effect of texture, composition, thickness anomalies, and asymmetry of the measured waveforms. The two material dependent properties, texture and composition, can both alter the elastic response in a given material. If the

polycrystalline aggregate assumption was inappropriate, and instead of using the polycrystalline values one were to compute the velocity by accounting for texture (following Section 2.5.3), one would find the anisotropy of the hcp and bcc crystals are not sufficient to account for the differences in the observed and predicted absolute values of velocity. For instance, when velocity is computed as a function of orientation, the hcp unit cell demonstrates a minimum or maximum velocity when a wavefront is propagating within the basal plane or parallel to the c-axis, respectively. At 700 °C, the upper and lower bounds for velocity in an anisotropic hcp titanium unit cell are:

$$(\varphi_1, \Phi, \varphi_2) = (0, 0, 0) \rightarrow \mathrm{v}_\alpha = 5.946 \quad \mathrm{mm.\mu s^{-1}} \tag{7.1}$$

$$(\varphi_1, \Phi, \varphi_2) = \left(0, \frac{\pi}{2}, 0\right) \rightarrow \mathrm{v}_\alpha = 5.376 \quad \mathrm{mm.\mu s^{-1}} \tag{7.2}$$

Where φ_1, Φ, and φ_2 are the Euler angles given in Radians. Thus, even in a hypothetical condition where all the α crystals were aligned such that their c-axes were all parallel to the wave propagation direction, a velocity of 5.946 $\mathrm{mm.\mu s^{-1}}$ would be possible, which is significantly lower than the velocities shown in Figure 7.8.

For the bcc case, the upper and lower bounds in predicted velocities were given when the ultrasonic pulse propagated through $\{110\}\langle 1\bar{1}1\rangle$ and $\{101\}\langle 100\rangle$, respectively. The single crystal elastic constants are only available in the literature at 1000 °C, so the velocities have been computed at 1000 °C. At 1000 °C, the upper and lower bounds for an anisotropic bcc titanium unit cell are:

$$(\varphi_1, \Phi, \varphi_2) = \left(0, \frac{\pi}{2}, 0\right) \rightarrow \mathrm{v}_\beta = 5.55 \quad \mathrm{mm.\mu s^{-1}} \tag{7.3}$$

$$(\varphi_1, \Phi, \varphi_2) = \left(0.61548, \frac{\pi}{2}, \frac{\pi}{4}\right) \rightarrow \mathrm{v}_\beta = 4.76 \quad \mathrm{mm.\mu s^{-1}} \tag{7.4}$$

This prediction is limited by the fact that the single crystal elastic constants only exist for bcc titanium at 1000 °C, and that the experimental velocities were observed at 700 °C. However, considering the Bulk modulus observed by Ogi *et al.* [38] demonstrated a minute temperature dependence above the transus, the 300 °C temperature difference between predictive computation and the experiment is unlikely to account for the drastic difference between the predicted and

observed velocities (5.55 mm.μs^{-1} versus 5.83 - 5.97 mm.μs^{-1}). Consequently, neither the anisotropy in the bcc nor hcp phase is large enough to account for the high velocities shown in Figure 7.8a.

Upon examining Figure 7.8b, it can be observed that the relative change in velocity ($\Delta v = v_t - v_\beta$) of each trial overlapped. The EQAD of the bcc grains at the onset of the treatment was 182 μm. In Chapter 6 it was seen that the commercially pure titanium specimen that endured 5 cycles exhibited an EQAD of only 142 μm (cf. Table 6.1). Based on that initial assessment, one would assume orientation effects would be a significant contributor to variation in velocity. However, Figure 7.9 demonstrates the reason why texture is such a significant contributor in Chapter 6 and not here. Figure 7.9a shows the EBSD obtained microstructure of hcp commercially pure titanium after 5 cycles of heat treatment. Extremely coarse grains (diameter $\geq$ 500 μm) are mixed with smaller grains (diameter $\leq$ 50 μm). Conversely, Figure 7.9b demonstrates a microstructure with a fairly uniform distribution of grain size. The area weighted grain diameter (d_A) of the microstructures shown in Figure 7.9a and 7.9b are 538 μm and 289 μm, respectively, where the area weighted grain diameter (d_A) was calculated by:

$$d_A = \frac{1}{\sum_{i=0}^{n} A_i} \sum_{i=1}^{n} A_i d_i \tag{7.5}$$

Where A_i is the area of a given grain, d_i is the diameter of a given grain, and n is the total number of grains.

The d_A of the treated commercially pure titanium specimen is significantly larger than its corresponding EQAD, as well as the d_A and EQAD of the Ti-5553 specimen. This suggests, that the orientation of large grains, such as the big blue one shown in Figure 7.9a contribute significantly to the velocity of the wave, and in cases where there are sufficient grains with a smaller area weighted fraction, such as in Figure 7.9b, velocity can be predicted using a polycrystalline assumption. This is self consistent with the fact that all the velocity curves collapse when the relative change in velocity ($\Delta v = v_t - v_\beta$) is calculated, as shown in Figure 7.8b.

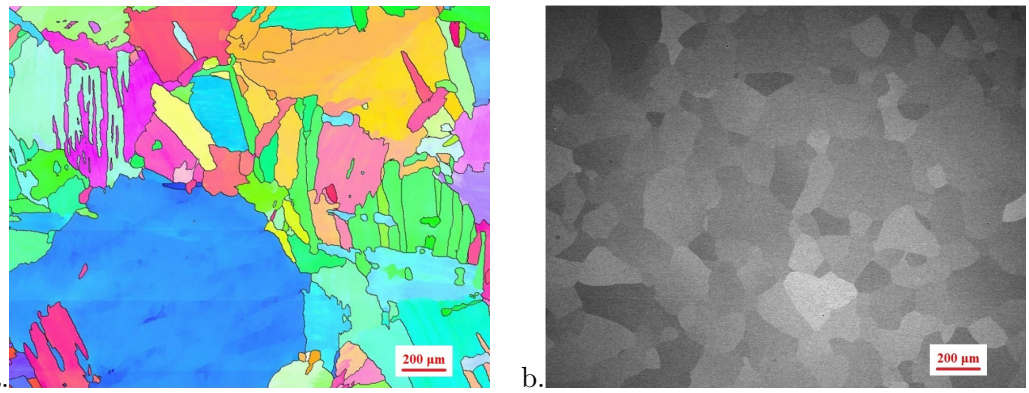

Figure 7.9: A comparison of: a) Inverse ND pole figure map (ND - IPF map) showing the microstructure and microtexture in hcp commercially pure titanium after 5 treatment cycles, and b) BSE image of a Ti-5553 specimen solutionized for 15 minutes at 900 °C, then cooled to 700 °C at 6.7 °C.s^{-1} and quenched to depict the bcc microstructure at the on-set of the isothermal treatment

If one returns to the work of Fisher and Dever [37], the effect of alloy composition on elastic response in the bcc phase can be explored. Their work suggests that a percent change in the P-wave modulus (observed at 1000 °C) as high as 10.42 % can occur with Cr alloy additions of 14.62 wt. %. However, if one calculates the density of bcc Ti and bcc Cr at 1000 °C [25], and computes the alloy density using a rule of mixtures, and finally computes the predicted velocity, the largest observed percent change is 1.68 %. The effect of composition and elastic response in hcp crystals was explored by the work of Senkov *et al.* [1] which looked at the addition of interstitial hydrogen into titanium at 20 °C. Senkov *et al.* [1] found that an addition of 25 at. % H would increase the P-wave modulus by 4.64 %, which corresponded to a 2.29 % change in velocity. These two studies [1, 37] suggest composition does have a minor impact on velocity. However, how each element addition effects velocity can vary because it will affect both the aggregates elastic response and density.

The material dependent properties, such as texture and composition, alone do not account for the high observed velocities. Experimental error such as inconsistencies in specimen thickness and poor waveform quality can also contribute to an offset in absolute velocity. For example, with thickness of 3 mm input, CTOME will compute a velocity of 5.832 mm.µs^{-1} for the initial fully β condition (t = 0 min) at 700 °C in the specimen aged for 180 minutes. For the fully β specimen to lie within the predicted velocity range of [4.76, 5.55] mm.µs^{-1} a maximum thickness of 2.85 mm (yields a velocity of 5.54 mm.µs^{-1}) would be necessary. However, the specimens were machined with

consistent quality to the pure Ti specimens (used in Chapter 6) which were on par with predicted values.

The final source of error is inherent to the quality of the waveform itself. Figure 7.10a demonstrates the quality of the echos in the as-received state at room temperature (Reference (AR)), in the fully β condition at 700 °C (Reference (BCC)) and at an arbitrary, representative point during the isothermal holding treatment (Current signal). To obtain the results shown in Figure 7.8a, all echos were compared to the as-received state (cf. Section 4.3.3). While the selected reference contained symmetric echos with sharp peaks, its shape was inconsistent to the shape observed at high temperatures, which had deteriorated substantially. The echos captured at 700 °C (eg. Reference (BCC) and Current signal) were asymmetric, and attenuated considerably due to the large bcc grains. Thus, when the cross-correlation algorithm is employed in CTOME [89], a consistent mis-windowing can occur [99]. This can be explained by examining the cross-correlation functions produced when the current signal echo is compared to the as-received and fully β reference echos. The two resulting cross-correlation functions are shown in Figure 7.10b. Figure 7.10b shows that when the asymmetric current echo is compared to the symmetric echo (Reference (AR)), the resulting cross-correlation function is asymmetric. When the algorithm in CTOME selects the maximum amplitude (corresponding to the red dashed line shown on Figure 7.10b), it will underestimate the time delay, which leads to a higher computed velocity. Conversely, when an equally asymmetric and attenuated waveform (Reference (BCC)) is selected, the resulting cross-correlation function is symmetric, as shown by the black function in Figure 7.10b, where the black dashed line identifies the maximum amplitude and corresponding time delay. To ensure this offset was indeed occurring in each dataset, each data set was compared to their own 30^{th} echo (representative of the fully β condition observed during that particular treatment), and velocity was computed. All specimens observed a decrease in velocity of approximately 0.3 mm.μs^{-1}, indicating that the error introduced due to asymmetry of the waveform is both consistent and significant. Correction of this systematic error is beyond the scope of this thesis. However, since the asymmetry effects at 700 °C are consistent across the aging treatments for each specimen, the relative change in velocity is a valid measure of the transformation since this offset is consistently applied to all points.

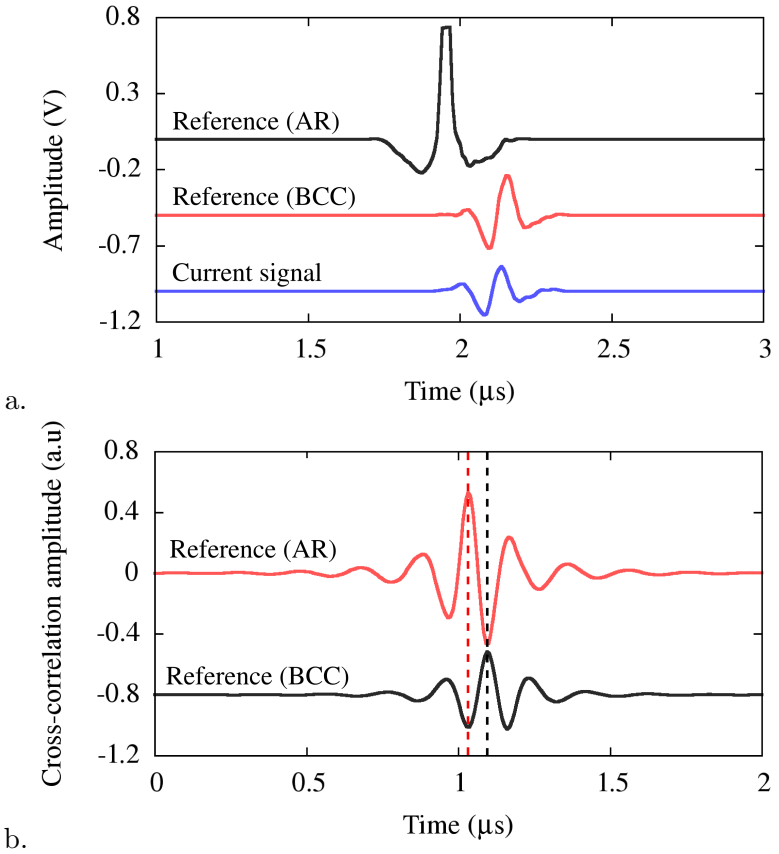

Figure 7.10: Schematic showing a) the as-received (AR) 2nd echo reference, fully β (BCC) 2nd echo reference, and an arbitrary and representative high temperature 2nd echo (Current signal), and b) cross-correlation function obtained when the current signal is compared to the as-received reference (red) and to the fully β reference (black). The dashed lines indicate the maximum amplitude, and corresponding time delay of each cross-correlation function.

Thus, the relative change in velocity depicted in Figure 7.8b was used to determine the kinetics over the five separate treatments. Any change observed in velocity is due to the formation of α precipitates throughout the specimen. The experimentally observed relative change in velocity (cf. Figure 7.8b) divided by the relative change predicted for the 100 % $\beta \rightarrow \alpha$ transformation ($\Delta v_{\beta\rightarrow\alpha}$ = 0.373 mm.μs^{-1}) yields the phase fraction of α precipitated during the isotherm:

$$f = \frac{\Delta v_{experimental}}{\Delta v_{\beta\rightarrow\alpha}} \tag{7.6}$$

Figure 7.11 compares the phase fraction obtained from normalizing the velocity data to the phase fraction measured via *ex-situ* metallography. Both the *in-situ* and *ex-situ* data sets overlap

well demonstrating that the monitoring velocity changes in Ti-5553 is an effective way to monitor precipitation and aging in this material. LUMet measured a systematically higher α phase fraction during the first 50 minutes of treatment. This has been attributed to difficulty in quantifying *ex-situ* the α phase fraction at earlier times due to the difficulty resolving the thin α_{GB} that nucleated on β-β grain boundaries using both the BSE and EBSD techniques. Overall, there seems to be excellent agreement between LUMet and metallography.

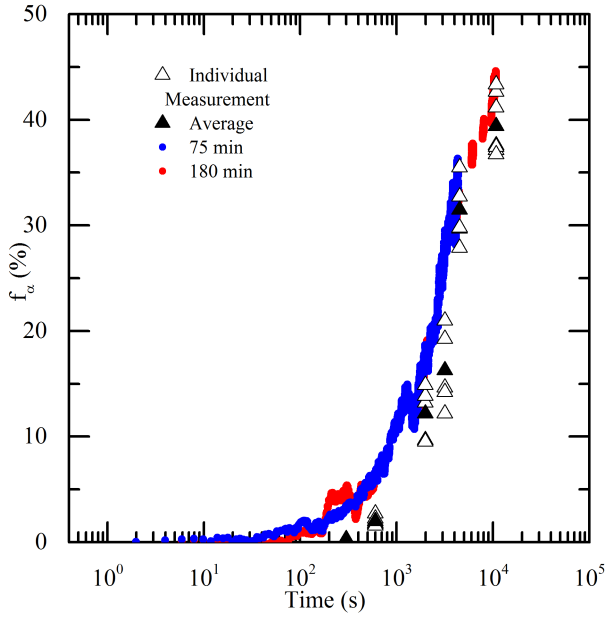

Figure 7.11: Comparison fraction of α precipitation obtained via *ex-situ* metallography and normalized velocity data during isothermal treatment

7.5 Chapter summary

The α precipitation kinetics of Ti-5553 were monitored using *in-situ* laser ultrasound and compared to *ex-situ* metallographic results. Three distinct morphologies of α phase were observed over the course of the isothermal holding treatment held at 700 °C. These morphologies consisted of: α_{GB} found precipitating on the grain boundaries, α_{W1} found growing as Widmanstätten plate packets into the grain after initiating along α_{GB} - β interfaces, and finally α_{W2} which was observed to form last, and consisted of Widmanstätten plate packets arranged in crossed bundles nucleating

throughout the grain body. Laser ultrasonics provided a fast, responsive and *in-situ* measure of the α precipitation kinetics in a material that demonstrated complex morphologies and microstructures.

Chapter 8

Summary and Future Work

8.1 Summary

This thesis developed strategies for interpreting laser ultrasonic data and monitoring the α/β phase transformations in cp-Ti and the metastable β alloy Ti-5553. This work validated the feasibility of LUMet as a non-destructive tool for monitoring the α/β phase transformation kinetics in these materials.

Three studies (Chapters 5, 6 and 7) were conducted to achieve this end. Firstly, a 2-D FEM simulation of wave propagation through a 2-phase aggregate was developed to understand the effects of precipitate spacial arrangement and phase fraction on the velocity signal. Chapter 5 found that the selection of a correct averaging scheme to predict ultrasound velocity in a 2-phase aggregate depended on the geometric configuration and the relative size of the pulse's wavelength compared to the microstructural feature size. Furthermore, sensitivity analysis of these results showed that of mixtures of phases with similar elastic properties and densities (such as in α and β titanium), the possible averaging schemes collapse onto each other and produce similar velocities, and thus using a rule of mixtures is sufficient.

The second study presented in Chapter 6 subjected cp-Ti specimens to cycles of continuous heat treatments above the transus temperature. The ultrasonic velocity was shown to be sensitive to both the $\alpha \rightarrow \beta$ and $\beta \rightarrow \alpha$ transformations in cp-Ti, despite the similar P-wave moduli and densities of the two phases. Extraction of the transformation kinetics was shown to be complicated by a strong starting texture in the as-received condition and extensive β grain growth above the

transus. It was found that under these conditions, the local texture must be incorporated into the analysis to predict the correct velocity. For tests where texture was well quantified, there was a strong agreement between predicted and measured velocity. Conversely, if texture was not well quantified, as was the case in heating of the as-received specimens, the model would be incapable of predicting the experimentally observed velocity. The non-monotonic presentation observed here was attributed to a decrease in velocity caused by the phase transformation, followed by a rapid grain growth in the β phase that caused an increase in velocity. This change is qualitatively consistent to the recent *in-situ* EBSD observations of the $\alpha \rightarrow \beta$ transformation from a similar starting texture in cp-Ti [11].

Finally, the third study presented in Chapter 7 took Ti-5553 specimens, solutionized them to the fully β condition, and then held them for varying times at a 700 °C isotherm to monitor precipitation kinetics with LUMet. The precipitation of α grains could be monitored by using the relative change in velocity and one *ex-situ* obtained phase fraction. This was necessary, because unlike the cp-Ti waveforms, the Ti-5553 waveforms were attenuated and asymmetric, and induced a consistent offset into the absolute value of velocity. Even still, using the relative change in velocity was able to provide comparable phase fraction data to the metallographic obtained phase fraction data. Thus, laser ultrasound is able to provide a fast, responsive and *in-situ* method to measure α-precipitation kinetics in Ti-5553, even though it is a material which demonstrates complex morphologies and microstructures.

8.2 Future work

To date, while the temperature dependence of the polycrystalline elastic moduli is available [1, 38], the temperature dependence of the single crystal elastic constants in pure titanium has not been measured. Using a procedure and texture based velocity model similar to one utilized and validated in Chapter 6 it may be possible to design experiments and infer the temperature dependence of the bcc elastic constants. However, for this proposal to be successful, an additional model must be incorporated into the analysis. A model capable of determining the orientation of the high temperature β phase from measured EBSD data for the low-temperature phase has been developed in the literature [100].

The first step would be to design a pre-treatment step that would maximize the bcc grain size, since creating a single crystal of bcc pure titanium is unheard of. This can be accomplished by either extended holding treatments above the transus, or repeated cycling treatments, and then verified by performing EBSD after the treatment, and calculating the location of prior-β grain boundaries or by using Glavicic's approach [100] to approximate the bcc microstructure.

The next step would be to perform a continuous heating cycle on a pre-treated specimen where LUMet monitoring of velocity would occur. Then perform a large EBSD comboscan along the cross section of the wave propagation interaction volume located at the center-line of the specimen. After, use Glavicic's approach [100] in combination with the bcc single crystal elastic constants at 1000 °C [37] and the anisotropy dependent velocity model to approximate the high temperature bcc structure by fitting it to match the observed velocity in the bcc phase at 1000 °C for that cycle. Originally, his model works by selecting possible variants that minimize the global misorientation of the map. By adding the goal seeking approach to predict the experimentally observed velocity, the variants of each grain in the multicrystal can be more accurately selected. The orientations of the bcc crystals once determined are now assumed to not change during the high temperature segment of the cycle, as this was shown in Chapter 6.

Now the problem is defined in such a way that the temperature is changing as an input variable, the texture of the bcc phase is a constant input, the predicted velocity is a modeled output which is compared to the experimentally observed velocity, and the bcc single crystal elastic constants (c_{11}, c_{12} and c_{44}) are unknown inputs. Because there are three unknowns, three equations must be analyzed, and thus, three separate cycle treatments on separate specimens with distinct multicrystal textures (input) and observed velocities (output) must be performed in order to goal seek for the temperature dependence of c_{11}, c_{12} and c_{44}. This approach should then be repeated to validate in the temperature dependence of c_{11}, c_{12} and c_{44}. This approach is not perfect, and of course it is always preferable to perform a directional study on a single crystal, but considering the limitations of the high temperature bcc phase, it is a good attempt at determining the single crystal elastic constants.

Many possible avenues regarding further study of alloy Ti-5553 exist due to it being relatively new to western markets and its current demand in landing gear applications. This study focused on the detection and monitoring of the $\beta \rightarrow \alpha$ transformation during an isothermal aging treatment.

However, much interest surrounds the detection of the ω phase. Exploring the effect of ω phase precipitation on velocity and attenuation to see if the formation of the small nano-sized precipitates would be resolvable by LUMet would be valuable. Also, now that LUMet has been validated as an effective tool to monitor the $\beta \rightarrow \alpha$ phase transformation in this alloy, performing repeated isothermal and continuous cooling treatments to create a detailed time temperature transformation (TTT) diagram and continuous cooling transformation diagram (CCT) would be a valued addition to the literature.

Bibliography

[1] O. N. Senkov, M. Dubois, and J. J. Jonas. Elastic moduli of titanium-hydrogen alloys in the temperature range 20C to 1100C. *Metallurgical and Materials Transactions A*, 27(12):3963–3970, December 1996.

[2] S. Zamiri, B. Reitinger, H. Grun, J. Roither, S. Bauer, and P. Burgholzer. Laser ultrasonic velocity measurement for phase transformation investigation in titanium alloy. pages 683–686. IEEE, July 2013.

[3] M. Donachie. *Titanium: a technical guide*. ASM International, Materials Park, Ohio, 2000.

[4] G. Lutjering and J.C. Williams. *Titanium*. Materials Engineering And Processes. Springer, 2 edition, 2007.

[5] O.M. Ivasishin, P.E. Markovsky, Yu.V. Matviychuk, S.L. Semiatin, C.H. Ward, and S. Fox. A comparative study of the mechanical properties of high-strength beta-titanium alloys. *Journal of Alloys and Compounds*, 457(1-2):296–309, June 2008.

[6] V. V. Shevel'kov and L. F. Kratovich. Design strength of VT22 titanium alloy in different structural conditions. *Soviet Materials Science*, 26(6):687–691, 1991.

[7] A.F. Gerday, M. Ben Bettaieb, L. Duchêne, N. Clément, H. Diarra, and A.M. Habraken. Interests and limitations of nanoindentation for bulk multiphase material identification: Application to the beta phase of Ti-5553. *Acta Materialia*, 57(17):5186–5195, October 2009.

[8] J.C. Fanning. Properties of TIMETAL 555 (Ti-5al-5mo-5v-3cr-0.6fe). *Journal of Materials Engineering and Performance*, 14(6):788–791, December 2005.

[9] C Leyens, M Peters, John Wiley & Sons, and Wiley InterScience (Online service). *Titanium and titanium alloys fundamentals and applications*. Wiley-VCH ; John Wiley] [distributor], Weinheim; Chichester, 2003.

[10] R. Panza-Giosa. *The effect of heat treatment on the microstructural evolution and mechanical properties of Ti-5Al-5V-5Mo-3Cr, and its potential application in landing gears*. PhD thesis, McMaster University, 2009.

[11] G.G.E. Seward, S. Celotto, D.J. Prior, J. Wheeler, and R.C. Pond. In situ SEM-EBSD observations of the hcp to bcc phase transformation in commercially pure titanium. *Acta Materialia*, 52(4):821–832, February 2004.

[12] F.X. Gil, D. Rodrguez, and J.A. Planell. Grain growth kinetics of pure titanium. *Scripta Metallurgica et Materialia*, 33(8):1361–1366, October 1995.

[13] T. Ahmed and H.J. Rack. Phase transformations during cooling in alpha + beta titanium alloys. *Materials Science and Engineering: A*, 243(1-2):206–211, March 1998.

[14] M. S. Oh, Jai-Y. Lee, and J. K. Park. Continuous cooling beta to alpha transformation behaviors of extra-pure and commercially pure Ti. *Metallurgical and Materials Transactions A*, 35(10):3071–3077, October 2004.

[15] S. K. Kim and J. K. Park. In-situ measurement of continuous cooling beta to alpha transformation behavior of CP-Ti. *Metallurgical and Materials Transactions A*, 33(4):1051–1056, April 2002.

[16] G. Ltjering. Influence of processing on microstructure and mechanical properties of (alpha + beta) titanium alloys. *Materials Science and Engineering: A*, 243(1-2):32–45, March 1998.

[17] W. Szkliniarz and G. Smołka. Analysis of volume effects of phase transformation in titanium alloys. *Journal of Materials Processing Technology*, 53(1-2):413–422, August 1995.

[18] J. Teixeira, B. Appolaire, E. Aeby-Gautier, S. Denis, G. Cailletaud, and N. Späth. Transformation kinetics and microstructures of Ti17 titanium alloy during continuous cooling. *Materials Science and Engineering: A*, 448(1-2):135–145, March 2007.

[19] S Malinov, W Sha, Z Guo, C.C Tang, and A.E Long. Synchrotron X-ray diffraction study of the phase transformations in titanium alloys. *Materials Characterization*, 48(4):279–295, June 2002.

[20] J.W. Elmer, T.A. Palmer, S.S. Babu, and E.D. Specht. In situ observations of lattice expansion and transformation rates of alpha and beta phases in Ti6al4v. *Materials Science and Engineering: A*, 391(1-2):104–113, January 2005.

[21] D. Ma, A. D. Stoica, K. An, L. Yang, H. Bei, R. A. Mills, H. Skorpenske, and X.-L. Wang. Texture Evolution and Phase Transformation in Titanium Investigated by In-Situ Neutron Diffraction. *Metallurgical and Materials Transactions A*, 42(6):1444–1448, June 2011.

[22] E. S. Makarov and L. M. Kuznetsov. The crystal structure and chemical character of lower oxides of titanium TiO00.48. *Journal of Structural Chemistry*, 1(2):156–162, July 1960.

[23] Gordon A. Sargent and Hans Conrad. On the strengthening of titanium by oxygen. *Scripta Metallurgica*, 6(11):1099–1101, November 1972.

[24] R. Montanari, G. Costanza, M.E. Tata, and C. Testani. Lattice expansion of Ti6al4v by nitrogen and oxygen absorption. *Materials Characterization*, 59(3):334–337, March 2008.

[25] X.-G. Lu, M. Selleby, and B. Sundman. Assessments of molar volume and thermal expansion for selected bcc, fcc and hcp metallic elements. *Calphad*, 29(1):68–89, March 2005.

[26] E. K. Molchanova. *Phase diagrams of titanium alloys*. Israel Program for Scientific Translations (1965), 1965.

[27] A. S. M. International. Al (Aluminium) Binary Alloy Phase Diagrams. In *Alloy Phase Diagrams*, volume 3 of *ASM Handbook*, page 2.42.56. 1992.

[28] A. S. M. International. Mo (Molybdenum) Binary Alloy Phase Diagrams. In *Alloy Phase Diagrams*, volume 3 of *ASM Handbook*, page 2.2922.298. 1992.

[29] A. S. M. International. Ti (Titanium) Binary Alloy Phase Diagrams. In *Alloy Phase Diagrams*, volume 3 of *ASM Handbook*, page 2.3783.380. 1992.

[30] A. Kamp. *Investigation of titanium alpha plates by EBSD analysis*. PhD thesis, Delft University of Technology, Delft, Netherlands, 2007.

[31] H.W. Rosenberg. Titanium alloying in theory and practice. *The Science, Technology and Application of Titanium*, pages 851–859, 1970.

[32] G. Welsch, R. Boyer, and E.W. Collings. *Materials Properties Handbook: Titanium alloys*. ASM international, 1993.

[33] C. Lin, G. Yin, Y. Zhao, P. Ge, and Z. Liu. Analysis of the effect of alloy elements on martensitic transformation in titanium alloy with the use of valence electron structure parameters. *Materials Chemistry and Physics*, 125(3):411–417, February 2011.

[34] N.V. Ageev and L.A. Petrova. The theoretical bases of the development of the hight-strength metastable beta alloys of titanium. *The Science, Technology and Application of Titanium*, pages 809–814, 1970.

[35] J. Coakley, V. A. Vorontsov, N. G. Jones, A. Radecka, P. A. J. Bagot, K. C. Littrell, R. K. Heenan, F. Hu, A. P. Magyar, D. C. Bell, and D. Dye. Precipitation processes in the Beta-Titanium alloy Ti5al5mo5v3cr. *Journal of Alloys and Compounds*, 646:946–953, October 2015.

[36] E.S. Fisher and C.J. Renken. Single-Crystal Elastic Moduli and the hcp to bcc Transformation in Ti, Zr, and Hf. *Physical Review*, 135(2A), 1964.

[37] E.S. Fisher and D. Dever. The single crystal elastic moduli of beta-titanium and titanium-chromium alloys. *The Science, Technology and Application of Titanium*, pages 373–381, 1968.

[38] H. Ogi, S. Kai, H. Ledbetter, R. Tarumi, M. Hirao, and K. Takashima. Titaniums high-temperature elastic constants through the hcpbcc phase transformation. *Acta Materialia*, 52(7):2075–2080, April 2004.

[39] W. Petry, A. Heiming, J. Trampenau, M. Alba, C. Herzig, H. R. Schober, and G. Vogl. Phonon dispersion of the bcc phase of group-IV metals. I. bcc titanium. *Physical Review B*, 43(13):10933–10947, May 1991.

[40] S. Nishitani, H. Kawabe, and M. Aoki. First-principles calculations on bcchcp transition of titanium. *Materials Science and Engineering: A*, 312(1-2):77–83, August 2001.

[41] H. Ledbetter. Elastic constants of body-centered-cubic titanium monocrystals. *Journal of Applied Physics*, 95(9):4642, 2004.

[42] M. Sanati, A. Saxena, T. Lookman, and R. C. Albers. Landau free energy for a bcc-hcp reconstructive phase transformation. *Physical Review B*, 63(22), May 2001.

[43] R. Ahuja, J. M. Wills, B. Johansson, and O. Eriksson. Crystal structures of Ti, Zr, and Hf under compression: Theory. *Physical Review B*, 48(22):16269–16279, December 1993.

[44] W. Hosford. *The mechanics of crystals and textured polycrystals*, volume 32 of *Oxford engineering sciences series*. Oxford University Press, New York, 1993.

[45] C. G. Rhodes and J. C. Williams. The precipitation of alpha-phase in metastable beta-phase Ti alloys. *Metallurgical Transactions A*, 6(11):2103–2114, November 1975.

[46] E. S. K. Menon and H.I. Aaronson. Interfacial structure of widmanstatten plates in a TiCr alloy. *Acta Metallurgica*, 34(10):1975–1981, October 1986.

[47] T. Furuhara and H.I. Aaronson. Crystallography and interfacial structure of proeutectoid alpha grain boundary allotriomorphs in a hypoeutectoid TiCr alloy. *Acta Metallurgica et Materialia*, 39(11):2887–2899, November 1991.

[48] W.G. Burgers. On the process of transition of the cubic-body-centered modification into the hexagonal-close-packed modification of zirconium. *Physica*, 1(7-12):561–586, May 1934.

[49] C. Zener. Contributions to the Theory of Beta-Phase Alloys. *Physical Review*, 71(12):846–851, June 1947.

[50] N. N. Sirota and T. E. Zhabko. X-ray study of the anisotropy of thermal properties in titanium. *Physica Status Solidi (a)*, 63(2):K211–K215, February 1981.

[51] J. Spreadborough and J. W. Christian. The Measurement of the Lattice Expansions and Debye Temperatures of Titanium and Silver by X-ray Methods. *Proceedings of the Physical Society*, 74(5):609–615, November 1959.

[52] H. Kleinschmidt, A. Ziegler, G. H. Campbell, J. D. Colvin, and O. Bostanjoglo. Phase transformation analysis in titanium at nanosecond time resolution. *Journal of Applied Physics*, 98(5):054313, 2005.

[53] M. Grujicic and P. Dang. Atomic-scale analysis of martensitic transformation in titanium alloyed with vanadium Part I: verification of the embedded-atom method model. *Materials Science and Engineering: A*, 205(1-2):139–152, January 1996.

[54] S. Banerjee and P. Mukhopadhyay. *Phase transformations: examples from titanium and zirconium alloys*. Elsevier, 1 edition, 2007.

[55] S. Nag, R. Banerjee, J.Y. Hwang, M. Harper, and H.L. Fraser. Elemental partitioning between alpha and beta phases in the Ti5al5mo5v3cr0.5fe (Ti-5553) alloy. *Philosophical Magazine*, 89(6):535–552, February 2009.

[56] A. Settefrati, E. Aeby-Gautier, B. Appolaire, M. Dehmas, G. Geandier, and G. Khelifati. Low Temperature Transformations in beta-Metastable Ti 5553 Titanium Alloy. *Materials Science Forum*, 738-739:97–102, January 2013.

[57] S. K. Kar, A. Ghosh, N. Fulzele, and A. Bhattacharjee. Quantitative microstructural characterization of a near beta Ti alloy, Ti-5553 under different processing conditions. *Materials Characterization*, 81:37–48, July 2013.

[58] A. Dehghan-Manshadi and R. J. Dippenaar. Development of alpha-phase morphologies during low temperature isothermal heat treatment of a Ti5al5mo5v3cr alloy. *Materials Science and Engineering: A*, 528(3):1833–1839, January 2011.

[59] S. Malinov, W. Sha, and P. Markovsky. Experimental study and computer modelling of the beta to alpha + beta phase transformation in beta 21s alloy at isothermal conditions. *Journal of Alloys and Compounds*, 348(1-2):110–118, January 2003.

[60] T. Furuhara, S. Takagi, H. Watanabe, and T. Maki. Crystallography of grain boundary alpha precipitates in a beta titanium alloy. *Metallurgical and Materials Transactions A*, 27(6):1635–1646, 1996.

[61] S. Malinov, P. Markovsky, and W. Sha. Resistivity study and computer modelling of the isothermal transformation kinetics of Ti8al1mo1v alloy. *Journal of Alloys and Compounds*, 333(1-2):122–132, February 2002.

[62] J.-P. Monchalin. Laser-Ultrasonics: From the Laboratory to Industry. volume 700, pages 3–31. AIP, 2004.

[63] M. Falkenström, M. Engman, E. Lindh-Ulmgren, and B. Hutchinson. Laser ultrasonics for process control in the metal industry. *Nondestructive Testing and Evaluation*, 26(3-4):237–252, September 2011.

[64] E. Fraizier, M.-H. Nadal, and R. Oltra. Noncontact determination of the elastic moduli of beta-Sn up and through the melting point. *Journal of Applied Physics*, 93(1):649, 2003.

[65] A. Moreau, C. Bescond, S. Bolognini, M. Lord, S.E. Kruger, and C. S. Man. Inline Measurements of Texture and Recrystallization on Aluminum Alloys. pages 3–10. Automation & Control/ Advanced OnLine Metallurgical Models/Sensors Materials, Materials Science & Technology, 2005.

[66] S. Sarkar, A. Moreau, M. Militzer, and W.J. Poole. Evolution of Austenite Recrystallization and Grain Growth Using Laser Ultrasonics. *Metallurgical and Materials Transactions A*, 39(4):897–907, April 2008.

[67] A. Moreau, D. Lévesque, M. Lord, M. Dubois, J.-P. Monchalin, C. Padioleau, and J.F. Bussière. On-line measurement of texture, thickness and plastic strain ratio using laser-ultrasound resonance spectroscopy. *Ultrasonics*, 40(10):1047–1056, December 2002.

[68] M. Militzer, T. Garcin, and W. J. Poole. In-situ Measurements of Grain Growth and Recrystallization by Laser Ultrasonics. *Materials Science Forum*, 753:25–30, March 2013.

[69] Silvio E. Kruger and Edward B. Damm. Monitoring austenite decomposition by ultrasonic velocity. *Materials Science and Engineering: A*, 425(1-2):238–243, June 2006.

[70] M. Dubois, A. Moreau, and J. F. Bussière. Ultrasonic velocity measurements during phase transformations in steels using laser ultrasonics. *Journal of Applied Physics*, 89(11):6487, 2001.

[71] M. Maalekian, R. Radis, M. Militzer, A. Moreau, and W.J. Poole. In situ measurement and modelling of austenite grain growth in a Ti/Nb microalloyed steel. *Acta Materialia*, 60(3):1015–1026, February 2012.

[72] M. Dubois. A new technique for the quantitative real-time monitoring of austenite grain growth in steel. *Scripta Materialia*, 42(9):867–874, April 2000.

[73] D. A. Hutchins. Ultrasonic generation by pulsed lasers. In *Physical Acoustics*, volume 18, pages 21–123. Academic Press W.P. Mason and R.N. Thurston, eds., 1988.

[74] C. M. Scala. Time- and frequency-domain characteristics of laser-generated ultrasonic surface waves. *The Journal of the Acoustical Society of America*, 85(4):1569, 1989.

[75] R. K. Ing and J.-P. Monchalin. Broadband optical detection of ultrasound by two-wave mixing in a photorefractive crystal. *Applied Physics Letters*, 59(25):3233, 1991.

[76] J.-P. Monchalin, R. Héon, P. Bouchard, and C. Padioleau. Broadband optical detection of ultrasound by optical sideband stripping with a confocal FabryPerot. *Applied Physics Letters*, 55(16):1612, 1989.

[77] G. Hamel de Monchenault and Jp. Huignard. Two-wave mixing with time-modulated signal in Bi12sio20 theory and application to homodyne wave-front detection. *Journal of Applied Physics*, 63(3):624, 1988.

[78] A. Moreau, P.J. Kielczynski, J.F. Bussière, and J. H. Root. Ultrasonic Characterization ofTexture in Pure and Alloyed Zirconium. pages 119–128. Nondestructive Characterization of Materials VI, Plenum Press, New York, 1994.

[79] B.A. Auld. *Acoustic fields and waves in solids*, volume 1. John Wiley & Sons, Inc., 1973.

[80] D. Mainprice, R. Hielscher, and H. Schaeben. Calculating anisotropic physical properties from texture data using the MTEX open-source package. *Geological Society, London, Special Publications*, 360(1):175–192, January 2011.

[81] M. Slawinski. *Waves and rays in elastic continua*. Creative Commons, 2 edition, 2007.

[82] D. Tromans. Elastic anisotrioy of hcp metal crystals and polycrystals. *IJRRAS*, 6(4):462–483, March 2011.

[83] J. Bradford and R. Latimer. *Advances in Near-surface Seismology and Ground-penetrating Radar*, volume 15 of *Geophysical Development Series*. American Geophysical Union, 2010.

[84] W. Voight. Ueber die Beziechung zwischen den beiden Elasticitatsconstanten isotroper Korper. *Ann. d. phys. u. chem.*, 38:573–587, 1889.

[85] A. Reuss. Berechung der Fliebenze von Mischkristallen auf Grund der Plastizitatsbedingung fur Einkristalle. *Zeit. Angew. Math. Mech.*, 9:49–58, 1929.

[86] M. Hirao. Texture of polycrystalline metals characterized by ultrasonic velocity measurements. *The Journal of the Acoustical Society of America*, 81(5):1434, 1987.

[87] A.D. Rollett. Orientation Distribution: Definition, discrete forms, examples, September 2011.

[88] S.C. Wang, M. Aindow, and M.J. Starink. Effect of self-accommodation on alpha/alpha boundary populations in pure titanium. *Acta Materialia*, 51(9):2485–2503, May 2003.

[89] T. Garcin. Computational Tools for Metallurgy (CTOME), 2015. http://ctome.org/.

[90] T. Williams, Kelley C., and D. Crawford. Gnuplot 4.6, an interactive plotting program, 2014. http://www.gnuplot.info/docs4.6/gnuplot.pdf.

[91] Q. Puydt, T. Garcin, M. Militzer, and W. J. Poole. Us wave propagation in an elastic medium: 2 d finite element modelling. international workshop on laser ultrasonics for metallurgy, November 2013.

[92] T. Garcin, Q. Puydt, W. J. Poole, and M. Militzer. Simulation of ultrasound propagation in anisotropic polycrystalline media, November 2013.

[93] B. Tie, D. Solas, J. Thébault, C. Rey, T. Baudin, and A.-S. Mouronval. Modélisation numérique de la propagation des ultrasons dans des milieux polycrystallins. Lyon France, 2010.

[94] T.W. Murray and J.W. Wagner. Laser generation of acoustic waves in the ablative regime. *Journal of Applied Physics*, 85(4):2031–2040, February 1999.

[95] C. Jourdan, J. Gastaldi, and G. Grange. Heterogeneous nucleation during the titanium alpha to beta transformation studied by Synchrotron X-ray topography. *Acta Metallurgica*, 36(11):2979–2987, November 1988.

[96] A.O.F. Hayama and H.R.Z. Sandim. Annealing behavior of coarse-grained titanium deformed by cold rolling. *Materials Science and Engineering: A*, 418(1-2):182–192, February 2006.

[97] Z.S. Zhu, J.L. Gu, R.Y. Liu, N.P. Chen, and M.G. Yan. Variant selection and its effect on phase transformation textures in cold rolled titanium sheet. *Materials Science and Engineering: A*, 280(1):199–203, March 2000.

[98] N. Gey and M. Humbert. Characterization of the variant selection occurring during the alpha to beta to alpha phase transformations of a cold rolled titanium sheet. *Acta Materialia*, 50(2):277–287, January 2002.

[99] D. R. Hull, H. E. Kautz, and Vary A. Ultrasonic velocity measurement using phase-slope and cross correlation methods. *NASA technical memorandum 83794. Spring Conference of the American Society for Nondestructive Testing*, 1984.

[100] M.G. Glavicic, P.A. Kobryn, T.R. Bieler, and S.L. Semiatin. A method to determine the orientation of the high-temperature beta phase from measured EBSD data for the low-temperature alpha phase in Ti-6al-4v. *Materials Science and Engineering: A*, 346(1-2):50–59, April 2003.

Appendix A

EBSD IPF comboscan maps

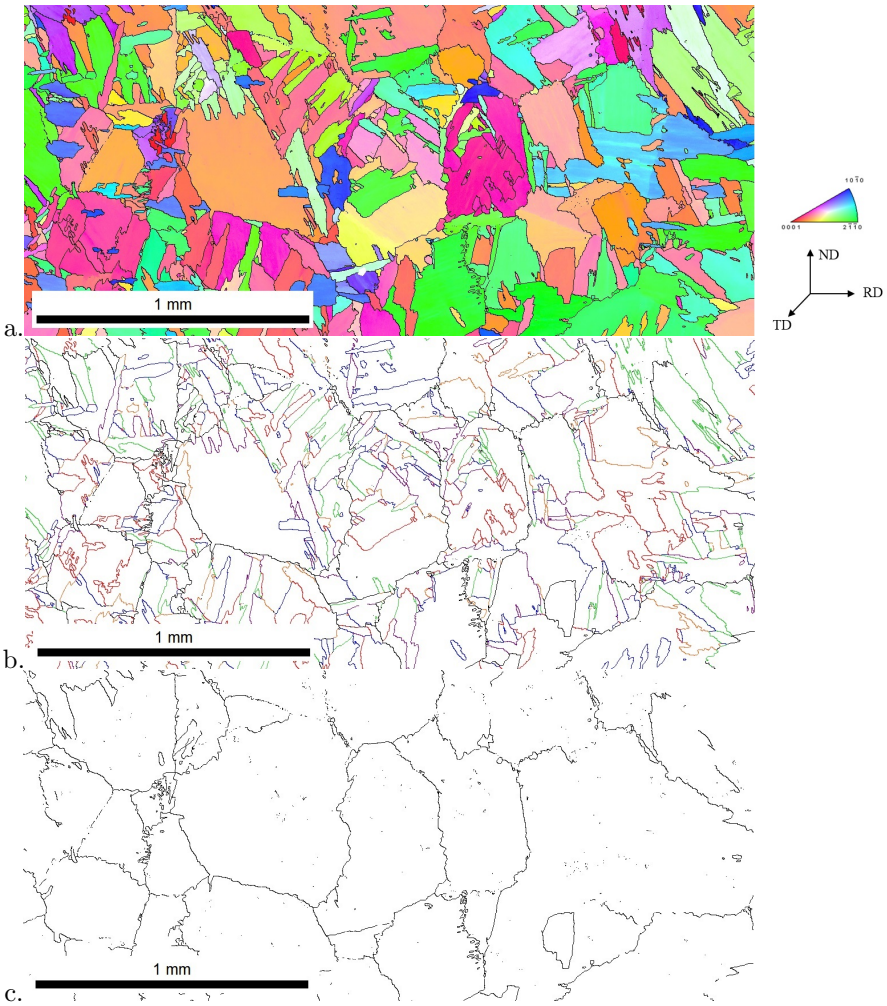

Figure A.1: Full EBSD obtained comboscan a) inverse ND pole figure maps (ND - IPF maps) showing the microstructure and microtexture, b) the α/α special boundary map, and c) prior β special boundary map of a specimen after 1 treatment cycle

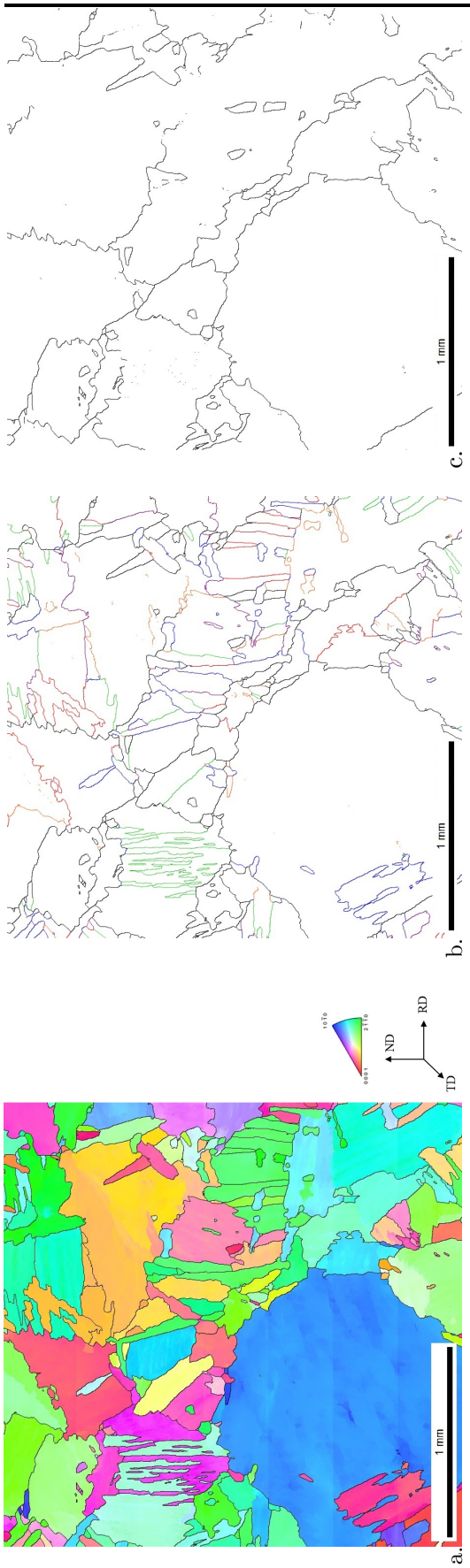

Figure A.2: Full EBSD obtained comboscan a) inverse ND pole figure maps (ND - IPF maps) showing the microstructure and microtexture, b) the α/α special boundary map, and c) prior β special boundary map of a specimen after 5 treatment cycles.

Appendix B

Plotting 3-D Surface Young modulus as a Function of Orientation

B.1 Young modulus as a function of orientation in the titanium hcp unit cell

The following is the script created in the PyDev module of Eclipse SDK used to plot the elastic response surface for an titanium hcp unit cell. The single crystal elastic constants lines were linear regressions of data in the literature [36], and the mathematical approach was taken from Hosford's textbook [44].

```
'''
Created on 2015-04-07

@author: Alyssa
'''
import re
import math
import numpy as np
import matplotlib.pyplot as plt
from matplotlib import *
from scipy.constants.constants import alpha
import itertools
from mpl_toolkits.mplot3d import axes3d, Axes3D
from matplotlib.font_manager import FontProperties


gammagamma = np.arange(1.0, 181.0,1)

T = 882  # put T in Celsius here
c11 = (-0.0513*T + 163.34) * math.pow(10.0, 9.0)
c12 = (0.0118*T + 91.313) * math.pow(10.0, 9.0)
c13 = (0.0006*T + 68.736) * math.pow(10.0, 9.0)
c33 = (-0.0363*T + 181.29) * math.pow(10.0, 9.0)
c44 = (-0.0199*T + 46.856) * math.pow(10.0, 9.0)
c66 = 0.5 * (c11 - c12)
A = c44/c66
print A
c_hcp = np.array([[c11, c12, c13, 0, 0, 0],
```

```
[c12, c11, c13, 0, 0, 0], [c13, c13, c33, 0, 0, 0],
[ 0, 0, 0, c44, 0, 0], [0, 0, 0, 0, c44, 0],
[0, 0, 0, 0, 0, c66]])

s_hcp = np.linalg.inv(c_hcp)

tera = 1000.0
s11 = s_hcp[0,0] * math.pow(10, 9)
s12 = s_hcp[0,1] * math.pow(10, 9)
s13 = s_hcp[0,2] * math.pow(10, 9)
s33 = s_hcp[2,2] * math.pow(10, 9)
s44 = s_hcp[3,3] * math.pow(10, 9)
s66 = s_hcp[5,5] * math.pow(10, 9)
print s11
print s12
print s44

alpha = []
beta = []
gamma = []

gammagamma = np.arange(1.0, 181.0,1)
x = []
y = []
z = []
r = []
zMax = 0
xMax = 0

for i in range(0, gammagamma.__len__()):
    g = math.radians(gammagamma[i])
    phi = g;
    g = math.cos(g)

    Edinv = math.pow((1.0 - math.pow(g, 2)), 2)*s11
        + math.pow(g, 4)*s33
        + math.pow(g, 2)*(1.0 - math.pow(g, 2))*(2.0*s13 + s44)

    if Edinv == 0.0:
        Ed = 0.0
    else:
        Ed = 1.0/Edinv #radius


    for otherAngle in range(1, 361):

        angle = math.radians(otherAngle)

        xCart = Ed*math.cos(angle)*math.sin(phi) #x
        yCart = Ed*math.sin(angle)*math.sin(phi)#y
        zCart =  Ed*math.cos(phi)#z
        r.append(Ed)
        x.append(xCart)
        y.append(yCart)
```

```
        z.append(zCart)

        if xCart > xMax:
            xMax = xCart
        if zCart > zMax:
            zMax = zCart

print 'xMax: '+str(xMax)
print 'zMax: '+str(zMax)

print 'plotting'

font = {'family' : 'Times New Roman'
        }

fig = plt.figure(figsize=(10, 10))
ax = fig.gca(projection='3d')

ax.set_autoscale_on(False)
ax.axis([-200, 200, -200, 200], fontdict = font)
ax.set_zlim(-200, 200)
ax.xaxis.set_ticks(np.arange(-200, 300, 100))
ax.yaxis.set_ticks(np.arange(-200, 300, 100))
ax.zaxis.set_ticks(np.arange(-200, 300, 100))

fontprop =
font_manager.FontProperties(family='Times New Roman', size=28)

for tick in ax.xaxis.get_major_ticks():
    tick.label.set_font_properties(fontprop)

for tick in ax.yaxis.get_major_ticks():
    tick.label.set_font_properties(fontprop)

for tick in ax.zaxis.get_major_ticks():
    tick.label.set_font_properties(fontprop)

ax.scatter(x, y, z, c=r, cmap=cm.get_cmap('gray'))

ax.set_xlabel('x', size=28, fontdict = font)
ax.set_ylabel('y',size=28, fontdict = font)
ax.set_zlabel('z', size=28, fontdict = font)

plt.show()
```

B.2 Young modulus as a function of orientation in the titanium bcc unit cell

The following is the script created in the PyDev module of Eclipse SDK used to plot the elastic response surface for an titanium bcc unit cell at 1000 °C. The single crystal elastic constants were taken from the literature [37], and the mathematical approach was taken from Hosford's textbook [44].

```
'''
Created on 2015-04-07

@author: Alyssa
'''
import re
import math
import numpy as np
import matplotlib.pyplot as plt
from matplotlib import *
from scipy.constants.constants import alpha
import itertools
from mpl_toolkits.mplot3d import axes3d, Axes3D
from matplotlib.font_manager import FontProperties
from matplotlib.pyplot import draw
from matplotlib.delaunay.triangulate import Triangulation
from matplotlib.patches import Shadow

'''
Data for c11, c12, c44
taken from Fisher and Dever,
given in GPa at T = 1000C
'''
c11 = 99
c12 = 85
c44 = 33.6

s11 = (c11 + c12)/(math.pow(c11, 2)
+ c11*c12 - 2*math.pow(c12, 2))

s12 = (-c12)/(math.pow(c11, 2)
+ c11*c12 - 2*math.pow(c12, 2))

s44 = 1/c44

E100= 1/s11
E111 = 3.0/(s11 +2.0*s12 +s44)

print E100
print E111

alpha = []
beta = []
gamma = []
r = []
x = []
```

```
y = []
z = []
h = []
zMax = 0
xMax = 0



for i in range(1, 181):
    g = math.radians(i)
    phi = g;
    g = math.cos(g)
    for j in range(1, 361):
        h = math.radians(j)
        theta = h
        th = math.cos(g)
        alpha = math.sin(phi)*math.cos(theta)
        beta = math.sin(phi)*math.sin(theta)
        a2 = math.pow(alpha, 2)
        b2 = math.pow(beta, 2)
        g2 = math.pow(g, 2)
        f =3.0*(b2*g2 + g2*a2 + a2*b2)

        Edinv = 1/E100 + f*(1/E111 - 1/E100)


        if Edinv == 0.0:
            Ed = 0.0
        else:
            Ed = 1.0/Edinv #radius
            xCart = Ed*math.cos(theta)*math.sin(phi) #x
            yCart = Ed*math.sin(theta)*math.sin(phi)#y
            zCart =  Ed*math.cos(phi)#z

            r.append(Ed)
            x.append(xCart)
            y.append(yCart)
            z.append(zCart)

            if xCart > xMax:
                xMax = xCart
            if zCart > zMax:
                zMax = zCart

print 'xMax: '+str(xMax)
print 'zMax: '+str(zMax)

print x.__len__()

print 'plotting'

font = {'family' : 'Times New Roman'
        }
```

```
fig = plt.figure(figsize=(10, 10))
ax = fig.add_subplot(111, projection='3d')

ax.set_autoscale_on(False)
ax.axis([-60, 60, -60, 60], fontdict = font)
ax.set_zlim(-60, 60)
ax.xaxis.set_ticks(np.arange(-60, 60, 20))
ax.yaxis.set_ticks(np.arange(-60, 60, 20))
ax.zaxis.set_ticks(np.arange(-60, 60, 20))

fontprop = font_manager.FontProperties(family='Times New Roman', size=28)

for tick in ax.xaxis.get_major_ticks():
    tick.label.set_font_properties(fontprop)

for tick in ax.yaxis.get_major_ticks():
    tick.label.set_font_properties(fontprop)

for tick in ax.zaxis.get_major_ticks():
    tick.label.set_font_properties(fontprop)

print len(x)
print len(y)
print len(z)

ax.scatter(x, y, z, c=r, cmap=cm.get_cmap('gray'))

ax.set_xlabel('x',size=28, fontdict = font)
ax.set_ylabel('y',size=28, fontdict = font)
ax.set_zlabel('z', size=28, fontdict = font)

plt.show()
```